Karlsruhe Institute of Technology

Quantification of Greenhouse Gas Emissions in Thessaloniki, Greece

Master's Thesis of

Pablo Lenard Schmid

at the Department of Physics
IMK-ASF – Institute of Meteorology and Climate Research - Atmospheric Trace Gases and Remote Sensing

Reviewer:	Prof. Dr. Peter Braesicke
Second reviewer:	PD Dr. Frank Hase
Advisor:	M. Sc. Lena Feld

01. February 2022 – 01. February 2023

Karlsruhe Institute of Technology
Department of Physics
D-76128 Karlsruhe

I declare that I have developed and written the enclosed thesis completely by myself. I have submitted neither parts of nor the complete thesis as an examination elsewhere. I have not used any other than the aids that I have mentioned. I have marked all parts of the thesis that I have included from referenced literature, either in their original wording or paraphrasing their contents. This also applies to figures, sketches, images and similar depictions, as well as sources from the internet.

Karlsruhe, 01.02.2023

. . . . . .

(Pablo Lenard Schmid)

Abstract

In this work, a pair of Bruker^{TM} EM27/SUN FTIR spectrometers and a box model are used to estimate area emission fluxes[1] of greenhouse gases (GHGs) in Thessaloniki, Greece. A measurement campaign is carried out in October 2021 and summer 2022 in the framework of the COllaborative Carbon Column Observing Network (COCCON). One spectrometer is permanently located in the city centre, while another instrument is located depending on the daily wind situation. With this setup, column-averaged dry-air mole fractions (DMFs) of the GHGs carbon dioxide (CO_2) and methane (CH_4), as well as of CO as an indicator of combustion processes, are measured. Based on the observed abundances, the analysis focuses on the estimation of area emission fluxes with a box model. The model is fed with concentration differences between the upwind and downwind spectrometer. In addition, a low wind speed limit calculation is used as an alternative method to estimate potential area emission fluxes. Besides the up- and downwind configurations, the spectrometers were also deployed orthogonal to the flow for quantifying the variability of the background concentrations. The observed variability allows an estimate of the background-induced uncertainties in the emission fluxes.

As a city with around 800'000 inhabitants, Thessaloniki is expected to be the dominant local source of GHGs, being home to a harbour, factories, transportation and landfills.

The use of the campaign data to estimate area emission fluxes results in

$$59.9\ \frac{\mathrm{kt}}{\mathrm{km^2 yr}}\ \text{for}\ CO_2,\ 17.1\ \frac{\mathrm{t}}{\mathrm{km^2 yr}}\ \text{for}\ CH_4\ \text{and}\ 66.1\ \frac{\mathrm{t}}{\mathrm{km^2 yr}}\ \text{for CO},$$

where the value of CO_2 is in the upper range of the inventory and those of CH_4 and CO are in the lower range. The use of the box model approach, assuming ideal alignment along the flow and without taking into account the complex orography of Thessaloniki, introduces considerable uncertainties. Those are estimated via error propagation and lie in the order of 100 % of the corresponding averages. The assumed uncertainty in concentration differences is deduced from the level of background variability as observed with the orthogonal alignment. Other important parameters subject to error are the distance between the measurement sites, the wind speed and the ground pressure at each measurement site. The ground pressure is carefully evaluated.

Alternatively, the area emission can be estimated from the rate of increase of columnar gas abundances observed with one spectrometer in the city center under calm conditions. The results based on the single instrument campaign data are 179.2 $\frac{\mathrm{kt}}{\mathrm{km^2 yr}}$ for CO_2,

[1] From the detected enhancement of trace gas concentrations, the corresponding emission (mass per time) can be inferred. Area fluxes (mass per time per area) are a common quantity in the inventory reporting, and the used box model refers to an effective area. The area emission flux therefore can be interpreted as the emissions of an area source.

262.8 $\frac{\mathrm{t}}{\mathrm{km^2 yr}}$ for CH_4 and 559.7 $\frac{\mathrm{t}}{\mathrm{km^2 yr}}$ for CO, and therefore biased high compared to the obtained values from the up- and downwind alignment. The systematic uncertainty implied by the limit case $v \to 0$ is a maximum of 18 %.

This work shows possible applications, extensions, and limitations of a simplistic transport model. From that, realistic results for emissions can be derived using GHG concentration changes measured in Thessaloniki. The investigations presented in this thesis lay the foundation for further refined investigations using simulated trace gas fields and wind profiles.

Zusammenfassung

In dieser Arbeit werden zwei Bruker^{TM} EM27/SUN FTIR-Spektrometer und ein Box-Modell zur Abschätzung der Flächenemissionsflüsse[2] von Treibhausgasen (GHG) in Thessaloniki, Griechenland, verwendet. Eine Messkampagne wird im Oktober 2021 und im Sommer 2022 im Rahmen des Netzwerks COCCON (COllaborative Carbon Column Observing Network) durchgeführt. Ein Spektrometer wird dauerhaft im Stadtzentrum aufgestellt, während ein anderes Instrument abhängig von der täglichen Windsituation plaziert wird. Mit diesem Aufbau werden säulengemittelte Stoffmengenanteile in trockener Luft (column-averaged dry-air mole fractions (DMFs)) der GHGs Kohlendioxid (CO_2) und Methan (CH_4) sowie CO als Hinweis auf Verbrennungsprozesse gemessen. Auf Basis der gefundenen Konzentrationen fokussiert sich die Analyse auf die Abschätzung der Flächenemissionsflüsse mittels eines Box-Modells. Das Modell wird mit gemessenen Konzentrationsunterschieden zwischen dem windzugewandten und dem windabgewandten Spektrometer („Up-Downwind"-Anordnung) gespeist. Darüber hinaus wird ein Grenzfall für schwachen Wind ausgearbeitet, um Flächenemissionen aus der beobachteten lokalen Zunahme der Gasmengen zu erschließen. Zusätzlich zu den „Up-Downwind"-Konfigurationen werden die Spektrometer auch orthogonal zur Strömung eingesetzt, um die Variabilität der Hintergrundkonzentrationen zu quantifizieren. Die beobachtete Variabilität erlaubt eine Abschätzung der durch den Hintergrund verursachten Unsicherheiten im Emissionsfluss.

Als Stadt mit rund 800.000 Einwohner*innen kann erwartet werden, dass Thessaloniki ein lokaler Hauptverursacher von GHG-Emissionen ist, da sich dort ein Hafen, Fabriken, Verkehr und Mülldeponien befinden. Daher kann von einer Vergleichbarkeit mit den Emissionseigenschaften anderer Großstädte ausgegangen werden.

Die Verwendung der Kampagnendaten zur Abschätzung der Flächenemissionsflüsse führt zu folgenden Ergebnissen:

$$59.9\ \frac{\mathrm{kt}}{\mathrm{km^2 yr}}\ \text{für}\ CO_2,\ 17.1\ \frac{\mathrm{t}}{\mathrm{km^2 yr}}\ \text{für}\ CH_4\ \text{und}\ 66.1\ \frac{\mathrm{t}}{\mathrm{km^2 yr}}\ \text{für CO},$$

wobei das Ergebnis von CO_2 im oberen Bereich und die Ergebnisse von CH_4 und CO jeweils im unteren Bereich der Literaturwerte liegen. Die Verwendung des einfachen Box-Modells, das von idealer Anordnung entlang der Windtrajektorie ausgeht und die komplexe Orographie Thessalonikis nicht berücksichtigt, führt zu erheblichen Unsicherheiten. Diese werden durch Fehlerfortpflanzung abgeschätzt und liegen in einer Größenordnung von 100 % der entsprechenden Mittelwerte. Die angenommene Unsicherheit bei den Konzentrationsunterschieden wird aus der Hintergrundvariabilität abgeleitet, wie sie bei der

[2] Aus der gemessenen Erhöhung der Spurengaskonzentrationen kann die Emission (Masse pro Zeit) gefolgert werden. Flächenflüsse (Masse pro Zeit pro Fläche) sind eine gängige Literaturgröße, und das verwendete Boxmodell bezieht sich auf eine effektive Fläche. Der Flächenemissionsfluss kann daher als die Emissionen einer Flächenquelle interpretiert werden.

orthogonalen Ausrichtung beobachtet wurde. Weitere gewichtige fehlerbehaftete Größen sind der Abstand der Messstandorte, die Windgeschwindigkeit und der Bodendruck. Der Bodendruck wird dabei sorgfältig bestimmt.

Alternativ kann die Flächenemission anhand der Steigerungsrate der lokalen Gaskonzentration geschätzt werden, die mit einem Spektrometer im Stadtzentrum unter ruhigen Windverhältnissen beobachtet wird. Die gemittelten Ergebnisse aus den Kampagnendaten eines einzelnen Instruments sind 179.2 $\frac{\mathrm{kt}}{\mathrm{km^2 yr}}$ für CO_2, 262.8 $\frac{\mathrm{t}}{\mathrm{km^2 yr}}$ für CH_4 und 559.7 $\frac{\mathrm{t}}{\mathrm{km^2 yr}}$ für CO und zeigen höhere Werte als die aus den „Up-Downwind“-Berechnungen gefolgerten. Die systematische Unsicherheit, die sich aus dem Grenzfall $v \to 0$ ergibt liegt bei maximal 18 %.

Diese Arbeit zeigt mögliche Anwendungen, Erweiterungen und Grenzen eines einfachen Transportmodells. Dabei können realistische Ergebnisse für die Flächenemissionen in Thessaloniki aus GHG-Konzentrationsgradienten abgeleitet werden. Die hier durchgeführten Untersuchungen legen den Grundstein für weitergehende Untersuchungen mit simulierten Spurengas- und Windprofilen.

Contents

List of Figures

List of Tables

Introduction

Climate change is driven by the increasing concentration of greenhouse gases (GHG) in the atmosphere, their impact on global warming through radiative forcing (RF) and the reaction of the climate system. The most important GHGs in respect to RF are carbon dioxide (CO_2), methane (CH_4), water vapor (H_2O), nitrous oxide (NH_2) and ozone (O_3). The concentration of CO_2 in the earth's atmosphere rose since industrialization from 280 to over 400 ppm nowadays. CH_4 increased meanwhile from around 720 to over 1860 ppb [IPC21].

To mitigate the drastic consequences from climate change, political action to reduce carbon emissions is necessary [IPC22]. First attempts of organizing climate protecting policies have been done with the Kyoto protocol by the United Nations in 1997 [Uni97] and later in the Paris agreement in 2015 [Uni15]. The latter named the goal to mitigate climate change by keeping the increase of global average temperature well below 2 °C and best under 1.5 °C. One main aspect of those and further contracts on climate protection are mandatory limits of GHG emissions mostly in industrial countries in the global north.

An important requirement of reducing GHG emissions is identifying and quantifying location, strength and eventual temporal behaviour of their sources and sinks. Depending on the desired quantity, there are different methods of measuring GHGs: "In situ" measurements are used to observe the concentration on site to investigate local abundances [Vui+07; RS07; Le +15]. Another approach are remote sensing techniques that can be further divided into satellite-based [Par+11; Mor+11; Vee+12; Fra+15] and ground-based measurements. In the present work, ground-based Fourier-transform infrared spectroscopy (FTIR) finds application to measure total column abundances through all layers of the atmosphere. This method is less dependent on local fluctuations in concentration than in situ measurements.

The Total Carbon Column Observation Network (TCCON) operates as reference source for other ground-based remote sensing measurements and is operated as reference data source for validating space-borne GHG sensors [Wun+11]. The laboratory spectrometers used by TCCON are expensive and immobile because they require regular supervision and operation in a controlled environment (e.g. air-conditioned lab container).

To solve these issues, a new FTIR device was developed by Karlsruhe Institute of Technology (KIT) in cooperation with Bruker Optics™ in Ettlingen: a portable spectrometer called EM27/SUN[3] [Gis+12; Has+16]. The EM27/SUN is compact and can be carried by a person, has proven stability in hard measurement conditions (e.g. hot or cold weather or in dusty conditions) and during transportation, has a lower price and is easy to operate [Fre+15]. In 2019, the COllaborative Carbon Column Observing Network (COCCON) network[4] has been established [Fre+19] to fill the gaps of the TCCON network and extend it to remote

[3] https://www.bruker.com/en/products-and-solutions/infrared-and-raman/remote-sensing/em27-sun-solar-absorption-spectrometer.html

[4] https://www.imk-asf.kit.edu/english/COCCON.php

sites or even dynamic measurements on a ship [Kla+15b]. Various field campaigns have been performed with EM27/SUNs where the device has shown its potential to measure trace gas abundances on a sub percentage level [Fre+15; Has+15; Mak+21; Tu+22; Alb+22b]. Particular interest for measuring GHGs lies on urban areas as those are main emitters being location for transport facilities, factories, power stations, waste deposits and the main part of world's population [Ken+09]. The first permanent city observatories using arrays of EM27/SUN spectrometers are emerging [Die+21].

The present work aims to quantify GHG emissions in Thessaloniki, Greece, with a pair of EM27/SUN spectrometers. Therefore, the long-term measurements with one instrument performed at the Aristotle University of Thessaloniki (AUTh) [Mer+21] are supplemented with a second instrument to create a satellite-like setup with one permanently located instrument and a second one with daily changing locations. This requires a minimal number of persons to operate the campaign. Conceptually, a box model will serve to estimate area emission fluxes (in t per km^2 per yr) of CO_2, CH_4 and CO. From the detected enhancement in trace gas concentrations, the corresponding emission (mass per time) can be inferred. The box model scales the emission to an effective area.

In the following, an outline of the structure of the present work is given. The theoretical fundamentals of atmospheric processes including the natural and anthropogenic greenhouse effect and basics of absorption spectroscopy are provided in chapter 1. In chapter 2, the foundations of the measurements are explained. It introduces main quantities like column-averaged dry-air mole fractions (DMFs), the COCCON network with its history, the used EM27/SUN spectrometers, the measurement procedure and the retrieval software `PROFFAST`. Also described in that chapter is the concept of up- and downwind measurements and the theoretical ideas of the box model to estimate area emission fluxes. Light wind conditions induce a boundary case of the box model which can be used to estimate columnar accumulations of GHG with one instrument. This case is derived as well.

In chapter 3, the data set collected during the measurement campaign in Thessaloniki is presented: first, the motivation and a general overview of the campaign are given. Then, the used setups are described: up- and downwind configurations to estimate emission fluxes as well as background measurements. The latter shall serve to determine possible deviations by arranging the spectrometers perpendicular to the air flow. The available wind and ground pressure data sets and the calculation of ground pressure levels for the different measurement sites are then presented. The calibration of the instruments to ensure the inter-comparability between them and relative to other campaigns is explained in the last part of chapter 3.

The measurement results, analysis and discussion of the Thessaloniki campaign are presented in chapter 4. First, the measurements of the background variability are considered to investigate how deviations from the ideal up- and downwind alignment effect the results. Then, the results of the up- and downwind measurement days are presented. This leads to the main goal of this work, the estimation of area emission fluxes for the most important GHGs CO_2, CH_4 and of CO. Additionally the correlations between different trace gases are analyzed to identify signatures for biomass incineration processes (CO_2 and CO) and correlated sources (CO_2 and CH_4). The results of the emission flux from up- and downwind measurements are supplemented by estimations for light wind conditions. As the applied box model is a simplistic approach for estimating emissions, a rough er-

ror consideration will be made to assess the obtained results. Finally, chapter 4 will be concluded by discussing the results. The last chapter summarizes the work and gives an outlook (chapter 5).

1. Theoretical Background

In this first chapter, theoretical concepts are introduced and provide background knowledge on processes and measurement methods. First, the composition of the Earth's atmosphere (section 1.1) and its radiative properties, including the important greenhouse effect (section 1.2), are described. The idea of Fourier-transform infrared spectroscopy (FTIR) measurements used here is explained in section 1.3.

1.1. Composition of the Earth's Atmosphere

The Earth's atmosphere is one of the most important ingredients for life on Earth: it contains the air we breathe, stabilises the temperature at the Earth's surface through the greenhouse effect (subsection 1.2.2)), creates the pressure that allows liquid water to form, and absorbs ultraviolet radiation from the Sun.

Figure 1.1 shows schematically the climate system which is composed of the atmosphere, the anthroposhere (everything made or modified by humans) and the biogeosphere. The latter can be further subdivided into the hydrosphere (water system), the biosphere (all ecosystems), the lithosphere (Earth's surface) and the cryosphere (ice and permafrost). Figure 1.1 includes feedbacks that can accelerate the climate crisis: for example, thawing permafrost soils causing methane emissions or industries influencing nearly every part of the climate system.

In order to measure and analyse trace gas emissions, it is important to understand some general processes in the Earth's atmosphere. Therefore, this section introduces its chemical composition and the trace gases it contains. The vertical structure of the atmosphere, important quantities and some basic processes in the layers are then summarised and finally the important greenhouse effect is outlined.

1.1.1. Chemical Composition and Trace Gases

Following [Möl19], the atmosphere can be seen as a reservoir filled by air. Accordingly, the hydrosphere represents the water reservoir. Air is a mixture of gases, liquids (like water droplets) and solids (like dust or snow). The gaseous (and particulate) constituents of air are shown in Table 1.1. N_2, O_2 and Ar make up around 99.96 % of the total dry air volume. The remaining gases are summed up as "trace gases". As marked in Table 1.1, some of them are inert noble gases. Most of the trace gases on the other hand have a large impact on the climate system through their ability to absorb infrared radiation. These gases are called greenhouse gases (GHGs).

No component of dry air but also contributing to the greenhouse effect is water, showing large concentration variations from almost zero to up to 3 % in the atmosphere. These

Table 1.1.: Dry remote atmosphere composition (global mean 2015-2016). The atmospheric composition is measured in remote regions of the world, away from civilization and other sources, to avoid local emissions. Considering dry air concentrations is beneficial as the water vapor concentration in the air varies from 0.5 % to 3 % [Möl19].

Substance	Formula	Mixing ratio in ppm	Behaviour in time
Nitrogen[1]	N_2	780,825	Constant
Oxygen[1]	O_2	209,432	Constant
Argon[1]	Ar	9,339	Constant
Carbon Dioxide[a,c]	CO_2	404	Increasing
Neon[b]	Ne	18.18	Constant
Helium[b]	He	5.24	Constant
Methane[a,c]	CH_4	1.845	Increasing
Krypton[b,c]	Kr	1.14	Constant
Hydrogen[a,c]	H_2	0.5	Constant
Nitrous Oxide[a,c]	N_2O	0.328	Increasing
Carbon Monoxide[a,c]	CO	0.120	Increasing
Ozone[a,c]	O_3	0.03	Variable
Particulate matter[c]	-	0.01	Variable

[1] Main atmospheric gas.

[a] Reactive trace gas.

[b] Inert trace gas (noble gas).

[c] Human influenced.

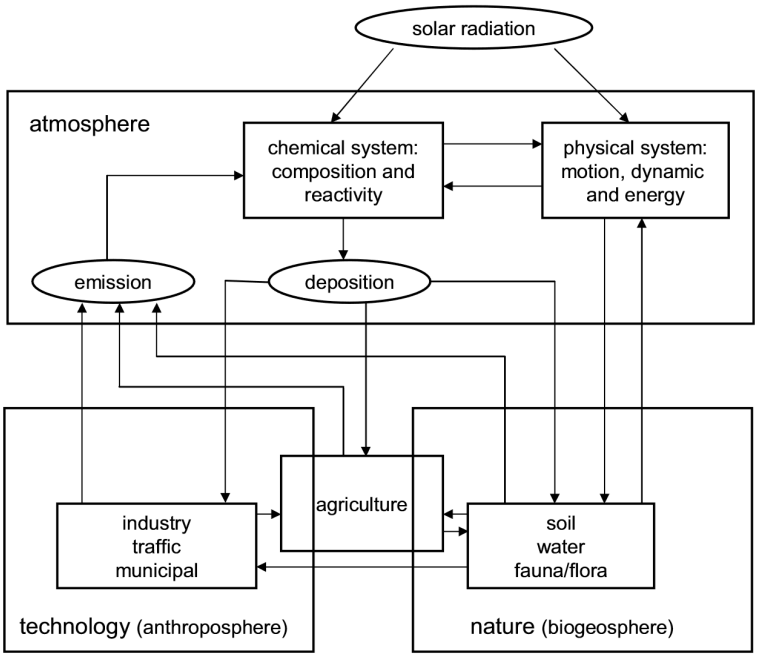

Figure 1.1.: Schematic representation of interactions between antroposhere, atmosphere and biogeosphere, constituting the climate system [Möl19].

variations are caused by the water cycle that takes place in the lower atmosphere (troposphere). As it changes state between solid (ice), liquid and gaseous (vapour), water affects weather (e.g. precipitation), energy exchange between compartments (Figure 1.1), temperature regulation and more.

1.1.2. Vertical Structure of the Atmosphere

The atmospheric matter described above is held by the Earth's gravity to form the atmosphere. By considering physical characteristics of the atmosphere, it can be split into layers. These are outlined in the following.

- The *troposphere* is the lowest part of the atmosphere, beginning at the Earth's surface up to the tropopause (at around 10 to 15 km altitude). Here, the temperature decreases linearly with height and vertical mixing of air constituents is strong. The tropopause separates the weather-influenced troposphere from the more stable stratosphere.

- In the *stratosphere*, temperature increases with height up until the stratopause (at around 45 to 55 km altitude). The vertical mixing is slow in this layer. The stratopause marks the first maximum in temperature of the atmosphere.

- *Mesosphere* is the layer between stratopause and mesopause (at around 80 to 90 km altitude) where the temperature decreases again with height. The Vertical mixing here is rapid.

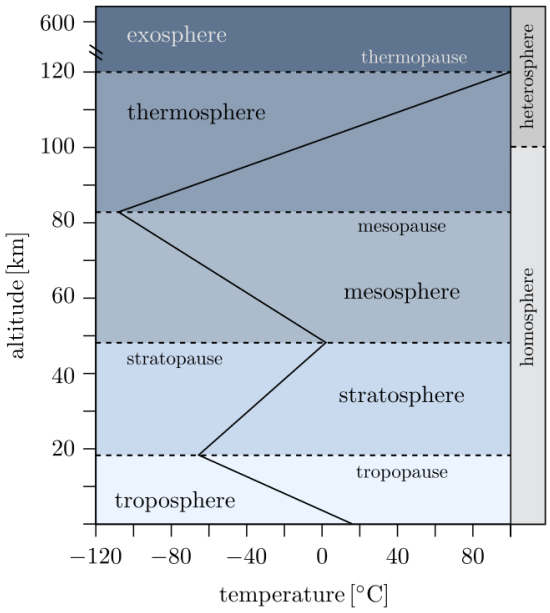

Figure 1.2.: Schematic vertical temperature profile and the different layers of the Earth's atmosphere [Dör12].

- Above the mesopause, the *thermosphere* is the outer layer of the atmosphere characterized by rapid vertical mixing through high temperatures and absorption of short-wavelength radiation by N_2 and O_2 molecules.

The lowest part of the troposphere is the planetary boundary layer (PBL). Here, the exchange of trace gases between terrestrial sources and sinks and the atmosphere takes place. This layer extends from the Earth's surface up to several hundred meters or a few kilometers and is characterized by the interaction with the surface. This includes drag on wind profiles or heat transfer on temperature profiles. Vertical mixing of e.g. trace gases depends on the vertical temperature gradient in the PBL: neutral or increasing temperature with height supports accumulation of gas emissions near the surface, while strong solar heating of the ground generates an increase of the PBL thickness associated with rapid vertical mixing across the PBL [Möl19].

1.2. Radiative Properties of the Atmosphere

In this section, interactions between solar radiation and matter are presented. After the introduction of basic properties, the absorption of radiation by matter is explained. An important property of absorption spectra are the spectral line shapes, which are outlined in the following. Then the infrared spectral range and the transmission properties of the atmosphere are then examined in more detail to finally explain the greenhouse effect.

First, basic terms will be introduced that will be applied in the following:

- Radiation strength can be expressed by different quantities depending on the application. The power of the incident radiation is referred to as *radiant flux* Φ with

the unit W. Often the radiant power is related to the incident surface, which is called *irradiance* and is given in the unit $\frac{\mathrm{W}}{\mathrm{m}^2}$. On the other hand, the *radiant intensity* is the radiation power related to the solid angle, i.e. in the unit $\frac{\mathrm{W}}{\mathrm{sr}}$. The mentioned quantities are also used as spectral quantities, i.e. related to a specific wavelength or frequency.

- Light that hits a medium is either transmitted, absorbed or reflected. The *transmittance* τ refers to the fraction of the radiation flux that is transmitted by the medium. The fraction that is absorbed is correspondingly expressed by the *absorptance* α and the reflected fraction by the *reflectance* ρ. Due to the conservation of energy, $\tau + \alpha + \rho = 1$ holds.

- The concept of a *black body* names an ideal physical body that is in thermodynamical equilibrium with its surrounding. It absorbs all incoming radiation and on the other hand emits so-called *black body radiation*. The spectrum of black body radiation for a certain temperature T follows Planck's radiation law and is isotropic:

$$B_\lambda(T) = \frac{2h \cdot c^2}{\lambda^5} \frac{1}{\exp\left(\frac{h \cdot c}{\lambda \cdot k_\mathrm{B} T}\right) - 1}, \tag{1.1}$$

  with the Planck constant h, the speed of light c and Boltzmann's constant k_B. Its maximum intensity is located at $\lambda \propto \frac{1}{T}$ according to *Wien's displacement law*. The power per area radiated by a black body is given by *Stefan-Boltzmann*'s law that reads $P = \epsilon \sigma T^4$, with ideal emissivity $\epsilon = 1$ and the Stefan-Boltzmann constant $\sigma \approx 5.670 \cdot 10^{-8} \frac{\mathrm{W}}{\mathrm{m}^2 \mathrm{T}^4}$.

- A physical body that does not absorb all incident radiation, i.e. for which $\epsilon < 1$, is often called a *grey body* and represents an approximation to a black body with the corresponding laws introduced above.

- Electromagnetic energy is absorbed and emitted in quantized portions. The quanta associated with electromagnetic radiation are the photons. One single photon contains the energy $E = h \cdot f = h \cdot c \cdot \tilde{\nu}$, related to its frequency f or wave number $\tilde{\nu} = \frac{f}{c}$.

- The fraction of shortwave solar radiation scattered back into space is the *planetary albedo* A. It is caused by diffuse reflection. This means that on a complex surface, incident light is scattered in many directions.

- The opposite process to absorption is emission, where thermal radiation is emitted from a medium. The *emissivity* ϵ is given by the fraction of the radiant flux emitted by a medium at a given temperature T relative to that of a black body.

A key property of the atmosphere is its interaction with radiation. The Sun emits electromagnetic radiation with a spectrum as shown in Figure 1.3. It extends from the ultraviolet range ($\lambda = 100 - 400\ \mu$m), through the visible ($400 - 700\ \mu$m) to the NIR (NIR) ($700 - 2500\ \mu$m).

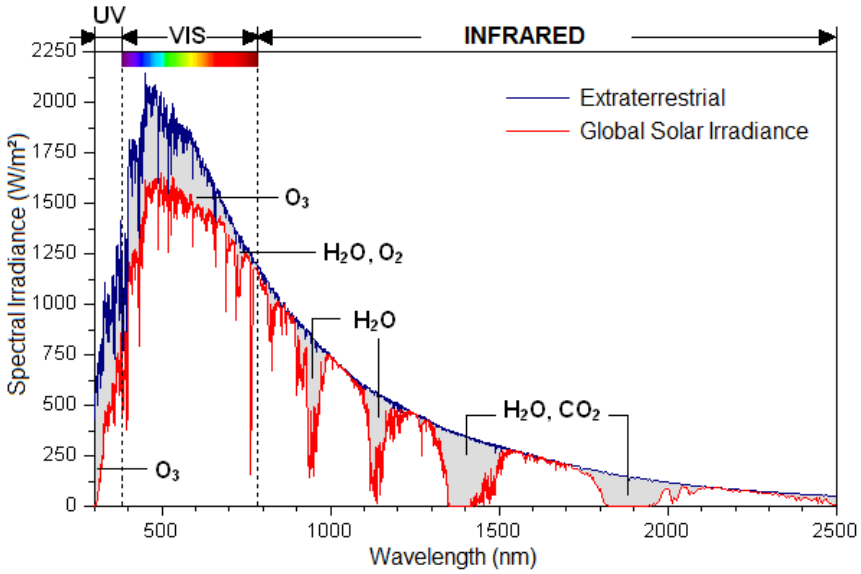

Figure 1.3.: Solar irradiance spectrum above the atmosphere (extraterrestrial) and at the Earth's surface (global solar irradiance) [Dor+11]. Irradiance names the total amount of isotropic radiant flux falling on a point of a surface. The ultraviolet (UV), visible (VIS) and near infrared part of the spectrum are marked as well as the the main absorption bands.

The irradiance measured at the outer boundary of the Earth's atmosphere (extraterrestrial, blue curve) shows the behaviour close to that of an ideal black body at 5800 K [Möl19], while the spectrum by the Earth's surface (global solar irradiance, red curve) differs from that through lower intensity in some parts of the spectrum. This is caused by absorption and scattering on atmospheric molecules and suspended particles in dependency of the light's wavelength.

Absorption as a main form of interaction between light and atmospheric particles is described in the following.

1.2.1. Molecular Absorption, Spectral Line Shapes and Radiative Transfer in the Infrared

Figure 1.3 shows a discrepancy between the spectral irradiance measured extraterrestrially and at the Earth's surface. Photons are absorbed and emitted by molecules in the atmosphere. In the infrared spectrum, these are mainly H_2O, CO_2, CH_4 and N_2O.

Information about molecular absorption and associated spectral line shapes is mainly taken from [Dem16] and [Has00].

Molecular Absorption

The absorption or emission of a photon by a molecule can be described quantum mechanically as a change of the molecule's energy eigenstate. Thereby, the photon's energy $E = h \cdot c \cdot \tilde{\nu}$ is equal to the change of the molecule's energy. Energy levels of molecules

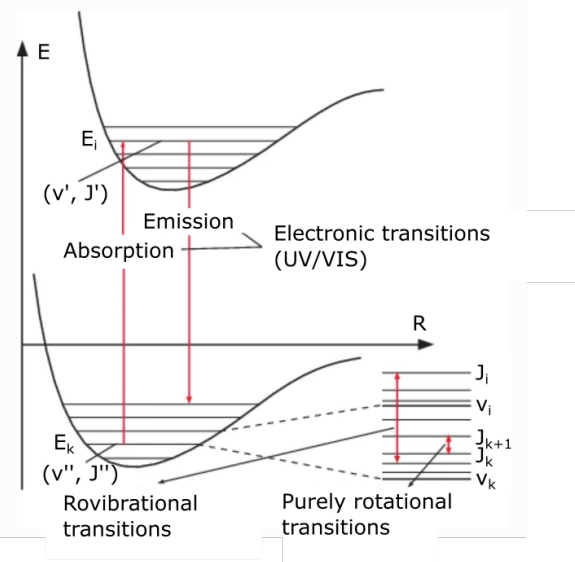

Figure 1.4.: Schematic representation of the substructure of an electronic transition of a diatomic molecule ([Dem16] with the legends translated to English). Additionally to the electronic energy levels E_i and E_k, transitions with smaller photonic energy are possible through rotational and rovibrational transitions.

can be split into electronic, rotational, vibrational and translational energy. Changes in translational energy are continuous transitions and covered by classical description. On the other hand, transitions between bound electronic, vibrational and rotational eigenstates cause well-defined discrete energy changes. Electronic energy levels are associated with those of the electrons in the molecule, while rotational and vibrational energy is largely contained in the relative motion of its nuclei.

Since the considered energy states have discrete levels, quantum numbers can be associated with them. Thereby, the state of the electrons in the orbital of a molecule is defined by the principal quantum number n, the projection quantum number[1] Λ and the spin quantum number S. Further quantum numbers come by the relative vibration (v) and rotation (J) of the nuclei. The transition probability of a molecular radiative transition is proportional to the squared matrix element of the dipole operator. For a diatomic molecule, it can be written as

$$|M_\mathrm{ik}|^2 = |\langle n_\mathrm{i}, \Lambda_\mathrm{i}, v_\mathrm{i}, J_\mathrm{i}|\mathbf{d}|n_\mathrm{k}, \Lambda_\mathrm{k}, v_\mathrm{k}, J_\mathrm{k}\rangle|^2, \tag{1.2}$$

which is non-zero for physically allowed transitions, implicating so-called selection rules (assuming dipolar transitions). The index i denotes the initial state of the molecule and k the final state.

Figure 1.4 shows the potentials of a diatomic molecule for two different electronic states ($E_\mathrm{i}(n_\mathrm{i}, \Lambda_\mathrm{i})$ and $E_\mathrm{k}(n_\mathrm{k}, \Lambda_\mathrm{k})$). The electronic potentials can be described by anharmonic Morse potentials, which are a modified parabola of the harmonic oscillator. Those include the convergence of the potential towards the dissipation energy for large internuclear

[1] Projection of the overall orbital angular momentum on the molecular axis.

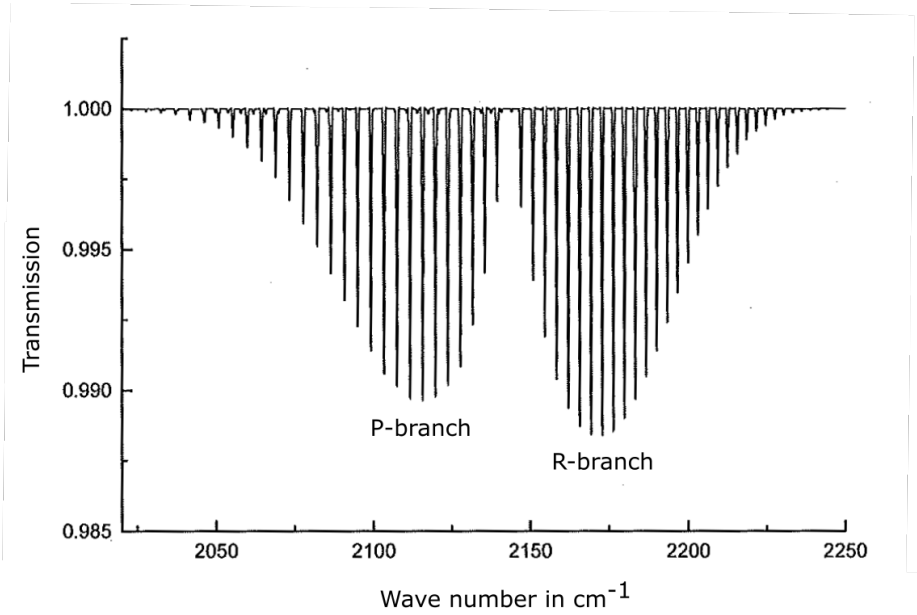

Figure 1.5.: P- and R-branch within the fundamental band of the transmission spectrum of CO (taken from [Has00] with axis labelling translated to English and additional naming of the branches).

separation $R \longrightarrow \infty$ and enable physical transitions that are not allowed in the harmonic approximation.

The selection rule for rotational transitions of diatomic molecules is

$$\Delta J = \pm 1, \tag{1.3}$$

with the physical meaning that the quantized angular momentum $\hbar = \frac{h}{2\pi}$ carried by a photon is compensated by the molecule.

Considering vibrational transitions in a harmonic approximation, the selection rule

$$\Delta v = (0, \pm 1) \tag{1.4}$$

allows transitions only between different rotational states for a constant vibrational state or rovibrational (rotation + vibration) transitions between neighboured vibrational states. In an anharmonic potential on the other hand, rovibrational transitions also for higher values of Δv are possible and called overtones. An important consequence of Equation 1.2 is that rovibrational transitions only occur for heteronuclear molecules (with two different constituents, e.g. CO). The symmetry of homonuclear molecules (e.g. O_2) leads to a vanishing electric dipole moment and therefore forbidden rovibrational transitions. Molecules with allowed transitions in the infrared spectrum are called infrared active and those without infrared inactive, respectively.

For molecules containing more than two atoms like CO_2 or CH_4, the geometry of the nuclei and their description becomes significantly more complex. Detailed presentations can be found in [Dem16] or [HS15].

The selection rules create a band structure as shown for a diatomic molecule in Figure 1.4, with different ΔE between different states of the molecule. As stated above, the energy of a photon corresponds to its wave number $\tilde{\nu}$, $E = h \cdot c \cdot \tilde{\nu}$ and the transition rules create characteristic spectral bands. The energy gaps for electronic transitions (Figure 1.4) are relatively large compared to those of rovibrational and rotational transitions. The location of a spectral line in the electromagnetic spectrum corresponds to the energy gap and therefore, the smaller energies are associated with longer wavelengths. Electronic transitions correspond to the ultraviolet and visible spectrum while rovibrational and rotational transitions to the infrared spectrum. The molecular absorption and emission of a well-defined energy leads to characteristic spectral lines. These can be split in branches, depending on the underlying selection rule:

- Spectral lines generated by rovibrational transitions with $\Delta J = +1$ are associated with the *R-branch*.
- Spectral lines generated by rovibrational transitions with $\Delta J = -1$ are associated with the *P-branch*.
- Spectral lines generated by rovibrational transitions with $\Delta J = 0$ are associated with the *Q-branch*. These transitions are only possible for molecules containing more than two atoms.

The spectral lines the fundamental rovibrational band of the CO molecule is presented in Figure 1.5.

Spectral Line Shapes

The absorption of radiation through a molecule is associated with a discrete energy. But, spectral lines feature a finite, non-zero width. This means that the energy of a transition is distributed around the discrete value. Effects that create the finite widths of spectral lines are:

- The *natural line width* corresponds with the lifetime of the particular excited state, lying in the order of $\Delta\tilde{\nu} \propto 10^{-8}\,\mathrm{cm}^{-1}$ (at $\tilde{\nu} = 1000\,\mathrm{cm}^{-1}$) [Has00] and is therefore negligibly small.
- *Doppler broadening* is caused by the thermal motion of molecules in a gas. Photons absorbed or emitted by molecules with a nonzero velocity component along the line of sight show a wavelength that is relatively shifted. Doppler broadening is a statistical effect, described by a normal distribution, which FWHM[2] lies at the order of $\Delta\tilde{\nu} \propto 10^{-3}\,\mathrm{cm}^{-1}$ (CO at $\tilde{\nu} = 2100\,\mathrm{cm}^{-1}$ and $T = 270\,\mathrm{K}$) [Has00].
- *Collision broadening* of spectral lines arises through collisions between molecules, shortening the lifetime of excited states. This effect therefore is proportional to the pressure of the gas. Being a statistical process, it can be described by a Lorentz function with a FWHM lying at $\Delta\tilde{\nu} \propto 0.1\,\mathrm{cm}^{-1}\frac{p}{10^3\,\mathrm{hPa}}$ with p in hPa.

[2] FWHM = Full width at half maximum of a given function (often applied to probability distributions). It is a measure of the width of a function's peak.

Collision broadening is proportional to the collision rate and therefore depends on pressure. Pressure decreases with height following the barometric formula that is derived in the Appendix A.1.1). On the other hand, Doppler broadening increases with temperature. Therefore, collision broadening is the dominating effect concerning line widening in the troposphere and Doppler broadening from middle stratosphere upwards. For conditions, where both effects significantly contribute to the FWHM, the resulting line shape can be approximated as a Voigt profile (convolution of Doppler and Lorentzian profiles).

Radiative Transfer in the Infrared

As mentioned before, solar radiation interacts in many ways as it propagates through the Earth's atmosphere. The corresponding transport equation of radiative transfer describes absorption, reflection and scattering processes between photons and matter. It is used in the context of ground-based remote sensing to calculate trace gas concentrations from transmitted solar radiation as observed at ground level. The following description and the equations used refer mainly to [Bal21].

Infrared radiation covers the part of the solar spectrum with long wavelengths ($\approx$ 700 nm − 1 mm [Möl19]) and therefore relatively small photonic energy. As stated above, infrared radiation is emitted or absorbed by molecules changing their rovibrational or rotational state. Furthermore, Rayleigh scattering is proportional to λ^{-4}, so the effect is negligible for infrared radiation. Mie scattering is generated by aerosols that are similar or larger in diameter than the wavelength. Under clear sky conditions, the effects of Mie scattering is negligible in case of solar absorption measurements.

Assuming that scattering processes are negligible, the equation of radiative transfer for a spectral radiant intensity I_λ can be written as:

$$\frac{\mathrm{d}I_\lambda}{\mathrm{d}s} + \kappa_\lambda \cdot I_\lambda = \kappa_\lambda \cdot B_\lambda(T). \tag{1.5}$$

The left hand side of this equation expresses the change in intensity after a path length s in the medium. On the right hand side is the decrease in radiation due to atmospheric absorption and a source term. The latter contains the assumption that atmospheric molecules are in thermal equilibrium with their environment and emit black body radiation (B_λ). Assuming thermal equilibrium implies through Kirchhoff's law that in the range of thermal radiation the emission coefficient is equal to the absorption coefficient[3].

If only direct solar radiation is considered, the source term in Equation 1.5 can be neglected, and the solution of the resulting differential equation yields Lambert-Beer's law:

$$I_\lambda(s) = B_\lambda(T) \cdot \mathrm{e}^{-\kappa_\lambda \cdot s}. \tag{1.6}$$

This law is from particular interest in the retrieval of trace gas abundances from measured solar spectra. A more detailed derivation is given in [Cha60; Has00; Kie16].

[3] If scattering processes are neglected, κ_λ equals the absorption coefficient defined as $\kappa_\lambda = -\frac{1}{\Phi_\lambda}\frac{\mathrm{d}\Phi_\lambda}{\mathrm{d}s}$ with the spectral radiant flux Φ_λ.

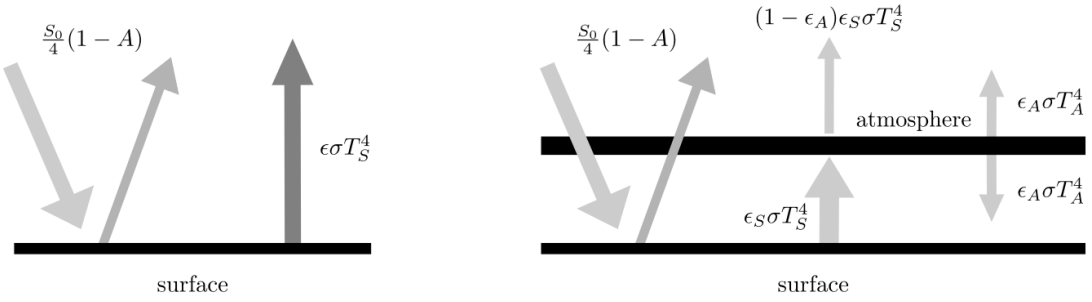

Figure 1.6.: Illustration of terrestrial energy fluxes due to incoming shortwave solar radiation and longwave thermal emission of the ground and the atmosphere [PDS12].

1.2.2. Greenhouse Effect

The greenhouse effect has a central influence on the Earth's climate system, as it is responsible for regulating and stabilising the temperature at the Earth's surface. To explain this effect, the concept of the Earth's energy budget is useful. It describes the balance between energy entering and leaving the Earth.

Figure 1.6 illustrates a model, with the atmosphere assumed to be a single layer with the behaviour of a grey body at temperature T_A. This means that the emissivity $\epsilon_\mathrm{A} < 1$ is equal to the absorptivity of the atmosphere. The Earth's surface can be assumed to be a black radiator at temperature T_S with correspondingly $\epsilon_\mathrm{S} = 1$. To clarify the discussion of the energy budget, the following terminology will be used [TFK09]:

- *Total solar irradiation* (TSI): It is measured on top of the atmosphere and given by the solar constant (time average):

$$\mathrm{TSI} = S_0 \approx 1367\,\frac{\mathrm{W}}{\mathrm{m}^2}. \tag{1.7}$$

- *Top-of-atmosphere* (TOA): The effective irradiance received at the top of the atmosphere is given by

$$\mathrm{TOA} = \frac{S_0}{4}. \tag{1.8}$$

  The factor of $1/4$ is caused by the Earth's rotation and the resulting distribution of the Sun's radiative power on the area of the hole sphere $4\pi r_\mathrm{e}^2$ while the cross section is that of a circle πr_e^2.

- *Absorbed solar radiation* (ASR): The solar energy that is absorbed on the Earth's surface is given by

$$\mathrm{ASR} = (1-A)\cdot\mathrm{TOA}, \tag{1.9}$$

  with the mean net albedo of the Earth $A \approx 0.3$.

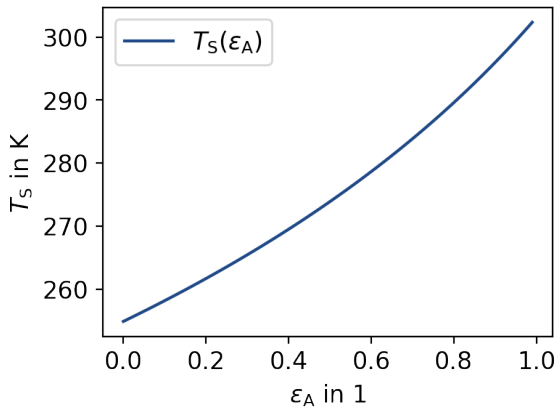

Figure 1.7.: Earth's surface temperature T_S as a function of the emissivity ϵ_A of the atmosphere for a single layer model. The Earth's surface is assumed to behave as a black body, while the atmosphere is assumed to behave as a grey body.

- *Outgoing longwave radiation* (OLR): The longwave radiation that is emitted by the Earth's surface is given by

$$\mathrm{OLR} = (1 - \epsilon_A)\, \sigma T_S^4 + \epsilon_A \sigma T_A^4. \tag{1.10}$$

  The outgoing radiant flux depends on the temperature of the Earth's surface T_S and that of the atmosphere T_A. ϵ_A denotes the emissivity of the atmosphere.

With the introduced terminology, the energy budget of the Earth is given by:

$$\mathrm{ASR} = \mathrm{OLR}. \tag{1.11}$$

Furthermore, the energy flux in the atmosphere is to be considered. The atmosphere absorbs terrestrial radiation and emits radiation both back to the Earth's surface and into space:

$$\epsilon_A \sigma T_S^4 = 2\epsilon_A \sigma T_A^4 \tag{1.12}$$

Equation 1.11 and Equation 1.12 assume the energy both on the Earth's surface and of the atmosphere to be constant. Solving the two equations for T_S gives the curve shown in Figure 1.7. From this it can be seen that the temperature of the Earth's surface for a vanishing emissivity $\epsilon_A = 0$ just takes on the value 255 K. This would be the case without the presence of an atmosphere. For the actual prevailing mean temperature of 288 K, the atmosphere's emissivity is $\epsilon_A \approx 0.8$.

The emissivity is influenced by the constituents of the atmosphere. In cloudy skies, the emissivity can be close to 1. Under clear skies, water vapour is the dominant contributor to the average emissivity ($\epsilon \approx 0.69$), while the influence of the trace gases CO_2 and CH_4 adds about 10 % ($\epsilon \approx 0.75$ [Men+17]). The important role of GHGs despite their low concentration comes through the fact that the dominant atmospheric gases N_2 and O_2 do not absorb infrared radiation. This is because of the aforementioned vanishing dipole moment of homonuclear diatomic molecules.

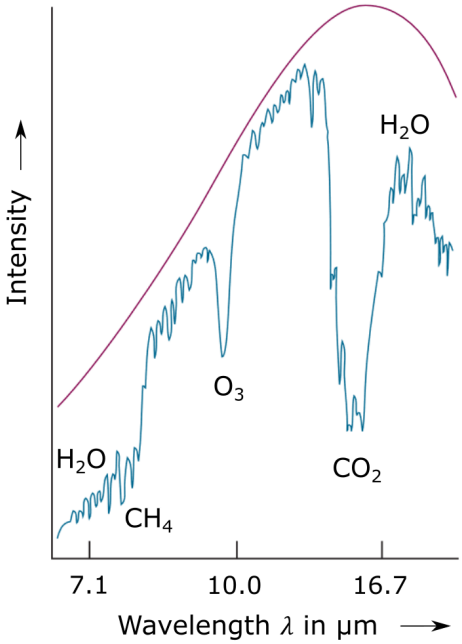

Figure 1.8.: Terrestrial IR radiation with absorption bands of main atmospheric trace gases. The red line marks the theoretical black body radiation without the presence of atmospheric absorption (taken from [APK22] with axis labelling translated to English).

Greenhouse Gases

The trace gases in the atmosphere that contribute to the greenhouse gas effect are called greenhouse gases (GHGs). The defining property is that they absorb infrared radiation that is emitted from the earth's surface.

The dominant part of the terrestrial radiative spectrum is depicted in Figure 1.8. Hereby, the red line marks the theoretical black body spectrum in absence of atmospheric absorption. It is visible that the absorption bands of CO_2 in the IR range of $\tilde{\nu} = 500 - 725\,\mathrm{cm}^{-1}$ ($\lambda = 14 - 20\,\mu\mathrm{m}$) and of CH_4 at around $1300\,\mathrm{cm}^{-1}$ ($7.7\,\mu\mathrm{m}$) lie in the main emission spectrum. CO on the other hand has its main IR absorption band at $2143\,\mathrm{cm}^{-1}$ ($4.6\,\mu\mathrm{m}$) (compare with Figure 1.5) and is therefore not categorised as a GHG.

As mentioned above, GHGs influence the emissivity of the atmosphere and thus the Earth's energy budget. The concentration of GHGs has increased measurably since industrialisation around 1800 AD: The concentration of CO_2 in the earth's atmosphere rose from 280 to over 400 ppm nowadays. CH_4 increased meanwhile from around 720 to over 1.86 ppm [IPC21]. By increasing GHG concentrations, the atmosphere can absorb more longwave radiation with a resulting positive change in the net energy flux. This is called radiative forcing (RF). Considering physical drivers of climate change, the GHGs CO_2 and CH_4 are those with the strongest RF [IPC21]. Main antropogenic sources of CO_2 are fossil burning processes. Human made sources of CH_4 are mainly livestock, the use of fossil fuels, landfills, rice cultivation and the burning of biomass.

1.3. Solar Absorption Spectroscopy for Chemical Remote Sensing

In this section, an outline of the FTIR measurement technique applied in the present work is given. The aim is to provide the main ideas and properties while for technical details or mathematical background of the underlying principles, existing sources are presented.

More detailed information can be found in previous publications [Has00; Gis12; Kie16; Fre18; Tu19].

1.3.1. Lambert-Beer Law, Transmission of the Atmosphere in the Near Infrared

After introducing the basic principles of molecular absorption and radiative transfer in the infrared, the focus will now be specifically on the properties in the NIR. This part of the electromagnetic spectrum is associated with wavelengths ranging in $0.7 - 2.5\,\mu$m ($\tilde{\nu} = 4000 - 14285\,\mathrm{cm}^{-1}$).

As discussed above, infrared radiation can be absorbed or transmitted by molecules, changing their electronic or vibrational state. What is characteristic of absorption in the near infrared is that the vibrational bands contain only overtones and combinations. Those transitions are forbidden in the harmonic approximation and therefore show a small absorptivity. This makes absorption spectra in the NIR distinguishable from those in the visible and thermal infrared spectrum as the latter are based mostly on fundamental bands that create much stronger absorptivity (around 2-100 times [WW08; Oza+21]). Another argument for spectroscopy in the NIR spectrum is the high transmittance following from low absorptivity and the corresponding relatively large penetration depth.

Remembering the simplified equation of radiative transfer in the infrared (Equation 1.5), and assuming direct propagation of solar radiation through the atmosphere, the result is Lambert-Beer's law (Equation 1.6):

$$I_\lambda(s) = B_\lambda(T = 5800\,\mathrm{K}) \cdot \mathrm{e}^{-\kappa_\lambda s}. \tag{1.13}$$

A more realistic expression for the radiative intensity that is transmitted through a probe of gas is derived in [Has00] (with $S = I_f$). I_f here gives the intensity for the specific transition of the state with energy E_1 into E_2:

$$I_f = \frac{c^2}{8\pi f^2}\frac{ng_2}{Q(T)}\mathrm{e}^{-E_2/k_\mathrm{B}T}\left[\exp\left((E_2 - E_1)/k_\mathrm{B}T\right) - 1\right]A_{21}, \tag{1.14}$$

with the number density n of the probe and the dimensionless line profile function g_2 The partition function $Q(T)$ includes all bound states of the radiative interacting system. Other determining quantities for the radiative intensity are the Einstein coefficients for spontaneous emission A_{21} and the energies of the associated states $E_{1,2}$. The calculation of the transition rates and the position of the lines is practically not possible. This issue can be treated by using data base numbers to identify trace gas abundances from absorption spectra. Below, this is explained in more detail.

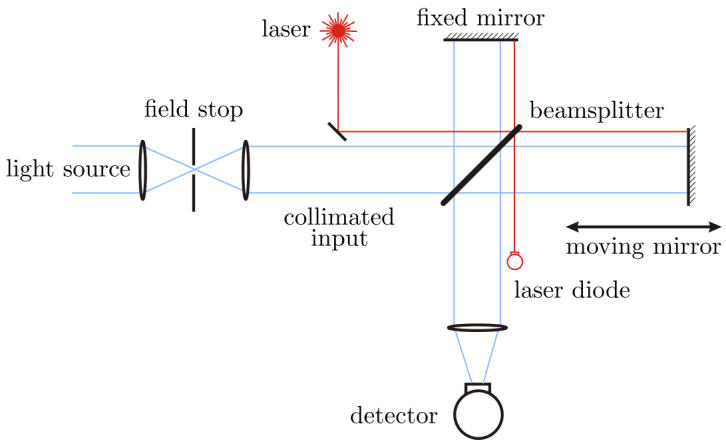

Figure 1.9.: Sketch of a Michelson interferometer as the basis of FTIR spectroscopy ([Kie16], adapted from [Gis12]).

1.3.2. FTIR Spectroscopy

The measurement principle used in the present work to observe solar absorption spectra is FTIR spectroscopy. Since they do not require an artificial light source, this measurement technique is referred to as "passive ground-based remote sensing". This technique finds application in various fields of research as a means of spectral analysis. It is explained in the following.

The basic construction of every FTIR spectrometer is a Michelson interferometer as shown in Figure 1.9. After being collected and collimated, the incoming radiation is divided by the beam splitter and redirected to two mirrors, whereas one is movable and one in fixed position. The resulting optical path difference (OPD) produce a measurable interference pattern when the beams are recombined at the beam splitter. A Helium-Neon (HeNe) reference laser with wavelength $\lambda = 632.988\,\mathrm{nm}$ is used to determine the OPD caused by the moving mirror.

The sensor records an interferogram $I(x)$, expressing the intensity I of the measured light for a given OPD x. The interferogram is connected with the spectrum by Fourier transformation (derived e.g. in [Kie16]):

$$\begin{aligned} I(x) &= \mathscr{F}\left[S(\tilde{\nu})\right] = \int_{-\infty}^{\infty} \mathrm{d}\tilde{\nu} \exp\left(2\pi \mathrm{i}\, \tilde{\nu} \cdot x\right) S(\tilde{\nu}), \\ S(\tilde{\nu}) &= \mathscr{F}^{-1}\left[I(x)\right] = \int_{-\infty}^{\infty} \mathrm{d}x \exp\left(-2\pi \mathrm{i}\, x \cdot \tilde{\nu}\right) I(x) \end{aligned} \tag{1.15}$$

with the wave number $\tilde{\nu} = \frac{1}{\lambda}$. In the practical realization, the interferogram is truncated to a limited range (up to the maximal optical path difference (MOPD)) and sampled in discrete steps (which requires a limitation of spectral bandwidth). The range of the wave number $\tilde{\nu}$ determines the spectrum covered by the interferometer. Due to the connection of the wave number $\tilde{\nu}$ and the OPD x as conjugated variables, the maximum coverage follows

from the range Δx. This link is given by the Nyquist–Shannon sampling theorem [Nyq28; Sha49]:

$$\tilde{\nu}_{\max} - \tilde{\nu}_{\min} < \frac{1}{2\Delta x}, \tag{1.16}$$

saying that the recorded resolution in terms of wave numbers is limited by the technically realizable difference in OPD Δx. Spectral frequencies outside this range lead to systematic distortion of the spectrum, as these contributions are folded back into the observed range. As mentioned above, the interference pattern of the HeNe reference laser measures the OPD and thus the sampling interval. For the FTIRs used in this work, the spectral high folding limit is set to $\tilde{\nu} = 15798\,\mathrm{cm}^{-1}$, in agreement with a sampling interval of 316.5 nm.

The OPD is limited by the MOPD which is defined by the optical setup. This restriction sets the spectral resolution of the spectrometer and the distance between adjacent independent spectral sampling points, which amounts to $\Delta\tilde{\nu} = \frac{1}{2 \cdot \mathrm{MOPD}}$. To apply this restriction to the spectrum $S(\tilde{\nu})$, the measured spectrum results from a convolution of the irradiated spectrum with a boxcar function in the interval of $|x| <$ MOPD. To avoid non-physical side lobes arising in $S(\tilde{\nu})$, a so-called numerical *apodization* function is applied to $I(x)$. As this procedure decreases the spectral resolution, a balance has to be found. For the spectrometers used in this work, the choice for the apodization function falls on the Norton-Beer medium function [Bee92]. The overall resolution is not unambiguous due to different criteria and in case of the EM27/SUN spectrometers set to

$$\Delta\tilde{\nu} = \frac{0.9}{\mathrm{MOPD}}. \tag{1.17}$$

Restricting the interferogram with the boxcar function further brings up another instrument to describe the effects of misalignment of the spectrometer's optical setup: the *instrumental line shape (ILS)*. A sufficiently narrow spectral line takes the shape of the ILS in the measured spectrum. The ILS depends on optical properties of the spectrometer like misalignment, optical aberrations or a phase error. To determine the ILS for an individual spectrometer, specific parameters are derived from experiments that are either gas cell measurements [HBP99; Has12] or open path measurements [Fre+15; Tu19; Alb+22a].

Further detailed information on FTIR spectroscopy can be found among others in [Bee92; Has00; Kie16].

1.3.3. Retrieval of Trace Gas Concentrations from Spectral Observations

The main interest in atmospheric ground-based remote sensing lies in the observation of trace gas abundances. Thus, the lines in the measured NIR spectrum must be translated to concentrations of corresponding gases. This step includes the identification of the line position $\tilde{\nu}$ and the inverse calculation of gas concentration from line intensities and line width based on laboratory reference data.

As mentioned above, this is done by using tabular figures collected in databases (a-priori profiles). Since the 1960s, the high-resolution transmission molecular absorption database (HITRAN) finds application in atmospheric remote sensing. It contains line

specific data that is measured under laboratory conditions. "Originally the database contained for each molecular transition the following basic parameters: (1) resonant frequency; (2) line intensity; (3) air-broadened half width; and (4) lower state energy (as well as unique quantum identifications). Additional parameters have recently been provided which permit new capabilities for remote sensing in the atmosphere and capabilities to deal with non local thermodynamic equilibrium effects in the upper atmosphere." [Rot+87]. Since then, the HITRAN data has been maintained, modified and updated on a regular basis [Rot+13; Gor+22].

To determine the measured gas quantities, the laboratory profiles are fitted to the measured spectra. For this purpose, a-priori trace gas profiles, the ground pressure at the measurement site, pressure profiles and temperature profiles are required. The a-priori volume mixing ratio (VMR) profiles of each retrieved trace gas are scaled to achieve the best agreement between measured and modelled spectrum using a least squares fit. VMR profiles are calculated by fully coupled chemical climate models and cover the entire atmosphere. The pressure and temperature profiles serve to determine the temporal variability of the trace gases. The calculation of trace gas abundances from absorption spectra is a so-called forward problem. This means that the connection between the trace gas abundances and spectra must be found by inversion. Since this connection is not linear, a linearisation is carried out by a Taylor expansion [Rod00; Fre18]. A measure of how the retrieval indicates deviations against the a priori VMR profile is the vertical sensitivity. Since the retrieval only scales the a-priori profile, the vertical sensitivity indicates a possible deformation of the spectral lines. The temperature profile indicates the height dependence of the temperature. The temperature dependence of the absorption spectra can then lead to errors in the calculation of the number of molecules if the height assignment is incorrect.

2. Passive, Ground-Based Remote Sensing for Monitoring GHG Emissions

In this chapter, the passive ground-based remote sensing technique used in the present work is introduced more specifically. In the first part, the COllaborative Carbon Column Observing Network (COCCON) and its activities are introduced in section 2.1. The second part of the chapter deals with up- and downwind measurements and the derivation of emission fluxes with a box model in section 2.2. The latter is explained in detail and the formulae for emission fluxes are derived.

2.1. The COCCON Network

Here, the history and ideas of COCCON, the FTIR Bruker^{TM} EM27/SUN with the corresponding measurement procedure and the retrieval procedure with the `PROFFAST` software are explained.

2.1.1. History and Idea

COCCON[1] was established by Karlsruhe Institute of Technology (KIT) in 2014 [Fre+19] to operate the Bruker^{TM} EM27/SUN spectrometer within a framework that provides reliable instrument performance and data processing. COCCON is intended to complement the existing Total Carbon Column Observation Network (TCCON) and its high resolution FTIRs Bruker^{TM} IFS125HR by offering greater flexibility in terms of transport and location, lower costs and easier operation. An important aspect is the centralisation within the COCCON network, with the instruments being developed at Bruker^{TM} in Ettlingen in collaboration with KIT. Specifically, each new instrument is tested at KIT, optimised and calibrated before deployment. The optimization contains the diagnosis and correction of a non-ideal optical alignment, double-passing, channeling, non-linearity problems, solar tracker problems or inaccurate positioning of the second detector [Fre18]. An EM27/SUN reference instrument, located in Karlsruhe, Germany, is regularly calibrated against a Bruker^{TM} IFS125HR and is used to calibrate other instruments before shipment or after a measurement. More details on this procedure are given below in subsection 2.1.2. Information is regularly exchanged within the network in order to ensure consistent measurement quality and ongoing adaptation of procedures. This includes the development and maintenance of the `PROFFAST` retrieval software and the sharing of operational knowledge. Collected data from calibration measurements, campaign data or long-term measurements is stored and shared centrally across the network.

[1] `https://www.imk-asf.kit.edu/english/COCCON.php`

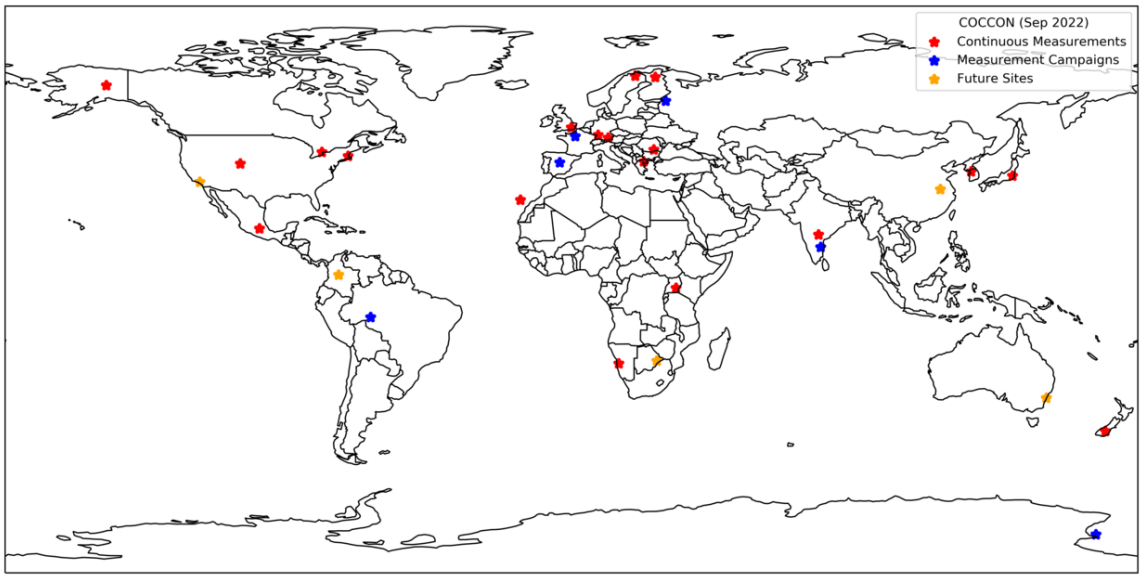

Figure 2.1.: The measurement sites of the COCCON Network. The campaign analysed in the present work is not marked on the map because it has not yet been published.
(`imk-asf.kit.edu/english/COCCON.php`, December 2022).

The main scientific goal of COCCON is the quantification of regional sources and sinks of GHGs and their temporal course in the atmosphere. Thereby, the portability, long-term stability and significant precision at the same time enables to perform measurements even in remote parts of the world. Campaigns were conducted for example on the research vessel Polarstern [Kla+15a] and in major cities, complementing the existing permanent monitoring sites.

Considering Europe, there has been measurement campaigns in Paris (France) [Fre+15], Berlin (Germany) [Has+15; Fre+15], St. Petersburg (Russia) [Mak+21; Alb+22b], Madrid (Spain) [Tu+22] and Poznan and Rzecin (Poland). Not all of them are marked on the world map in Figure 2.1 for various reasons. E.g. the Berlin campaign was performed in 2015 before the COCCON network was established, or the corresponding results are not published yet. The campaign considered in this work is not marked yet since the results are still in the process of publication. Furthermore, the map shows a spreading over nearly all parts of the world, but still with a enhanced density in Europe.

2.1.2. EM27/SUN Spectrometer

At the heart of the COCCON network are the Bruker^{TM} EM27/SUN FTIR spectrometers. Their general structure is illustrated and described below. The given technical data can be found in [Fre+19], while a detailed description of the instrumentation, but with deprecated technical specifications, can be found in [Gis12].

Figure 2.2 shows the interior of an EM27/SUN spectrometer. Following the path of light, the first part of the instrument is the solar tracker, which uses the `CamTracker`

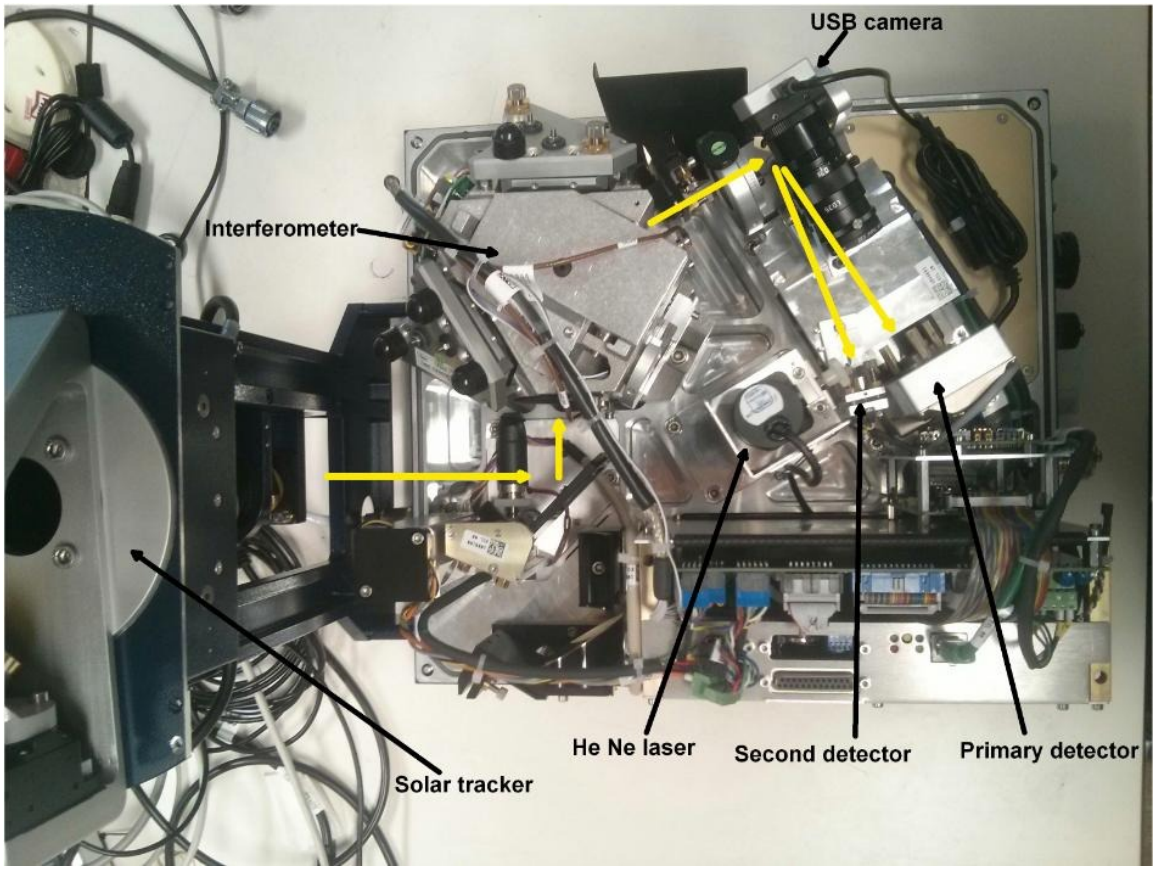

Figure 2.2.: Inner setup of an EM27/SUN. The yellow arrows mark the light path (taken from [Fre18]).

program [Gis+11] (using the USB camera) to capture the ellipse of the Sun and track its daily progress. The collimated beam then passes through the wedged entrance window, which filters radiation with a wavelength greater than 750 nm (long pass filter) to block stray light on the detector. Additionally, the beam is tilted against the optical axis to prevent channeling at the detector. Then, the beam enters the interferometer that is a RockSolid^{TM} pendulum interferometer with two cube corner mirrors and a calcium fluoride (CaF_2) beam splitter. As described above, the HeNe laser serves to measure the OPD of the interferometer. After recombination, the beam leaves the interferometer and passes a ≈ 5 mm aperture to avoid non-linear detector response and to control optical aberrations [Fre18]. Before the beam is led onto the detector, further optical elements are placed: a 90° off-axis paraboloid mirror (127 mm focal length) focuses the beam on a 0.6 mm field stop that yields a semi Field-of-View of 2.36 mrad (corresponding to 56 % of the Sun's diameter). The field stop is tilted to avoid channeling. A diffusor is placed in front of the detector to provide non-linear and ILS effects on the detector due to uneven illumination.

As shown in Figure 2.2, the EM27/SUN measures with two detectors. The second channel has been added to expand the covered spectral range [Has+16]. Therefore, the beam is split by a decoupling mirror that is installed right after the paraboloid mirror. This extension is meanwhile in common use in the COCCON network. For clarity, the detectors are presented separately in the following:

- The first detector implemented in the EM27/SUN spectrometer consists of a Hamamatsu^{TM} photo diode made from indium gallium arsenide (InGaAs) and offers a spectral coverage of about $5500 - 11000\,cm^{-1}$. Variable transmission of the atmosphere can be corrected through DC-coupling of the detector. The detector covers the NIR bands of CO_2, CH_4, H_2O and O_2.
- The second detector is a room-temperature extended InGaAs diode and covers the spectral range of $1900 - 5250\,cm^{-1}$. This allows measuring the trace gases CO, N_2O and HF (hydrogen fluoride).

Figure 2.3 shows the solar NIR spectrum measured by an EM27/SUN spectrometer with the two channels described, highlighted in different colours. The EM27/SUN spectrometer offers a spectral resolution of $0.5\,cm^{-1}$, equivalent to a MOPD of 1.8 cm [Alb+22a].

Calibration and ILS Adjustment using the TCCON Standard

The COCCON reference instrument SN37 is calibrated at KIT relative to the high resolution spectrometer Bruker^{TM} IFS125HR which is used in the frame of the TCCON network. The IFS125HR is also a FTIR spectrometer operated at a resolution of $0.02\,cm^{-1}$. Further IFS125HR are measuring from the far infrared up to the UV spectrum. For the calibration of the EM27/SUN, the IFS125HR can be set to perform measurements in the near infrared at low resolution with double-sided interferograms. These can be analysed with `PROFFAST` as those of the SN37 to perform the calibration. In the past years, there has been many studies concerning the calibration of the EM27/SUN against the IFS125HR. For more detailed information therefore see [Fre+19; Has+15; Kla+15a].

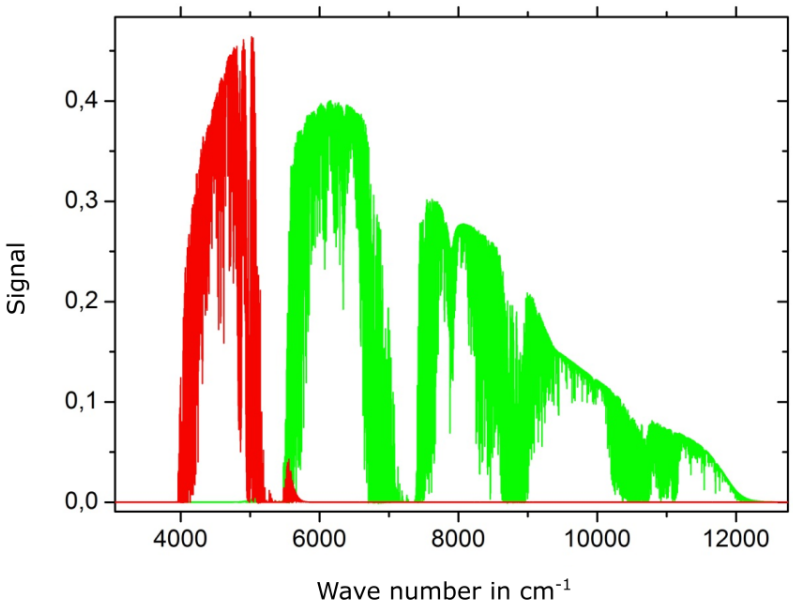

Figure 2.3.: Solar NIR absorption spectrum measured by an EM27/SUN. The green colored spectrum is measured by the first channel and the red by the second (taken from `https://www.imk-asf.kit.edu/english/3225.php` with adapted axis labelling).

Also part of the calibration process is the determination of ILS parameters by open path measurements. The present work does not include those open path measurements. For detailed description, see [Alb+22a]. The stability of the EM27/SUN spectrometers concerning ILS characteristics has been shown in rough transport and operational conditions for several years [Fre+15; Fre+19].

2.1.3. Measurement Procedure

In the following, the measurement procedure is explained, describing the practical steps needed to collect spectrometric data with a Bruker^{TM} EM27/SUN. The description is in chronological order.

Firstly, an even surface of around 3 m^2 must be found. The path of the sun during the planned measurement period must be taken into account, and possible shadows from buildings or trees must be avoided. Within the presented campaign in Thessaloniki, the EM27/SUN is transported in an appropriate box with protecting foam material. This box can be used to place the spectrometer on. The spectrometer should be pointing south to make it easier to find the solar disc with the `CamTracker`. Besides the spectrometer, the laptop, a data logger (measures pressure, humidity and temperature, see subsection 3.4.1), a GPS sensor, the solar panels and the electronic control unit with the battery are installed next to the spectrometer (for the specific setup of the Thessaloniki campaign, see section 3.3). Next, the listed individual parts are connected with cables: the spectrometer and the laptop are supplied with power, the laptop is connected to the spectrometer via an Ethernet cable and the data logger and GPS sensor are connected to the laptop. Then the spectrometer is switched on, as it takes some minutes for the HeNe to reach thermal equilibrium. After the laptop has booted up, the system time given by the GPS sensor is checked first. When the `CamTracker` is started, activated and pointed at the sun, the shape of the solar disk is checked and the `CamTracker` settings are corrected if necessary.

Next the `OPUS` software[2] is started and under *Advanced Data Collection* first the correct `XPM` file for the measurement is selected. Then under *Check Signal* the necessary amplification of the two channels is considered and changed if necessary. If the signal shows an amplitude in the range of $\approx$ 16000 cts in the morning hours, the present position of the maximum of the interferogram is saved with *Safe peak position*. Now the measurement is started by selecting the measurement cycles, whereby a sufficiently high number is selected and the measurement can be aborted at the end.

When the standard `OPUS` measurement procedure file is selected, a a co-added interferogram calculated from 10 consecutive scans is recorded approximately every minute. The first interferograms should be checked for any irregularities. Especially deflections at the sides of the interferogram indicate errors in the measurement process. Subsequently, the setup is regularly checked for correctly seated cables, power supply and focusing of the solar disk.

[2]provided by Brukder^{TM} `https://www.bruker.com/en/products-and-solutions/infrared-and-raman/opus-spectroscopy-software.html`

2.1.4. Retrieval Procedure with PROFFAST

The measurement outcome of an EM27/SUN spectrometer are interferograms that are recorded by the OPUS software (see subsection 2.1.3 above). Two main steps are needed to retrieve trace gas concentrations from the raw interferograms: the first is called preprocessing and contains the transformation of the interferogram into an absorption spectrum. KIT provides the open-source tool PROFFASTpreprocess, that has been developed in the framework of the COCCON-PROCEEDS project supported by ESA.

As a second step, the observed spectrum is used to obtain trace gas concentrations. Therefore, the line width and strength are analyzed by a radiative transfer code in combination with an inversion scheme to fit synthetic spectra to the measured spectra. The a-priori VMR profiles of each retrieved trace gas are scaled for achieving the best agreement between measured and modelled spectrum (least squares fit). The VMR profiles of the main trace gases in the atmosphere are well known and fairly constant in the troposphere [Wun+11]. The associated open source software is called PROFFAST and is developed at KIT.

Recently, a new interface for PROFFAST called PROFFASTpylot is developed by L. Feld and B. Herkommer at KIT. It automates the data processing using python and significantly reduces the effort of the retrieval.

The software packages can be found on https://www.imk-asf.kit.edu/english/3225.php. In the present work PROFFAST Version 2.2 in combination with PROFFASTpylot Version 1.1. are used for the retrieval. PROFFAST uses the same a-priori files as generated for the TCCON data analysis [Lau+22].

2.1.5. Column-Averaged Dry-Air Mole Fractions

Trace gas abundances can be expressed in various forms. One way is to use total column amounts, which is the total number of molecules in the measured column in the atmosphere:

$$TC = \int_{z_0}^{\infty} \mathrm{d}z \rho_{\mathrm{N}}, \tag{2.1}$$

with the number density of a trace gas ρ_{N} and the ground height z_0. This quantity is therefore dependent on the height of the measurement site, which leads to limited comparability.

Mole fractions, on the other hand, are defined as the molar amount of a tracer relative to the molar amount of air sampled. Locally, air can be assumed to be described by the ideal gas law (Equation A.4). Therefore, volume mixing ratios are equal to molar mixing ratios and the corresponding units are ppm(v) (parts per million). The use of dry air as a reference medium further enhances the significance due to the widely varying ratios of water vapour in the atmosphere. Column-averaged dry-air mole fractions (DMFs) are widely used in the field of atmospheric research and defined as

$$X_{\mathrm{gas}} = \frac{TC_{\mathrm{gas}}}{TC_{\mathrm{DryAir}}}. \tag{2.2}$$

The volume mixing ratio of oxygen (O_2) in the atmosphere can be assumed to be constant at 0.2095,

$$X_{O_2} = \frac{TC_{O_2}}{TC_{\text{DryAir}}} = 0.2095, \tag{2.3}$$

yielding for the column-averaged DMF:

$$X_{\text{gas}} = \frac{TC_{\text{gas}}}{TC_{O_2}} \cdot 0.2095. \tag{2.4}$$

With this definition, systematic uncertainties induced by the ground pressure are reduced. It is the method used for the COCCON retrievals. As shown in [Gis12], the retrieval of trace gas abundances still depends on the barometric pressure.

2.1.6. XAIR as an Indication of System Stability

Besides column-averaged DMFs of the trace gases CO_2, CH_4 and CO, X_{AIR} is another important quantity in the analysis of FTIR measurements. The auxiliary quantity X_{AIR} is calculated from the O_2 column, which is co-observed in the NIR spectral region. It compares the amount of spectroscopically derived O_2 with the O_2 column predicted based on ground pressure and H_2O column. X_{AIR} is used to recognize problems with instrumental stability, solar tracking performance, timekeeping, errors in assumed ground pressure, and other disturbances. Examples are time synchronization errors, errors with measuring ground pressure, the `CamTracker` not ideally pointing at the sun or changes in the optical construction of the device. X_{AIR} is derived in the following.

By definition, the DMF of dry air X_{AIR} is equal to 1 (Equation 2.2):

$$X_{\text{AIR}} = \frac{TC_{\text{DryAir}}}{TC_{\text{DryAir}}}. \tag{2.5}$$

The total column of dry air can be expressed in different ways. One way is using ground pressure and the H_2O column (subsection A.1.2):

$$TC_{\text{DryAir}} = \frac{P_{\text{gr}}}{\langle g \rangle \cdot m_{\text{DryAir}}} - TC_{H_2O} \cdot \frac{m_{H_2O}}{m_{\text{DryAir}}}, \tag{2.6}$$

where m name the molecular masses of the corresponding compound. Using

Another way of determining the total column of dry air is using Equation 2.3. Equation 2.5 then gives:

$$X_{\text{AIR}} = \frac{0.2095}{m_{\text{DryAir}}\, TC_{O_2}} \left[\frac{P_{\text{gr}}}{\langle g \rangle} - TC_{H_2O} \cdot m_{H_2O} \right]. \tag{2.7}$$

This expression gives a relation between the measured barometric ground pressure and the measured column of oxygen. The second term in the brackets is a correction because ground pressure is created not only by dry air but wet air. An ideal measurement and retrieval process as well as accurate pressure measurements would lead to $X_{\text{AIR}} = 1$ as mentioned above. Currently, X_{AIR} is normalised to 1 with individual instruments ranging in 1 ± 0.005.

2.2. Up- and Downwind Measurements and Box Model for Emission Monitoring

The quantity that describes the greenhouse gas emissions of a given area is the area emission flux, given in mass of a tracer gas per area and time. It can then be compared, for example, at different locations, possible emission hotspots, or for different times. Two or more spectrometers set in an up- and downwind alignment can be used to estimate emission fluxes. This means that the upwind instrument is reached first by the wind flow. Therefore, the downwind instrument is able to measure potential emissions from a source between the instruments. After presenting the idea of city campaigns, the box model that is used in the present work to calculate emission fluxes from trace gas concentrations is explained. In the end, a variation of the box model for light wind conditions is derived.

2.2.1. COCCON City Campaigns

Particular interest for measuring GHGs lies on urban areas as those are main emitters being location for transport facilities, factories, power stations, waste deposits and the main part of world's population [Ken+09]. In the framework of COCCON, campaigns were carried out in cities before this work. The aim here is to measure urban GHG emissions with a comparable measurement method, as the inventories often consist mainly of figures from municipalities or companies. Furthermore, the portable EM27/SUN are suitable to change location quickly by car, which makes it possible to cover different areas of a city. A similar approach with two spectrometers and the application of a box model has been used in St. Petersburg [Mak+21]. Further city campaigns are described in [Fre+15; Has+15; Mak+21; Tu+22; Alb+22b; Sag+22]. Additionally, first permanent city observatories using arrays of EM27/SUN spectrometers are emerging [Die+21].

2.2.2. Box Model for Up- and Downwind Conditions

A sketch of the box model that is introduced in the following is shown in Figure 2.4. One assumption is that emissions are constant over a distance L. In a box of size L multiplied by the height of the mixing layer z_i, the concentration C of the pollutant is taken to be constant as well. The distance L practically is the distance between the instruments, ideally covering potential GHG sources. The idea behind this assumptions is that in an urban area it's useful to combine different smaller point sources of pollution into larger area sources. Further, it is assumed that the wind speed v is independent of the altitude and the wind's trajectory connects the two devices. The wind first flows past the upwind instrument that measures background concentrations C_b. The instrument in the box is positioned downwind and measures concentrations C. Those concentrations above the mixing layer will be denoted as C_a. The mixing depth z_i should correspond to the planetary boundary layer (PBL) thickness. From this point, it is therefore noted as z_PBL. These quantities are connected by the following continuity equation [HBH82]:

$$L\, z_\mathrm{PBL}\, \frac{\partial C}{\partial t} = L\, Q_\mathrm{a} + v\, z_\mathrm{PBL}\, (C_\mathrm{b} - C) + L \frac{\partial z_\mathrm{PBL}}{\partial t} (C_\mathrm{a} - C)\,. \tag{2.8}$$

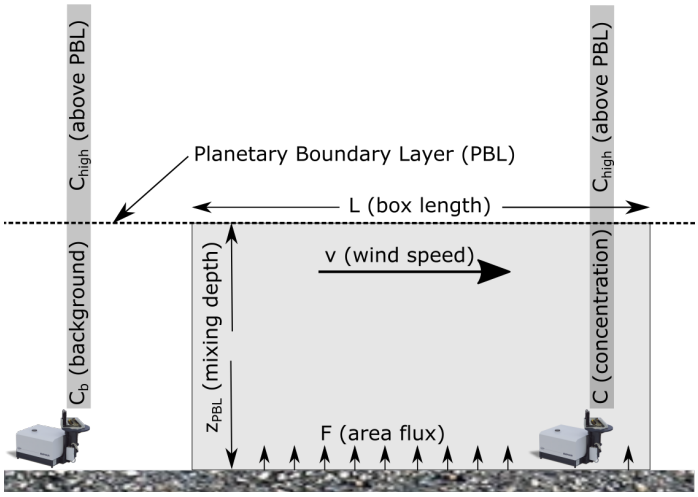

Figure 2.4.: Box model for up- and downwind conditions. Wind flows from the upwind instrument (background) towards the downwind instrument (in the box). From the detected enhancement of trace gas concentrations, the corresponding emission (mass per time) can be inferred. The used box model refers to an effective area and the area emission flux therefore can be interpreted as the emissions of an area source (Pablo Schmid, March 2022).

This equation now can be simplified for a steady-state-scenario meaning $\frac{\partial C}{\partial t} = 0 = \frac{\partial z_{\mathrm{PBL}}}{\partial t}$:

$$Q_{\mathrm{a}} = \frac{v\, z_{\mathrm{PBL}}\ (C - C_{\mathrm{b}})}{L}. \tag{2.9}$$

The units are as follows:

$$[Q_{\mathrm{a}}] = \frac{\mathrm{kg}}{\mathrm{m}^2\,\mathrm{s}} = \left[v \cdot z_{\mathrm{i}} \cdot (C - C_{\mathrm{b}}) \cdot L^{-1}\right] = \frac{\mathrm{m}}{\mathrm{s}} \cdot \mathrm{m} \cdot \left(\frac{\mathrm{kg}}{\mathrm{m}^3}\right) \cdot \mathrm{m}^{-1}. \tag{2.10}$$

Equation 2.9 contains mass concentrations C and C_{b} respectively. The aim is to express the area flux by the column-averaged DMFs X_{gas}, because this quantity contains less systematic errors than the total column amounts. (subsection 2.1.5). For that, further calculations are necessary.

The first step is getting the mass density from the particle density. Therefore, the number of particles N can be calculated via the amount of substance n, the mass of the gas in the volume m and the molar mass M. N_{A} denotes the Avogadro constant. Thus,

$$C = \frac{m}{V} = \frac{M \cdot n}{V} = \frac{M \cdot N}{N_{\mathrm{A}} \cdot V} = \frac{M}{N_{\mathrm{A}}} \cdot \rho_{\mathrm{N}} \tag{2.11}$$

$$\Rightarrow \rho_{\mathrm{N}} = \frac{N_{\mathrm{A}}}{M} \cdot C \tag{2.12}$$

The vertical column between the FTIR instrument and the sun contains a certain number of molecules that is why there is a density of particles ρ_{N} in this volume. The total column amount of a certain gas is the projection of all these molecules on a certain

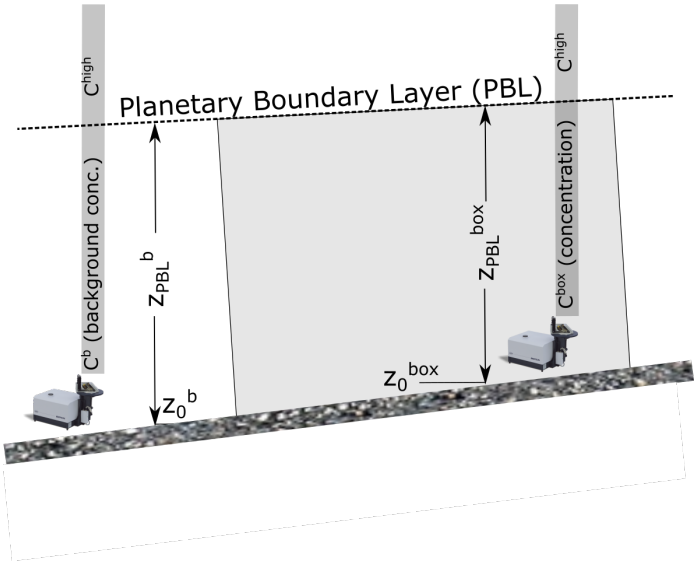

Figure 2.5.: Refined box model with measuring sites at different altitudes (Pablo Schmid, November 2022).

area: $[TC] = \left[\int_{z_0}^{\infty} \mathrm{d}z\, \rho_\mathrm{N}\right] = \frac{\text{molecules}}{\text{m}^2}$. Obviously, TC depends on the ground level of the instrument z_0. Therefore in Figure 2.5, a more realistic version of the box model of Figure 2.4 is shown. With a few assumptions, it is possible to "level" the box model again using column-averaged dry-air mole fractions X_gas. As in Equation 2.9, it will later be useful to work with differences between concentrations in the box and in upwind direction before the box (background concentration):

$$TC^\mathrm{box} - TC^\mathrm{b} = \int_{z_0^\mathrm{box}}^{\infty} \mathrm{d}z\, \rho_\mathrm{N}^\mathrm{box} - \int_{z_0^\mathrm{b}}^{\infty} \mathrm{d}z\, \rho_\mathrm{N}^\mathrm{b} \tag{2.13}$$

$$= \int_{z_0^\mathrm{box}}^{z_\mathrm{pbl}^\mathrm{box}} \mathrm{d}z\, \rho_\mathrm{N}^\mathrm{box} - \int_{z_0^\mathrm{b}}^{z_\mathrm{pbl}^\mathrm{b}} \mathrm{d}z\, \rho_\mathrm{N}^\mathrm{b} + \int_{z_\mathrm{pbl}^\mathrm{box}}^{\infty} \mathrm{d}z\, \rho_\mathrm{N}^\mathrm{box} - \int_{z_\mathrm{pbl}^\mathrm{b}}^{\infty} \mathrm{d}z\, \rho_\mathrm{N}^\mathrm{b} \tag{2.14}$$

$$= \frac{N_\mathrm{A}}{M_\mathrm{gas}} \left[\int_{z_0^\mathrm{box}}^{z_\mathrm{pbl}^\mathrm{box}} \mathrm{d}z\, C^\mathrm{box} - \int_{z_0^\mathrm{b}}^{z_\mathrm{pbl}^\mathrm{b}} \mathrm{d}z\, C^\mathrm{b} + \int_{z_\mathrm{pbl}^\mathrm{box}}^{\infty} \mathrm{d}z\, C^\mathrm{high} - \int_{z_\mathrm{pbl}^\mathrm{b}}^{\infty} \mathrm{d}z\, C^\mathrm{high} \right], \tag{2.15}$$

where the last two terms vanish because of the following assumptions:

- The PBL has the same height for both sites ($z_\mathrm{pbl}^\mathrm{b} = z_\mathrm{pbl}^\mathrm{box}$). For a small lateral range as in the area of a city and considering the constant volume of thePBL, this is a reasonable assumption.
- The concentration above thePBL, C^high, is the same for both integrals (already assumed in Equation 2.15).

This then yields:

$$TC^{\text{box}} - TC^{\text{b}} = \frac{N_A}{M_{\text{gas}}} \left[\int_{z_0^{\text{box}}}^{z_{\text{pbl}}} \text{dz}\, C^{\text{box}} - \int_{z_0^{\text{b}}}^{z_{\text{pbl}}} \text{dz}\, C^{\text{b}} \right] \tag{2.16}$$

$$= \frac{N_A}{M_{\text{gas}}} \cdot \left[z_{\text{pbl}} \left(C^{\text{box}} - C^{\text{b}} \right) - z_0^{\text{box}} \cdot C^{\text{box}} + z_0^{\text{b}} \cdot C^{\text{b}} \right], \tag{2.17}$$

where the box model assumption $C^{\text{b}}, C^{\text{box}} = \text{const. in } [0, z_{\text{pbl}}]$ is applied within the integral. Now, there are two terms depending on the altitude of the measuring sites. This shows the z_0 dependency of the total column amount.

As seen above in Equation 2.2, total columns and column-averaged dry-air mole fractions are connected like[3]:

$$X_{\text{gas}} = \frac{TC_{\text{gas}}}{TC_{\text{DryAir}}}, \tag{2.18}$$

yielding:

$$X_{\text{gas}}^{\text{box}} - X_{\text{gas}}^{\text{b}} = \frac{TC_{\text{gas}}^{\text{box}}}{TC_{\text{DryAir}}^{\text{box}}} - \frac{TC_{\text{gas}}^{\text{b}}}{TC_{\text{DryAir}}^{\text{b}}}. \tag{2.19}$$

The goal is to bracket out TC_{DryAir} in Equation 2.19 out as a factor. Therefore, investigating the z_0 dependency is necessary: For small differences in height, the difference in ground pressure can be assumed to be linear: $P_{\text{gr}} \propto -z_0$. As derived above in Equation 2.17, TC is proportional to z_0, leading to $TC_{\text{DryAir}} \propto z_0$. As the maximum difference in altitude of the measuring sites in the Thessaloniki campaign are $\Delta z_0 \approx 100m$, the maximum difference in P_{gr} is in a range of 1 %. Considering the campaign data from Thessaloniki, TC_{H_2O} shows maximum differences for two sites at the same time around $\Delta TC_{H_2O} \approx 1\,\%$, too. Putting all together, one can find a maximum variation of TC_{DryAir} for two sites at the same time of $\Delta TC_{\text{DryAir}} \approx 1\,\%$. With this argumentation and Equation 2.17, Equation 2.19 simplifies to:

$$X_{\text{gas}}^{\text{box}} - X_{\text{gas}}^{\text{b}} = \frac{1}{TC_{\text{DryAir}}} \left(TC_{\text{gas}}^{\text{box}} - TC_{\text{gas}}^{\text{b}} \right) \tag{2.20}$$

$$= \frac{N_A}{TC_{\text{DryAir}} \cdot M_{\text{gas}}} \cdot \left[z_{\text{pbl}} \left(C_{\text{gas}}^{\text{box}} - C_{\text{gas}}^{\text{b}} \right) - z_0^{\text{box}} \cdot C_{\text{gas}}^{\text{box}} + z_0^{\text{b}} \cdot C_{\text{gas}}^{\text{b}} \right]. \tag{2.21}$$

To further simplify this formula, and following the argumentation above, $z_0^{\text{b}} = z_0^{\text{box}} = z$ is set. z lies in a range of 1 to 4 % of the PBL and with this argument, the term $z \left(C_{\text{gas}}^{\text{box}} - C_{\text{gas}}^{\text{b}} \right)$ in Equation 2.21 can be neglected. Finally, the formula connecting concentrations C and mole fractions X_{gas} reads:

$$X_{\text{gas}}^{\text{box}} - X_{\text{gas}}^{\text{b}} = \frac{N_A \cdot z_{\text{pbl}}}{TC_{\text{DryAir}} \cdot M_{\text{gas}}} \left(C_{\text{gas}}^{\text{box}} - C_{\text{gas}}^{\text{b}} \right). \tag{2.22}$$

[3] An expression for TC_{DryAir} containing the ground pressure P_{gr} is derived in the Appendix A.1.2.

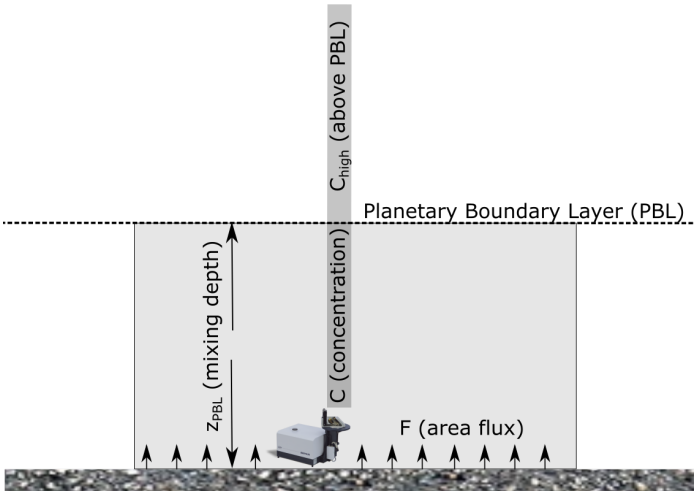

Figure 2.6.: Box model for light wind conditions assuming a slow mixing rate. The effective area that corresponds to the area emission flux is associated with the area of the measured column (Pablo Schmid, November 2022).

2.2.3. Flux Formula for Up and Downwind Measurements

Combining Equation 2.9 and Equation 2.22, one finds:

$$Q_\mathrm{a} = \frac{TC_\mathrm{DryAir} \cdot v}{L} \cdot \frac{M_\mathrm{gas}}{N_\mathrm{A}} \cdot \left(X_\mathrm{gas}^\mathrm{box} - X_\mathrm{gas}^\mathrm{b}\right) \tag{2.23}$$

The usual unit of area flux is $\frac{\mathrm{t}}{\mathrm{km}^2\,\mathrm{yr}}$. Thus, another conversion is done:

$$\begin{aligned} Q'_\mathrm{a} &= \frac{TC_\mathrm{DryAir} \cdot v}{L} \cdot \frac{M_\mathrm{gas}}{N_\mathrm{A}} \cdot \left(X_\mathrm{gas}^\mathrm{box} - X_\mathrm{gas}^\mathrm{b}\right) \cdot 31536 \cdot 10^6 \\ &\equiv \boxed{\frac{TC_\mathrm{DryAir} \cdot v}{L} \cdot k_\mathrm{gas} \cdot \left(X_\mathrm{gas}^\mathrm{box} - X_\mathrm{gas}^\mathrm{b}\right) =: F_\mathrm{UpDown},} \end{aligned} \tag{2.24}$$

with the gas-specific constant $k_\mathrm{gas} = \frac{M_\mathrm{gas}}{N_\mathrm{A}} \cdot 31536 \cdot 10^6$. Equation 2.24 will be used for following application. Values for M_gas for a specific molecule can be calculated from the atomic masses given in the periodic table of elements.

2.2.4. Model for Calm Wind Conditions

Assuming low wind speed $v_\mathrm{Wind} \to 0$, the continuity equation in Equation 2.8 yields a different solution. Low wind speeds change the up- and downwind box model with two instruments into one with only one instrument measuring local emissions, illustrated in Figure 2.6.

The basic continuity equation reads

$$L\, z_\mathrm{PBL}\, \frac{\partial C}{\partial t} = L\, Q_\mathrm{a} + v\, z_\mathrm{PBL}\, \left(C_\mathrm{b} - C\right) + L \frac{\partial z_\mathrm{PBL}}{\partial t} \left(C_\mathrm{a} - C\right).$$

For low wind speeds, two assumptions can be made:

1. In certain time intervals, there is a measurable change in concentration in time, meaning $\frac{\partial C}{\partial t} \neq 0$.
2. Light wind yields to slow transportation of gases. That means slower mixing of emissions from in and outside the box. The assumption then is equal concentrations in and outside the box, $C = C_{\mathrm{b}}$.

Together with the mixing layer z_{PBL} still being constant in time, these assumptions lead to the following equation:

$$z_{\mathrm{PBL}} \frac{\partial C}{\partial t} = Q_{\mathrm{a}}. \tag{2.25}$$

With the same arguments as for the up and downwind case (subsection 2.2.2), a similar expression to Equation 2.22 can be found:

$$X_{\mathrm{gas}} = \frac{N_{\mathrm{A}} \cdot z_{\mathrm{pbl}}}{TC_{\mathrm{DryAir}} \cdot M_{\mathrm{gas}}} \cdot C_{\mathrm{gas}}, \tag{2.26}$$

yielding

$$\boxed{F_{\mathrm{light}} = TC_{\mathrm{DryAir}} \cdot k_{\mathrm{gas}} \cdot \frac{\partial X_{\mathrm{gas}}}{\partial t},} \tag{2.27}$$

with the same gas specific constant k_{gas} as defined with equation (Equation 2.24).

The area flux obtained in Equation 2.27 now corresponds to local time-wise concentration changes and the area of the measured column. This solution of Equation 2.8 is a boundary solution as $v_{\mathrm{Wind}} = 0$ is a rare situation. Due to that, a systematical uncertainty is expected.

3. Measurement Campaign in Thessaloniki and Collection of the Data Set

In this chapter, an overview is given about why, how and what kind of data has been collected in the Thessaloniki campaign. The scientific and political motivation to measure GHGs in Thessaloniki are outlined in section 3.2. The measurement setups and corresponding expectations are discussed in section 3.3. Then, the availability and quality of necessary external data sets are presented in subsection 3.4.1. Finally, the calibration process and possible issues are explained in section 3.6.

3.1. Motivation for a Campaign in Thessaloniki

The determining structural aspect with regard to Thessaloniki is the cooperation between KIT and Aristotle University of Thessaloniki (AUTh). Marios Mermikgas from AUTh is performing long-term measurements with an EM27/SUN in Thessaloniki since January 2019 [Mer+21]. Comparing to the already performed campaigns in the COCCON framework (subsection 2.1.1), the geographical position is an argument for a campaign in Thessaloniki. It is located in the southwestern part of Europe which is not covered by previous campaigns.

3.2. Overview of the Measurement Campaign in Thessaloniki

This section describes the relevant characteristics of Thessaloniki from the viewpoint of the measurement campaign and the general ideas of measuring GHGs there.

Thessaloniki is a major European city with a population of around 800'000 [Hel22] in the total urban area. A high proportion of the cities traffic is based on fossil fuels. Further, the city is interesting because of its industry, being home to a harbour, a refinery, a cement factory and an airport (see Figure 3.1). Additionally, on the western outskirts of Thessaloniki, around the city of Chalastra, the largest rice fields in Greece are located. Watered rice fields are effective methane sources [SSB14]. The traffic, the industry and the rice fields are major sources of long-lived GHG like CH_4 and CO_2.

In a topographical perspective, the city is bound by the Thermaic Gulf on its southwest and by Mount Chortiatis from the northeast. The urban area itself is not flat but rises steadily from 0 to over 100 m a.s.l. in a north-easterly direction. The slope of the city also manifests itself in different heights of the measurement sites (Table 3.1).

The climate in Thessaloniki can be classified as BSk (Cold semi-arid climates) according to Köppen climate classification [Bec+18]. Prevailing wind situations in Thessaloniki

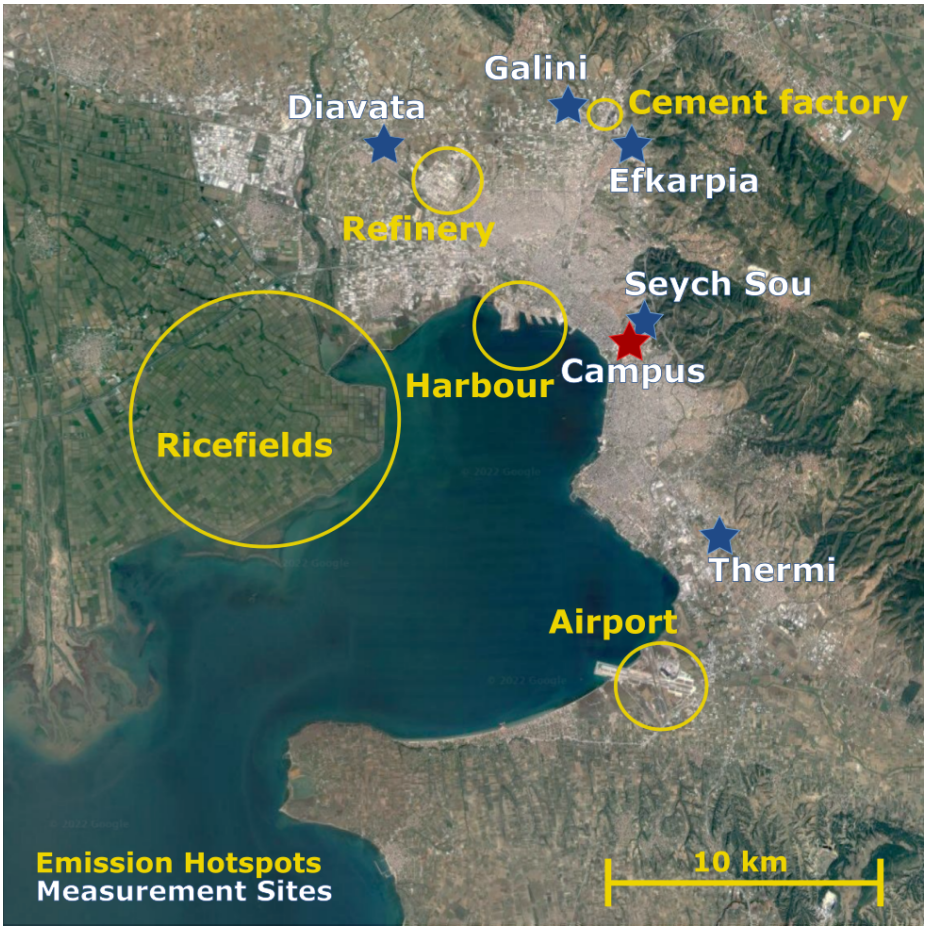

Figure 3.1.: Thessaloniki map with measuring sites and emission hotspots. "Campus" means either Meteorology or Physics building. The "Thermi" site is at the ΚΕΔΕΚ research center near the municipality of Thermi (Map data ©*Google Maps*, July 2022; created by Lena Feld). Maps shown in figures below are build from the same data.

Table 3.1.: Measurement Sites Thessaloniki Campaign

Site	Latitude in °N	Longitude in °E	Altitude in m a.s.l. GPS[a]	Map[b,c]
Meteorology	40.63105	22.95808	53.0 ± 1.2	34 + 8 = 42
Physics	40.63365	22.95654	62.9 ± 3.4	40 + 21 = 61
Galini	40.70284	22.93412	132.5 ± 4.0	121
Efkarpía	40.69048	22.95714	138.8 ± 0.3	129
Seych Sou	40.63581	22.96711	157.1 ± 4.4	145
Diavatá	40.68879	22.85468	17.2 ± 2.0	15
Thermi	40.56448	22.99496	84.2 ± 7.2	61 + 10.5 = 71.5

[a] Mean value ± σ for n measurement days at the corresponding site. GPS data is obtained by the GPS tracker attached to the measurement computer mainly for time synchronization.
[b] from `https://www.freemaptools.com/elevation-finder.htm` (2022/12/06)
[c] Height site = altitude + eventually estimated height building (3.5 m for each floor for Physics and Thermi, 4 m for Meteorology)

during the campaign were either a light sea breeze from southern or SSW direction or a stronger wind coming from north-western direction[1].

Two EM27/SUN (SN96 and SN52) are used throughout the campaign. Besides the side-by-side measurements for the relative calibration of the two EM27/SUNs, two general setups are applied in this campaign. An up- and downwind setup, where the wind trajectory ideally connects the two sites and background measurements, where the devices are positioned orthogonal to the prevailing wind direction.

As mentioned above, Marios Mermikgas is performing long-term measurements since January 2019 [Mer+21]. For the campaign, this brings the advantage of having one EM27/SUN (SN52), the knowledge and humanpower already on site. A second instrument (SN96) was calibrated to the COCCON reference instrument (SN37) in Karlsruhe and then shipped to Thessaloniki (see subsection 3.6.2). For the campaign, Marios Mermikgas and Thomas Panou from AUTh continue their measuring at the AUTh Campus (red star in Figure 3.1) while the SN96 device is used as a "satellite device" (blue stars). This means the placement of the SN96 device can change on a daily basis depending on the wind situation while the SN52 has a fixed position at the AUTh Campus. The measuring stations are selected so that as many wind directions as possible can be covered by the instrument arrangements (compare to Figure 3.1).

The Thessaloniki campaign was performed in two time periods: Lena Feld and Marios Mermikgas collected a first set of data with two FTIRs in October 2021 [Fel+21]. An extended campaign was then carried out in summer 2022 between May and July having more staff (Lena Feld, Marios Mermikgas, Thomas Panou and Pablo Schmid) and thus more mobility. More humanpower in this case is necessary mainly to transport the satellite instrument to the variable measurement sites.

[1] `https://meteo3.geo.auth.gr/stations/clim_data.htm`, December 2022

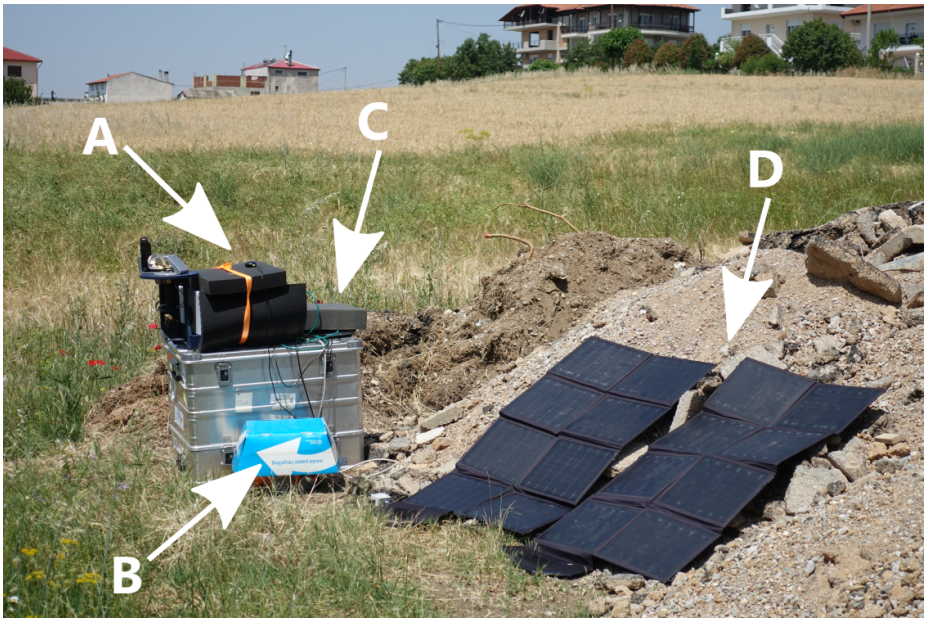

Figure 3.2.: SN96 measuring setup at the Galini site during Thessaloniki campaign:
A: EM27/SUN standing on top of its transport box, covered by foam material for heat protection.
B: Covered battery and electronic control unit.
C: Laptop with connected data logger, GPS sensor and Ethernet cable for EM27/SUN; also covered by foam material.
D: Solar panels.

3.3. Measurement Setup and Expectations

Having introduced the general settings of the Thessaloniki campaign, some more detailed information on the measuring procedure is given in this section.

The measurement standard for the EM27/SUN is described in subsection 2.1.3. Aiming to run one EM27/SUN (the SN96) as a satellite device on variable sites in and around the city, a self-sufficient power supply is needed. For this reason, a solar-cell power supply consisting of a 12 V lead gel battery, an electronic control unit and two solar panels with 100 W peak power each are used (constructed by Jochen Gross from KIT IMK-ASF). The electronic control unit contains mainly two DC/DC converters (19 and 24 V) to supply laptop and EM27/SUN. Further, heat protection is necessary due to temperatures reaching above 40 °C in sunny spots. Therefore, the foam material protecting the instrument whilst transport is used. The full setup can be seen in Figure 3.2.

3.3.1. Up- and Downwind Setup

After the short outline in the previous section, the up- and downwind measurement setup is introduced here in more detail. Further, some estimations are made on what results and possible retrieved quantities might be expected. The estimation of GHG emission from concentration gradients is the main interest of this work. Ideally, the emission strength in

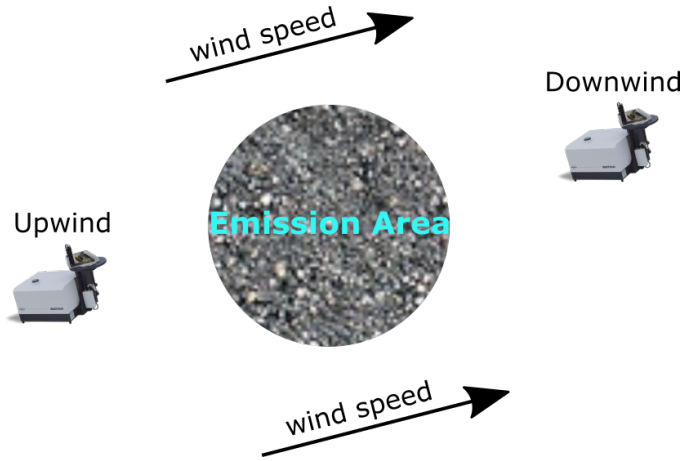

Figure 3.3.: Sketch of the up- and downwind setup (EM27/SUN images from `https://www.bruker.com`, December 2022)

the area between the instruments could be estimated from the concentration differences $\Delta X\text{gas} = X\text{gas}(\text{Downwind}) - X\text{gas}(\text{Upwind})$ for a well-known wind field.

For up- and downwind setups, the following naming convention is used from here:

- **Campus** device is the EM27/SUN SN52 located at the AUTh Campus, either at Meteorology or Physics site. The location of this instrument is marked by red color on attached maps and by a red curve in data plots.
- **Satellite** device is correspondingly SN96 collecting measurements on variable sites around the Campus device. It is marked by blue color.

Figure 3.3 illustrates the idea of up- and downwind setups. The ideal case would be a wind trajectory connecting Campus and satellite device. According to Figure 3.3, upwind corresponds to "background" in the previous introduction of the box model. Simply said, the wind trajectory starts at the upwind location and ends at the downwind location. The downwind location thus ideally measures trace gases emitted in the area in between both instruments. Therefore, the starting point for locating the satellite device is the predicted wind direction and strength (usually the morning before). Due to the satellite setup, two setup possibilities exist for each wind direction: the Campus instrument is located either upwind or downwind (and the satellite instrument correspondingly vice versa).

3.3.2. EDGAR Based Area Emission Fluxes and Inverse Calculations

In the present work, the up- and downwind setup is the basis for estimating emission fluxes of GHGs, in particular CH_4 and CO_2, using the box model introduced in subsection 2.2.2. Before retrieving emissions from the campaign's results, data base driven and inverse calculations are performed to give a rough idea what to expect.

The EDGAR data base (Emissions Database for Global Atmospheric Research[2]) [Eur21; Eur22] provides emission numbers for CO_2 and CH_4 from 1970 to 2021 in the unit of tons

[2] `https://edgar.jrc.ec.europa.eu/dataset_ghg70`

Table 3.2.: Estimated area emission flux in 2021 based on EDGAR data base numbers. The area of and around Thessaloniki is covered in the grid defined by 22.8 °E to 23 °E in Longitude and 40.5 °N to 40.7 °N in Latitude. As the chosen coverage is larger than the urban area of Thessaloniki, the obtained flux is scaled to the latter.

Tracer	Area flux in $\frac{t}{km^2 yr}$
CO_2	23'746.089
CH_4	136.875

Table 3.3.: Through inverse calculation estimated values for ΔXCO_2 and ΔXCH_4. $\Delta Xgas$ is the difference of measured DMFs. The instruments are located in a distance of L and the wind direction is ideally parallel to the instrument alignment (wind speed v).

		Distance L in m		
Gas	Wind Speed v in $\frac{m}{s}$	1000	8000	10000
ΔXCO_2 in ppm	2	0.02389	0.19114	0.23892
	5	0.00956	0.07645	0.09557
	10	0.00478	0.03823	0.04778
ΔXCH_4 in ppm	2	0.00038	0.00302	0.00378
	5	0.00015	0.00121	0.00151
	10	0.00008	0.0006	0.00076

per year on a on a grid map divided into 0.1° x 0.1° squares. For the following estimation, the numbers from 2021 are utilized. As the unit used in this work is tons per year and km^2, the lateral and longitudinal distance has to be converted to the metric scale. The used formula ("Haversine" formula) can be found in [Gad10], while the Earth's radius that is needed for this conversion is taken to be $r = 6378\,km$[3]. To cover the area of the city by the grid, the ranges of 22.8 °E to 23 °E in longitude and 40.5 °N to 40.7 °N in latitude are used (compare to Table 3.1). As the chosen coverage of $376.340\,km^2$ is larger than the urban area of Thessaloniki, the obtained flux is scaled to the latter that is $111.703\,km^2$[4].

The estimated area emission fluxes for CO_2 and CH_4 in 2021 are given in Table 3.2 and agree within an order of magnitude compared to previous measurements in other cities [Has+15; Mak+21].

The main quantity to analyse in the present work are differences of column-averaged DMFs of CO_2 and CH_4 (and CO which is not given in the used EDGAR data base). To get an idea what to expect for those, an inverse calculation of the box model for up- and downwind measurements (subsection 2.2.2) is done. Therefore, a perfect up- and downwind setup is assumed with some realistic values for the distance L between both instruments and

[3] https://nssdc.gsfc.nasa.gov/planetary/factsheet/earthfact.html

[4] https://en.wikipedia.org/wiki/Thessaloniki, in January 2023

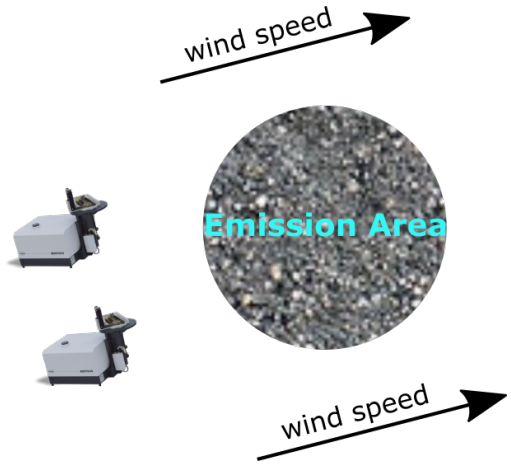

Figure 3.4.: Sketch of the background measurement setup (EM27/SUN images from `https://www.bruker.com`, December 2022)

wind conditions parallel to their alignment with wind speed v. As realistic distances L for the campaign's possible up- and downwind setups, values of 1000 m (Campus-Seych Sou), 8000 m (Campus-Thermi) and 10000 m (Campus-Diavatá) are taken. The EDGAR based values for area emission flux are finally used to obtain exemplary values for ΔXCO_2 and ΔXCH_4 from Equation 2.24[5]. The results can be seen in Table 3.3. ΔXCO_2 lies in a range of 0.001 % and 0.057 % relative to an expected DMF of 418 ppm and ΔXCH_4 in 0.004 % and 0.199 % (relative to 1.90 ppm).

3.3.3. Background Setup

As explained in the previous section, the upwind located instrument in the up- and downwind setup measures the background concentration in the case of an ideal alignment. Because the real situation deviates, the lateral variability of the background is figured out to learn about possible systematic variations. If the variability of the background concentration is large, the interpretation of the up- and downwind setup is problematic: one cannot distinguish if the difference between the instruments comes from fluctuations in background or from emissions between the instruments. The background variability is measured by placing the two instruments in upwind position orthogonal to the prevailing wind direction as shown in Figure 3.4. An interesting parameter to explore is the distance between the instruments.

As mentioned in section 3.2, there are two main wind configurations in Thessaloniki whilst the present campaign: light sea breeze from south-western direction and stronger wind from the mainland in north-western direction (compare with Figure 3.1). Especially the sea breeze configuration gives opportunity to different alignments of the instruments, e.g. the combination Thermi-Campus (larger distance $\approx$ 8 km) or Physics-Meteorology (smaller distance $\approx$ 0.3 km).

[5]The gas specific constant k is defined with the values for the molar masses as given in Table 4.4. For TC_{DryAir}, the mean value for all campaign days is calculated from $TC_{\mathrm{O_2}}/0.2095$ (Equation 2.3) with a value of $TC_{\mathrm{DryAir}} = 2.16 \cdot 10^{29}\,\mathrm{m}^{-2}$.

Table 3.4.: Overview of available pressure data sets

Instrument	Location	Accuracy	Interval
Vaisala PTB330	Physics	±0.15 hPa[a]	5 min
Davis Instruments Vantage Pro 2	Thermi (ΚΕΔΕΚ)	±1.0 hPa[b]	10 min
PCE-THB40 data logger	Variable	±2 hPa[c]	1 min

[a] Total absolute accuracy between 500 and 1100 hPa [Bar].
[b] Total absolute accuracy between 540 and 1100 hPa [Dav].
[c] Total absolute accuracy between 1001 and 1100 hPa [PCE].

For background measurements with sea breeze and small distance between the instruments, the expected variations are relatively small because the air coming from sea is well mixed without strong local emission sources. A variability in the order of the side-by-side measurements would underline the assumption that a non-ideal up- and downwind alignment concerning wind situation has no large impact in the resulting emission flux.

For the background variability in a setup with larger distance, a larger variability is expected. Local sources like the harbor could cause greater concentration gradients between the instruments, laying in a similar order as the results from the up- and downwind setup (Table 3.3).

3.4. Determination of the Ground-Pressure at the Measurement Sites

As discussed above in subsection 2.1.5, the `PROFFAST` retrieval requires the ground pressure at the measurement site to calculate column-averaged DMFs from total column abundances. Ground pressure names the barometric pressure measured at the location of the spectrometer. For the analysis of campaign data, different sources of pressure measurements were available. These data sets are introduced in subsection 3.4.1. The determination of ground pressure for each measurement site is explained in subsection 3.4.2.

3.4.1. Available Pressure Data Sets

The available pressure data sets are presented in Table 3.4. They are described in detail in the following.

As described in subsection 2.1.3, with each EM27/SUN measurement, a PCE-THB40 Data Logger collects values for pressure, temperature and humidity data every minute. Additionally, the data loggers can store data permanently on a SD card, which is important determine differences in pressure between different sites (subsection 3.4.2). The data loggers are not calibrated to absolute pressure level and have a relatively low accuracy. Furthermore, the timestamp of the record shows a certain drift. Pressure recorded by the data logger will be noted as p_{PCE}.

The most sophisticated source for ground pressure data in this data set is a Vaisala PTB330 pressure sensor, installed in October 2021 on the roof of the Physics Department

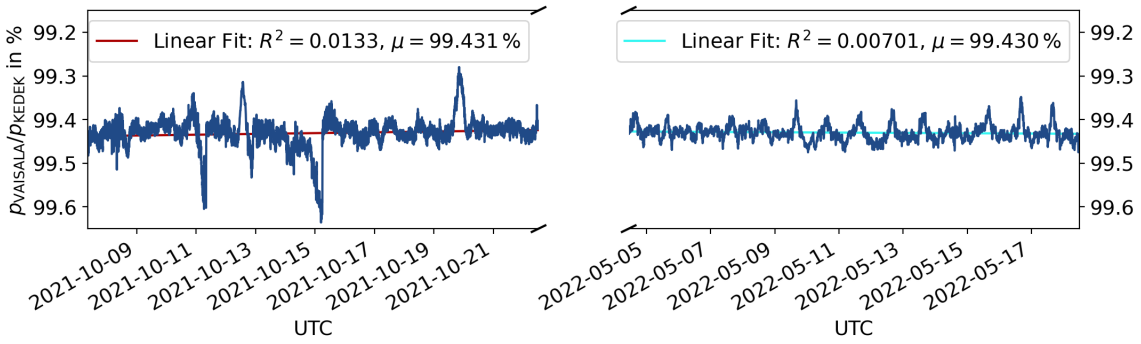

Figure 3.5.: Comparison of KEΔEK and Vaisala pressure data. The linear fits both show small R^2 and small difference in μ meaning a negligible drift.

building of AUTh. It has the best overall accuracy of all used sensors and is calibrated to offer a total accuracy of 0.15 hPa. Further, the altitude of the sensor itself is well-known. Unfortunately, the data set collected by the Vaisala is relatively small (7 out of 31 campaign days) due to technical problems. Pressure recorded by the Vaisala sensor will be noted as p_{Vaisala}.

At the KEΔEK research center (located at the measurement site in Thermi), a Davis Instruments Vantage Pro 2 weather station is positioned on the roof. Here, the altitude of the sensor is not precisely known. Pressure recorded at KEΔEK will be noted as p_{Kedek}.

Considering the absolute calibration and the known altitude of the Vaisala instrument as a major advantage, this data set will be taken in the `PROFFAST` retrieval. Due to lack of data coverage, the Vaisala data can only be taken as a reference and another data set is calibrated to it. The pressure data set used for further analysis is the KEΔEK pressure calibrated relative to the Vaisala sensor:

$$p_{\text{ref}} = \overline{\left(\frac{p_{\text{Vaisala}}}{p_{\text{Kedek}}}\right)} \cdot p_{\text{Kedek}}, \tag{3.1}$$

where the mean value is formed over all joint measurement days in October 2021 and summer 2022.

In Figure 3.5, the percentage deviation of the Vaisala relative to the KEΔEK pressure data is shown in the time intervals when both have taken measurements. To find a possible drift, a linear fit is applied to the data of p_{Kedek} relative to p_{Vaisala}. The coefficient of determination R^2 for both time intervals is around 1 % meaning the variance of the data and the residuals of the fit are nearly equal. This means that the fitted data behaves nearly equal to a constant. Further, the mean values μ are nearly equal for both October and summer data. The drift of p_{Kedek} and therefore of p_{ref} can therefore be neglected.

3.4.2. Height Correction for all Measurement Locations

As discussed before, the pressure recorded at KEΔEK will be scaled to the Vaisala instrument, due to its absolute calibration and most exact known reference height. This pressure is called p_{ref}. To receive the ground pressure of every measurement height, scaling factors

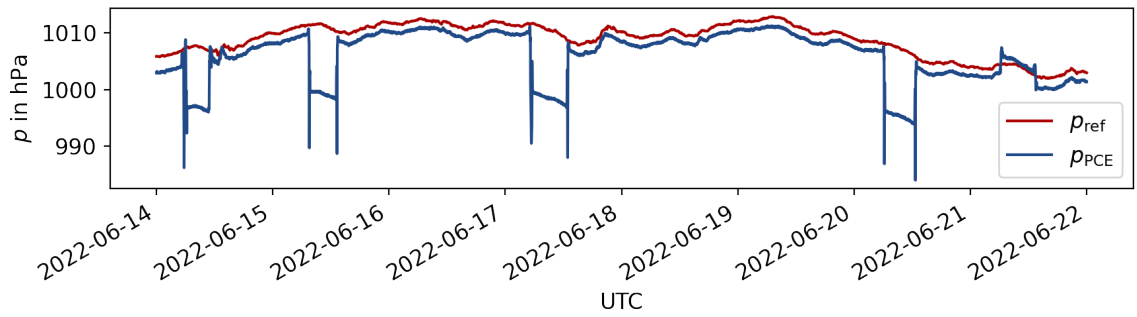

Figure 3.6.: Ground pressure data with changes due to relocation. Pressure data from 14 - 22 June 2022: reference pressure is KEΔEK data calibrated to Vaisala level p_{ref}. The abrupt changes in the pressure level recorded by the data logger are visible. At night, the data logger is stored at the Meteorology building at AUTh (Compare with Appendix A.1.5).

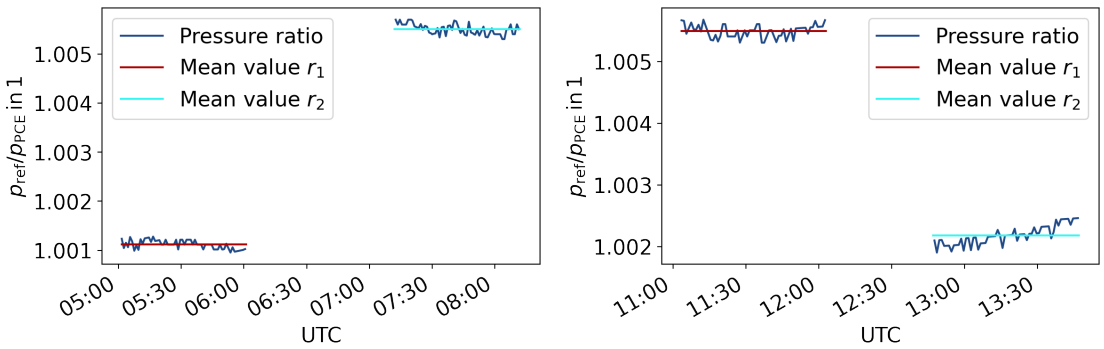

(a) (b)

Figure 3.7.: Ground pressure ratio for going from Meteorology building to Thermi (a) in the morning and back in the afternoon (b). The time intervals (6 to 7.15 am and 12 to 12.45 pm) when the data logger is moved is cut out from the graphs (data from 2022-07-11).

to correct the height difference between the reference pressure and the site are calculated in the following. Behind this idea lies the assumption of ground pressure not changing laterally in the range of measurement sites in the present campaign.

The procedure of calculating these pressure factors is described in the following. At every measurement day of the campaign, the data logger is transported together with the other measuring equipment from the storage location (for more detail, see Appendix Table A.3) to the measurement site and back afterwards. As every measurement site is located at a different height, the ground pressure shows characteristic steps for each location change (see Figure 3.6). To calculate factors for the ground pressure at different sites, ratios of the mean pressure the hour before and after moving the data logger are used (see Figure 3.7). Since most of the routes (from site 1 to site 2 or vice versa) are covered more then once, taking the mean value for two moves is reasonable. Those sites

Table 3.5.: Pressure factors and approximate heights of the measurement sites.

Site 1	Site 2	$\overline{f}_{1\to2}$	Altitude Site 2 in m[a]
Physics	Galini	0.99272	132.5
Physics	Efkarpía	0.99112	138.8
Physics	Seych Sou	0.98930	157.1
Physics	Diavatá	1.00461	17.2
Physics	Thermi	0.99777	84.2
Physics	Meteorology Upstairs	1.00123	53.0
Physics	Meteorology Downstairs*	1.00160	53 - 4 = 49[b]
Physics	Physics*	1	62.9

* Only one location change of the data logger used for the calculation of this pressure factor.
[a] GPS based altitude (see Table 3.1).
[b] No GPS data available: 4 m corresponding to estimated difference between Meteorology Up- and Downstairs.

with only one move used for the calculation are marked in Table 3.5. For the exemplary data in Figure 3.7, it writes (site 1: Meteorology building, site 2: Thermi):

$$f^{\text{outwardway}} = \left.\frac{r_1}{r_2}\right|^{\text{outwardway}} = \left.\frac{p_{\text{site2}}}{p_{\text{site1}}}\right|^{\text{outwardway}}, \tag{3.2}$$

$$f^{\text{returnway}} = \left.\frac{r_1}{r_2}\right|^{\text{returnway}} = \left.\frac{p_{\text{site1}}}{p_{\text{site2}}}\right|^{\text{returnway}}, \tag{3.3}$$

$$\Rightarrow \overline{f}_{1\to2} = \frac{1}{2}\cdot\left(f^{\text{outwardway}} + \frac{1}{f^{\text{returnway}}}\right) \hat{=} \frac{p_{\text{site2}}}{p_{\text{site1}}}. \tag{3.4}$$

$\overline{f}_{1\to2}$ now is the factor connecting pressure levels of site 1 and site 2:

$$p_{\text{site2}} = \overline{f}_{1\to2}\cdot p_{\text{site1}}. \tag{3.5}$$

Finally, the calculated pressure offsets between p_{ref} and each of the measurement sites are given in Table 3.5.

Plausibility Check for the Pressure Factors

A simple method to see if the idea of using pressure factors is reasonable is comparing them with altitude levels of the measurement sites. In Table 3.5, the GPS based altitude for each measurement site (as in Table 3.1) is given. To transfer these heights into ground pressure levels, the barometric formula is used. As derived in the Appendix A.1.1 with temperature assumed as constant, the simplified form of the this formula reads $p(z) = p_0\,\mathrm{e}^{-z/H}$ with the scale height $H = \frac{k_\mathrm{B}T}{mg}$. To calculate the scale height, a temperature T must be chosen. Following [SP16], the mean temperature of the troposphere is a reasonable

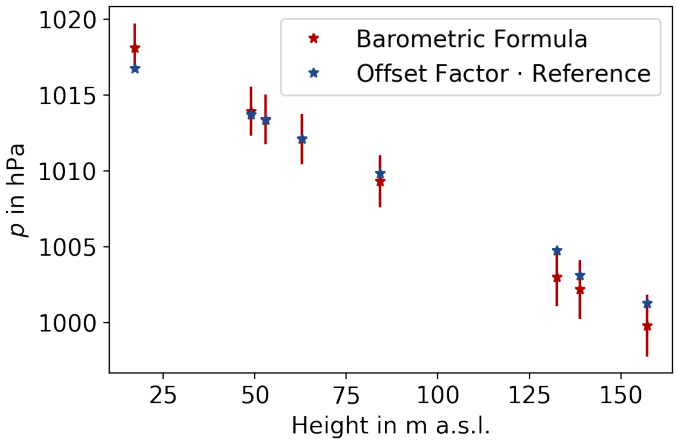

Figure 3.8.: Plausibility check of pressure factors. At the height of 61 m, the reference pressure level on the Physics Department's roof can be seen. The errors are calculated via uncertainty propagation and $\Delta H = 500\,\text{m}$ and $\Delta z = 12\,\text{m}$ and lie within 2.045 hPa. The maximal deviation between model pressure and pressure from pressure factors is 1.743 hPa for Galini.

choice, estimated for the semi-arid climate in Thessaloniki to be $T = 288\,\text{K}$. This yields a scale height of $H = 7.7\,\text{km}$. Further, as an exemplary reference pressure at the height of the Physics roof, the mean value of the Vaisala measurements in May 2022 is taken, which is $p = 1012.118\,\text{hPa}$.

Figure 3.8 shows the comparison of pressure levels from pressure factors and those from the barometric formula using GPS based heights. As expected for given small differences in height, the behaviour is linear in good approximation. Further, the pressure levels from the barometric formula lie within a range of about $\Delta p \approx 1.7\,\text{hPa}$ or $0.17\,\%$ to the offset values. For the following analysis, this method therefore seems to be a reasonable way to obtain different ground pressure levels.

3.5. Available Wind Data Sets

For the interpretation of the measured trace gas concentrations, wind plays a key role. The box model for up- and downwind conditions (section 2.2) contains the wind speed as well as the wind direction as important parameters. Therefore, having reliable sources for wind data is mandatory.

An overview on wind data used in the following analysis is given in Table 3.6. The primarily used data sets are those taken by station in Thermi and near the Meteorology building on the AUTh Campus. The meteorological station at AUTh is located between trees and building near the city center. Comparison with wind data recorded in Thermi (ΚΕΔΕΚ) and at the airport supports the assumption of lower wind speeds measured at the Campus while directions are consistent.

Figure 3.9 shows a map with the locations of the wind measuring stations. The coast line is emphasized to understand the relative position of the stations to the sea. A dominant

Table 3.6.: Overview of available wind data sets.

Instrument	Location	Elevation	Rel. Accuracy	Interval
Davis Instr. Vantage Pro 2	Thermi (ΚΕΔΕΚ)	$\approx 13\,\mathrm{m}^{a}$	$\pm 5\,\%^{x}$	10 min
Unknown	Meteorology[1]	$\approx 2\,\mathrm{m}^{b}$	$\pm 5\,\%^{y}$	10 min
Unknown	Makedonia Airport[2]	$8\,\mathrm{m}^{c}$	not known	60 min

[1] `https://meteo3.geo.auth.gr/stations/clim_data.htm`, July 2022
[2] `https://meteostat.net/de/place/gr/thessaloniki`, July 2022
[a] On the roof of a three-storey building.
[b] Ground-based measurement station.
[c] `https://meteostat.net/de/place/gr/thessaloniki`, July 2022
[x] [Dav]
[y] Information provided by Prof. P. Zanis, Department of Meteorology and Climatology, AUTh.

Figure 3.9.: Map with marked wind sensors on the Campus, in Thermi (ΚΕΔΕΚ) and at the airport. Wind speed as well as wind direction are important parameters for the up- and downwind setup. The map is a cut version of Figure 3.1 and depicts the wind sensors as stars. In an adapted form, small maps will be used throughout this work to illustrate measurement alignments and corresponding wind conditions.

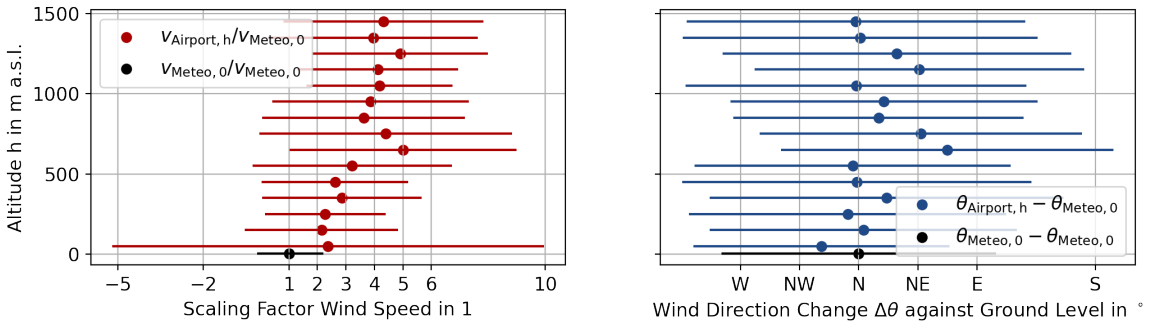

Figure 3.10.: Wind speed and direction profile as function of altitude. Relative to ground wind speed measured at the Meteorology station at AUTh. Change in wind direction relative to the north. Sounding data for wind profiles from `http://weather.uwyo.edu/upperair/sounding.html`, in December 2022. The data is taken and averaged for the period of the measurement campaign in Thessaloniki (04. - 22. October 2021 and 09. May 2022 - 12. July 2022).

wind direction in and around Thessaloniki is light sea breeze that comes from different directions for different measuring stations: from southwest at the Campus in the city center, more from SWW in Thermi and NWW at the Airport. In the analysis in chapter 4, wind data from all available stations will be compared to get an overall idea of the prevailing situation.

Of particular interest for the box model is the average wind speed and direction in the PBL, extending from the ground to approximately 1000 m. A method to extrapolate wind conditions and especially scaling wind speed above ground level is shown in [BHM20]. In this work, wind profiles are retrieved from data provided by the Department of Atmospheric Science at the University of Wyoming[6]. This source also provides a data set collected by a radiosonde located at the Makedonia Airport near Thessaloniki (compare to Figure 3.1). The source provides sound profiles at UTC 00:00 (local time Thessaloniki 03:00) and UTC 06:00 (local time Thessaloniki 09:00). The range in altitude expands from ground level (4 m at the airport) to an estimated maximum height of the PBL of 1500 m [San+98]. As discussed above, for the calculations of area emission fluxes, wind speed and direction will be taken from the Meteorology station at AUTh. Average ground wind speed at the airport is higher than at the Meteorology station, most probable due to surrounding buildings and trees in the city center. Therefore, estimating wind speed at altitude at the location of the Meteorology station requires levelling of the ground wind speeds ($v_{\text{Meteo,0}}$ to $v_{\text{Airport,0}}$) together with the scaling corresponding to the wind profile. Figure 3.10 shows the visualized wind profiles. For ground level, the ground wind speed at the Meteorology station is taken as reference as it should be a realistic value for the urban area. To obtain an overall scaling factor for further calculations, the wind profiles from the time period of both parts of the Thessaloniki campaign (04. - 22. October 2021 and 09. May 2022 - 12. July 2022) have been averaged. The given errors are standard deviations corresponding to the mean value for every 100 m step of altitude. The overall mean scaling

[6] `http://weather.uwyo.edu/upperair/sounding.html`, December 2022.

Figure 3.11.: Usage of a kite for the estimation of the wind direction (Photo taken at the measurement site in the Seych Sou park in July 2022 with a private digital camera and self-timer).

factor for wind speed and $h_{\mathrm{PBL}} = 1500$ m yields $k_{\mathrm{Wind}} = 3.428 \pm 1.123$ and can be applied in further analysis. Assuming the PBL to be only 1000 m, the obtained mean value changes to 3.324 ± 0.960. This possible deviation can be included later in the error consideration on the derived area emission fluxes. The change of wind direction in Figure 3.10 can serve as a basis for further analysis and will not be included in a quantitative way is this work.

Additionally, observations with a small kite serve to get a rough idea of the prevailing wind situation at the measurement site of the "satellite" instrument SN96 (Figure 3.11), as this location is not directly covered by wind data in most cases (compare Table 3.1 and Table 3.6).

3.6. Calibration of the Instruments

To make statements about GHG emissions, differences in column-averaged DMFs are considered. As mentioned in section 3.3, the expected range of such differences lie below the percentage level. After transportation of the device, small changes in the high precision hardware might lead to changes in performance. Thus, to perform reliable measurements of required quality, a calibration of the measurement devices is required. Calibration is performed using side-by-side measurements of atmospheric spectra to determine calibration factors that compensate for residual instrument specific deviations.

In preparation for the campaign, a side-by-side measurement of the campaign spectrometer SN96 next to the reference COCCON spectrometer SN37 was performed at KIT Karlsruhe in order to obtain the absolute calibration for both instruments. In Thessaloniki, 8 days of side-by-side measurements were performed to obtain a relative calibration between the campaign instruments SN96 and SN52. The main goal of those calibrations are correction factors for the column-averaged DMFs XCO_2, XCH_4 and XCO, reading

$X_{\text{gas}} = K_{\text{gas}}^{\text{SNXX}} X_{\text{gas}}^{\text{uncorr}}$. Further, the stability of the spectrometers throughout the campaign can be monitored through repeated side-by-side measurements.

3.6.1. Data Preparation for the Calibration

To ensure reliable data for the calibration, the following preparations are performed for each calibration measurement.

The coordinates used in `PROFFAST` are GPS based as shown in Table 3.1 and a-priori gas profiles are adopted from the TCCON GGG2020 processing (the so-called map files generated for the TCCON analysis are also used for the COCCON retrievals).

- For all calibration measurements, the first half hour after staring up the spectrometer is not taken into account to allow the laser to reach thermal equilibrium.
- The data sets from the different instruments are resampled into 5 minute averages to be able to compare them.
- Time intervals containing measurement problems are cut out (see Appendix A.1.3 and A.1.4).
- Measurement instabilities can occur due to a large solar zenith angle (SZA) [Gis+11; Tu19]. For SZA $> 70\,^{\circ}$, air mass between sun and spectrometer increases relatively fast with changing SZA. Namely, a relative air mass change of around 0.05 % has been obtained for $\Delta\text{SZA} = 1\,^{\circ}$ [Gis+11]. Therefore, small errors in the timestamps of the spectra recorded by the corresponding computer might lead to deviations in X_{AIR}. Thus, only results with SZA $< 70\,^{\circ}$ are considered for the calibration factors.
- Through different duration of measuring on each day and cutting time intervals due to measurement issues, each calibration day contributes a different amount of data. In order to weight the data points equally, the trimmed data sets for all days are merged and one calibration factor is calculated from there.

3.6.2. Pre-Campaign Calibration to Reference Instrument

As mentioned above, the first step in the calibration procedure are side-by-side measurements with the SN96 (campaign device) and the SN37 (reference device) in Karlsruhe. Those measurements have been performed between 2021-09-01 and 2021-09-03 before shipping the SN96 device to Thessaloniki for the first part of the campaign in October 2022. Pressure data was recorded by a PCE-THB40 Data Logger which is sufficient in this case as the absolute ground pressure is not of such importance for relative calibrations.

Column-averaged DMFs for CO_2, CH_4, CO and dry air from the pre-campaign calibrations are shown in the Appendix in Figure A.1. Following the process described above in subsection 3.6.1, the mean values for all those factors and the corresponding standard deviation given in Table 3.7 are obtained.

Table 3.7.: Calibration factors and corresponding standard deviations for SN96 relative to reference device SN37

	$K_{\text{gas}}^{\text{SN96}}$	$\sigma_{K_{\text{gas}}^{\text{SN96}}}$
XCO_2	1.00012531	0.00024586
XCH_4	1.00033906	0.00029437
XCO	1.01051686	0.00594044

Table 3.8.: Calibration factors for SN52 relative to the calibrated device SN96. The error contains the standard deviation corresponding to the mean value and the error propagation from $\sigma_{K_{\text{gas}}^{\text{SN96}}}$.

	$K_{\text{gas}}^{\text{SN52}}$	$\sigma_{K_{\text{gas}}^{\text{SN52}}}$
XCO_2	1.00112924	0.00048741
XCH_4	1.00079057	0.00063029
XCO	1.00858855	0.01280746

3.6.3. Relative Calibration of the Campaign Instruments

Similar to the procedure described in subsection 3.6.2, the calibration of SN52 relative to SN96 on site in Thessaloniki will be carried out. Due to the duration of the campaign from mid-May to mid-July and the daily transport of the EM27/SUNs, it makes sense to perform parallel measurements not only before the start of the actual campaign, but also between the up- and downwind or background measurements. This is a way to figure out instabilities of the devices or unnoticed changes in the measurement setup. The location of the side-by-side measurements changed due to practical reasons like demonstrations at the university or the storage location of the devices. For information about the measurement site for each day, see Appendix A.1.4.

Column-averaged DMFs for CO_2, CH_4, CO and dry air from the campaign calibrations are shown in the Appendix in Figure A.2. Again, the procedure as described in subsection 3.6.1 yields the mean values for all those factors and the corresponding standard deviation given in Table 3.8.

The comparison of calibration factors for the individual measuring days is shown in Figure 3.12. The attached error bars are standard deviations corresponding to the daily average added to the error propagation from the $K_{\text{gas}}^{\text{SN96}}$ factors (see Table 3.7):

$$\sigma_{K_{\text{gas}}^{\text{SN52}}}^{\text{total}} = \frac{X_{\text{gas}}^{\text{SN96}}}{X_{\text{gas}}^{\text{SN52}}} \cdot \sigma_{\text{gas}}^{\text{SN96}} + \sigma_{K_{\text{gas}}^{\text{SN52}}}^{\text{dailymean}}. \tag{3.6}$$

Most of the calibration factors lie in the σ range to the overall weighted mean value $\overline{K_{\text{gas}}^{\text{SN52}}}$. There is a correlation between XCO_2 and XCH_4, both tracers possibly show a similar time development. Connecting the calibration factors to the corresponding SZA would be interesting as the SZA has an annual course.

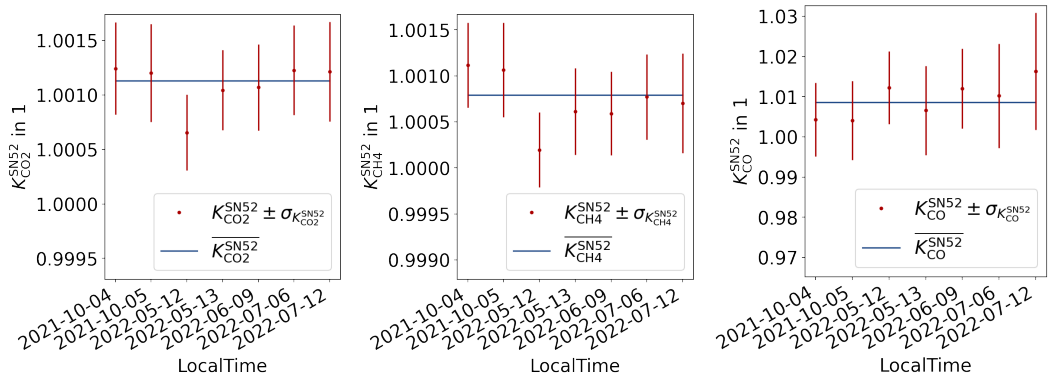

(a) XCO_2 (b) XCH_4 (c) XCO

Figure 3.12.: Calibration factors with corresponding error (red) for each day of side-by-side measurements. The weighted mean over all days lies within a σ range except for 2022-05-12 for XCO_2 and XCH_4.

On 2022-05-12 for XCO_2 and XCH_4, the daily mean is outside of this range. Besides the already discussed influences from large SZA or not correctly aligned `CamTracker`, there could be another systematic deviation on that particular day. It is noticeable that the difference in X_{AIR} between the instruments is relatively large, which might be an explanation (compare to the full plot of the DMFs in the Appendix A.2). For the further calculations, $\overline{K_{\mathrm{gas}}^{\mathrm{SN52}}}$ is used, while keeping in mind this outlier. Overall, the calibration factors lie in the sub per mille range which makes it reasonable to average all calibration days to one calibration factor for each gas.

From this point, everything is set for the retrieval of the up- and downwind and background measurements with the calibrated EM27/SUNs SN96 and SN52 and pressure levels for each measurement site.

4. Measurement Campaign Thessaloniki: Results and Application of the Box Model

After introducing the measurement procedure, the retrieval method and used data as well as describing the calibration in the previous chapters, the measurement results will be presented and analyzed in the following. After explaining the preparation of the data in subsection 4.0.1, the results of the background measurements are presented in section 4.1, followed by those of the up- and downwind measurements section 4.2. From the results of the up- and downwind configurations, emission fluxes are derived using the previously introduced box model. To assess possible emissions, correlations of GHGs concentrations are discussed in subsection 4.2.3. The results of the estimation of local emission fluxes under calm wind conditions is presented in section 4.3. Finally, the obtained results are discussed in section 4.4.

An overview of the DMFs for CO_2, CH_4, CO and dry air for all campaign days is given in Appendix A.3. It shall serve primarily to see how X_{AIR} behaves throughout the campaign in October 2021 and summer 2022 as a indication of measurement stability. There is no visible overall drift and the standard deviation lies at around 0.07 %.

4.0.1. Data Preparation for the Analysis

In the same manner as for the calibration, the following preparation of the data is performed to guarantee reliable results.

The coordinates used in `PROFFAST` are GPS based as shown in Table 3.1 and a-priori gas profiles are adopted from the TCCON GGG2020 processing (the so-called map files generated for the TCCON analysis are also used for the COCCON retrievals).

- For the analysis of the following measurements, the first 10 minutes are cut due to the warm up of the spectrometer's laser.
- If necessary, the data sets from the different instruments are resampled in 5 minute intervals to be able to compare them.
- Time intervals containing measurement problems are cut out (see Appendix A.1.3 and A.1.4).
- As explained in subsection 3.6.1, only results with SZA $< 70^\circ$ are considered for the calculation of further quantities.

Table 4.1.: Overview of background measurement days and corresponding distance L between the sites.

Site SN52 - Site SN96	Setup	Days	L in m
Physics-Physics	Side-by-Side	2021-10-04	≈ 1
		2021-10-05	
		2021-10-06	
Thermi-Thermi	Side-by-Side	2022-05-12	≈ 1
		2022-05-13	
Meteorology-Meteorology	Side-by-Side	2022-06-09	≈ 1
		2022-07-06	
		2022-07-12	
Physics - Meteorology	Small Distance	2022-07-01	330
		2022-07-02	
Physics - Thermi	Large Distance	2021-10-20	8000
		2021-10-22	
		2022-05-20	
		2022-06-24	
		2022-06-27	
		2022-06-29	

4.1. Estimation of Background Abundances

To begin with, the results of the background measurement days are analyzed. The background measurement setup is described in subsection 3.3.3. All measurement days including the chosen setup are listed in the measurement notes in Appendix A.1 and A.2. The basis for the classification of the setup during the campaign was the weather forecast and the available measurement sites. Nevertheless, the actual conditions often differed from the expectation and must be evaluated comparing wind data and measurement site for each day.

Table 4.1 lists the measurement days used to investigate the background variability $|\Delta X\text{gas}| = |X\text{gas}(\text{SN96}) - X\text{gas}(\text{SN52})|$. It is analyzed for the side-by-side measurements with a negligible distance between the instruments and then compared to a setup with a small and finally with a relatively large distance.

4.1.1. Background with Small Distance

As described insubsection 3.3.3, measuring lateral background variability on small scales is useful to estimate the background-induced uncertainties of the emission flux.

On 2022-07-01 and 2022-07-02, measurements on the Physics and the Meteorology building were performed. Those sites are separated by around 330 m, located in the city centre. Visualized DMFs of CO_2, CH_4, CO and dry air for those two days are attached in the Appendix A.4. The dominating wind direction can be categorized as a sea breeze.

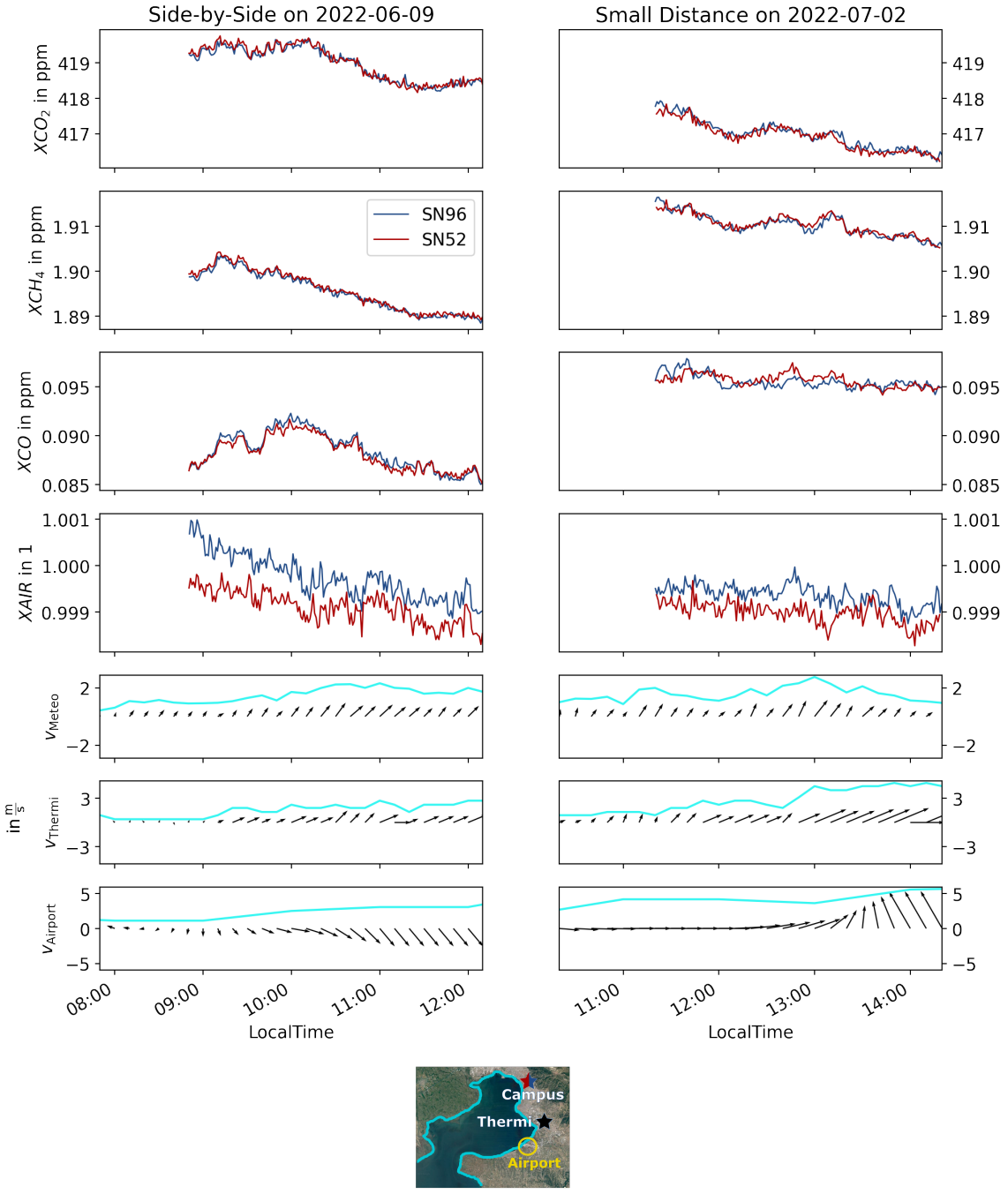

Figure 4.1.: DMFs and wind data to compare side-by-side and background measurements with small distance. The small map with marked wind measuring stations Thermi and Airport serves for orientation concerning wind direction, which is dominantly sea breeze for these days. The wind data is displayed one hour earlier because the effects of the wind are measured late.

Table 4.2.: Background variability for different distances between the instruments. The attached error is the averaged standard deviation among all single daily measurement samples. As the sample size varies for different measurement days, mean values and standard deviations are weighted with the daily measurement duration.

	$\lvert\Delta XCO_2\rvert$ in ppm	$\lvert\Delta XCH_4\rvert$ in ppm	$\lvert\Delta XCO\rvert$ in ppm
Side-by-Side	0.080016 ± 0.047829	0.000518 ± 0.000274	0.000492 ± 0.000282
Small Distance[a]	0.106744 ± 0.115462	0.000474 ± 0.000559	0.000546 ± 0.000669
Campus-Thermi[b]	0.322748 ± 0.253303	0.001896 ± 0.001369	0.002263 ± 0.001924

[a] Visualized daily results in Appendix A.5.

[b] Visualized daily results in Appendix A.6.

Compared to the wind sensors located at Meteo and Thermi, the wind direction measured at the Airport differs. This might be due to the location of the Airport relative to the sea (section 3.5). Some possible measurement instabilities can be seen from around 15:45 on 2022-07-01. As there is no obvious reason like high SZA for this behaviour, it will be reflected in the results as a statistical uncertainty.

Comparing the background variability for the setup with small lateral distance to side-by-side measurements (Figure 4.1), a similar behaviour is observed. This supports the argumentation that for small deviation of the up- and downwind alignment, the deviations in $\Delta X\text{gas}$ are negligible.

The calculated results for the lateral variability $|\Delta X\text{gas}|$ are presented in subsection 4.1.3 while the visualization is shown in Appendix A.5.

4.1.2. Background with Larger Distance

Additionally to the background measurements with a small distance between the instruments, investigating background variability on larger lateral scales can be used to estimate possible inaccuracies of further analysis like emission calculations. A number of days in the measurement configuration with the SN52 instrument at the Campus and SN96 at Thermi (distance $\approx 8\,\text{km}$) at sea breeze (S/SW) wind conditions have been performed. These days might give an idea of background variability coming from the sea. The lateral variability $|\Delta X\text{gas}| = |X\text{gas}\,(\text{SN96}) - X\text{gas}\,(\text{SN52})|$ for this alignment is shown in the Appendix A.6. The averaged numerical results of those measurements are presented in the following subsection 4.1.3.

4.1.3. Results for Background Setups

Table 4.2 presents the average variability obtained by weighting daily mean values with the measurement duration. This is to avoid measurement days with small sample sizes having a greater impact on the final average. The results show that the variability for a small distance between the measurement locations lies near the range of side-by-side measurements with an percentage $(\Delta X\text{gas}(\text{Background})/\Delta X\text{gas}(\text{Side}-\text{by}-\text{Side}) \cdot 100\,\%)$

Table 4.3.: Overview of up- and downwind measurement days and corresponding distance L between the sites. The prevailing wind direction is observed with a kite on ground level at the SN96 site outside the city center as demonstrated in Figure 3.11. This manually observed wind direction can differ from the measured one. It is measured in the morning hours and can change throughout the day.

Site SN52 - Site SN96	Configuration	Days	Wind Direction	L in m
Physics - Thermi	Upwind - Downwind	2021-10-13	N	8300
		2021-10-19	NW	
Meteo - Efkarpía	Upwind - Downwind	2022-06-15	NW	6600
		2022-06-17	SW	
		2022-06-20	S/SW	
Meteo - Seych Sou	Upwind - Downwind	2022-07-04	−*	940
		2022-07-05	−*	
Meteo - Diavata	Downwind - Upwind	2022-07-07	NW/NNW	10800
Meteo - Thermi	Upwind - Downwind	2022-07-11	N/NNW	8000

*wind speed too low to see a direction with the used kite.

of 133 % for CO_2, 91.5 % for CH_4 and 111 % of CO. Further, the standard deviations of the background measurement are around twice as high as for the side-by-side measurement. Having only two days of measurement for the background setup with a small distance, statistical deviations (e.g. on 2022/07/01) weight heavier then within the 8 calibration days.

A clear enhancement of the variability relative to the side-by-side measurements is visible for the setup with a larger distance between the instruments. Comparing it to the inverse calculated values for ΔXgas from EDGAR emissions (Table 3.3), the background variability reaches a percentage of minimum 135 % for CO_2 and 50.3 % for CH_4. As the EDGAR based concentration gradients reflect effective GHG emissions, it can no longer be assumed that only background concentrations are measured for the background setup with a large distance.

4.2. Up- and Downwind Measurements

The estimation of area emission fluxes from up- and downwind measurements can be considered as the main interest in this work. It can be compared e.g. to other emission hotspots. The measurement days with the two instruments set in up- and downwind configuration are listed in Table 4.3 The table does not contain all days noted as "Up-Down" in the Appendix A.1.3 and A.1.4. This is because the latter have been listed during the campaign based on weather forecast, from which the real conditions deviate. In contrast, the days in Table 4.3 are selected by comparing the instrument's alignment to the measured wind data of the available wind data sets (section 3.5). The map with the added sites and hotspots in Figure 3.1 serves to compare the prevailing wind speed with the location of the measurement sites.

Table 4.4.: Quantities used for the calculation of area emission fluxes with the box model.

Quantity	Value	Source
$TC^{\mathrm{SN52}}_{\mathrm{DryAir}}$	variable	Equation 2.6 + quantities below
$TC^{\mathrm{SN52}}_{\mathrm{H_2O}}$	variable	SN52 (Campus)
P_{gr}	p_{ref}·pressure factor	Vaisala/KEΔEK + Table 3.5
m_{DryAir}	$4.810 \cdot 10^{-26}$ kg	[GHK08]
$m_{\mathrm{H_2O}}$	$2.991 \cdot 10^{-26}$ kg	Periodic Table of Elements
M_{CO2}	$44.01 \frac{\mathrm{g}}{\mathrm{mol}}$	Periodic Table of Elements
M_{CH4}	$16.04 \frac{\mathrm{g}}{\mathrm{mol}}$	Periodic Table of Elements
M_{CO2}	$28.01 \frac{\mathrm{g}}{\mathrm{mol}}$	Periodic Table of Elements
$\langle g \rangle$	$9.805 \frac{\mathrm{m}}{\mathrm{s}^2}$	Averaged over PBL[1]
N_{A}	$6.02214076 \cdot 10^{23} \frac{1}{\mathrm{mol}}$	`Scipy Constants` [Vir+20]
Distance L	Table 4.3	*Google Maps* Range Finder (Dec 2022)
Wind speed v	variable · 3.428	Meteorology station · k_{Wind} (section 3.5)

4.2.1. Application of the Box Model

In the present work, a box model, introduced in subsection 2.2.2, is used to estimate area emission fluxes of CO_2, CH_4 and CO. The up- and downwind setup is described in subsection 3.3.1. Ideally, the wind trajectory connects both instruments in this configuration. In the Thessaloniki campaign, deviations of the ideal must be taken into account. Therefore, the obtained background variability from section 4.1 can be taken into account. A rough error estimation is performed in subsection 4.2.2.

The area emission flux is calculated according to the formula in Equation 2.24, which is repeated here for simplicity:

$$\begin{aligned} F_{\mathrm{UpDown}} &= \frac{TC^{\mathrm{SN52}}_{\mathrm{DryAir}} \cdot v_{\mathrm{wind}}}{L} \cdot k_{\mathrm{gas}} \cdot \left(X^{\mathrm{box}}_{\mathrm{gas}} - X^{\mathrm{b}}_{\mathrm{gas}} \right) \\ \text{with } k_{\mathrm{gas}} &= \frac{M_{\mathrm{gas}}}{N_{\mathrm{A}}} \cdot 31536 \cdot 10^{6}, \end{aligned} \tag{4.1}$$

while $X^{\mathrm{box}}_{\mathrm{gas}} - X^{\mathrm{b}}_{\mathrm{gas}} = \Delta X\mathrm{gas} = X^{\mathrm{downwind}}_{\mathrm{gas}} - X^{\mathrm{upwind}}_{\mathrm{gas}}$ corresponds to the difference between the two EM27/SUN instruments. Depending on the wind situation, the role of the instruments can be different. As the Campus of AUTh is located in the center of the city and does not change on large scales (only from Physics to Meteorology site with a difference of 330 m), it shall be used as the location corresponding to the calculation of the defining quantities in Equation 4.1. Those are presented in Table 4.4. Wind data for the calculations is taken from the Meteorology station at AUTh due to its central position in the city and

[1] Formulas from `https://www.vcalc.com/wiki/gravity-acceleration-by-altitude` (December 2022) to calculate g_{Lat} at latitude 40.6 °N and then scale g_{Lat} to altitude levels of 800, 1200 and 1500 m (estimated possible heights of PBL) and take mean value. The standard deviation of the mean value for the different assumed PBL heights is 0.0004, why it is reasonable to take the mean value for the calculation of fluxes.

therefore relative to the possible measurement sites (compare to Figure 3.1). To evaluate the reliability, this data is in the following compared to that measured in Thermi (ΚΕΔΕΚ) and at the airport.

In the following, visualized data showing the temporal course of the area emission flux as well as DMFs of CO_2, CH_4 and CO for each different instrument configuration is presented and discussed. In the figures, all available wind data sets are used (see section 3.5). Plots of the individual days are shown in the Appendix A.2.4.

On 2022-07-07 (Figure 4.2), the wind direction observed by the different sensors is in agreement to be mostly from NNW and NW direction. The small map shows the configuration of the instruments in Diavatá (SN96) and on the Campus (SN52), while the latter is in downwind position. The locations of the wind sensors in Thermi and at the airport are displayed as well. It is visible that for all considered trace gases, CO_2, CH_4 and CO, the instrument placed at the Campus measures an increased concentration compared to that at Diavatá. This is also reflected in the displayed area emission flux. Especially the signals in CO_2 and CO could display the refinery (see the small map in Figure 4.2) located near Diavatá directly in line between the instruments. Further, a the northwestern and main part of Thessaloniki's urban area is located in between Diavatá and the Campus. In this area is the harbour, another possible source of CO_2 and CH_4 .

In Figure 4.3, the campaign days measuring in Efkarpía in the northern part of Thessaloniki are shown. The prevailing wind situation is comparable to that from the background measurement at sea breeze, with mainly southwest wind measured at the Campus and in Thermi while the wind comes from northwest at the airport. The assumption here is that the given sea breeze conditions allow to interpret the Efkarpía site as downwind and the Campus site as upwind position. For CO_2 and CO, a concentration enhancement for most time of the three days is observed while for CH_4, no clear net emission can be seen throughout the days. The measured emissions for CO_2 and CO could be caused by the harbour or the cement factory (small map in Figure 4.3) while the latter would mean a local accumulation of trace gases at the Efkarpía site.

Another set of measured data with promising wind conditions is shown in Figure 4.4. It displays the data of three days of measurements at the Campus and at the Thermi site. Plots for the single days can be found in the Appendix A.2.4. The overall wind situation is similar to that for the Diavatá day analyzed before which is in northern and northwestern direction. This fits to the instrument's configuration at the Campus (SN52) and in Thermi (SN96). Here, the SN96 is in downwind position. Compared to the alignment Diavatá-Campus on 2022-07-07 described before, the setup Campus-Thermi covers the southeastern part of the city. The wind speed on 2022-07-11 is relatively constant, indicating stable conditions. The emission flux for CO_2 is in a similar range as on 2022-07-07, again reaching the highest level in the early evening. CH_4 and CO though scale at around half the maximum values compared to the Diavatá measurement day. This again could indirectly hint the refinery and the harbour as these sources are not located within the Campus-Thermi alignment. Another explanation could be an accumulation of local emission in the city center measured at the Campus site. The NNW/NW wind conditions on 2021-10-13 are similar to those on 2022-07-11 and so are the emission graphs. The CO_2 emissions show a similar behaviour for both days as there are "negative emissions" until 11:00 and after that a mostly positive emission flux. Negative values for F do probably not hint a sink

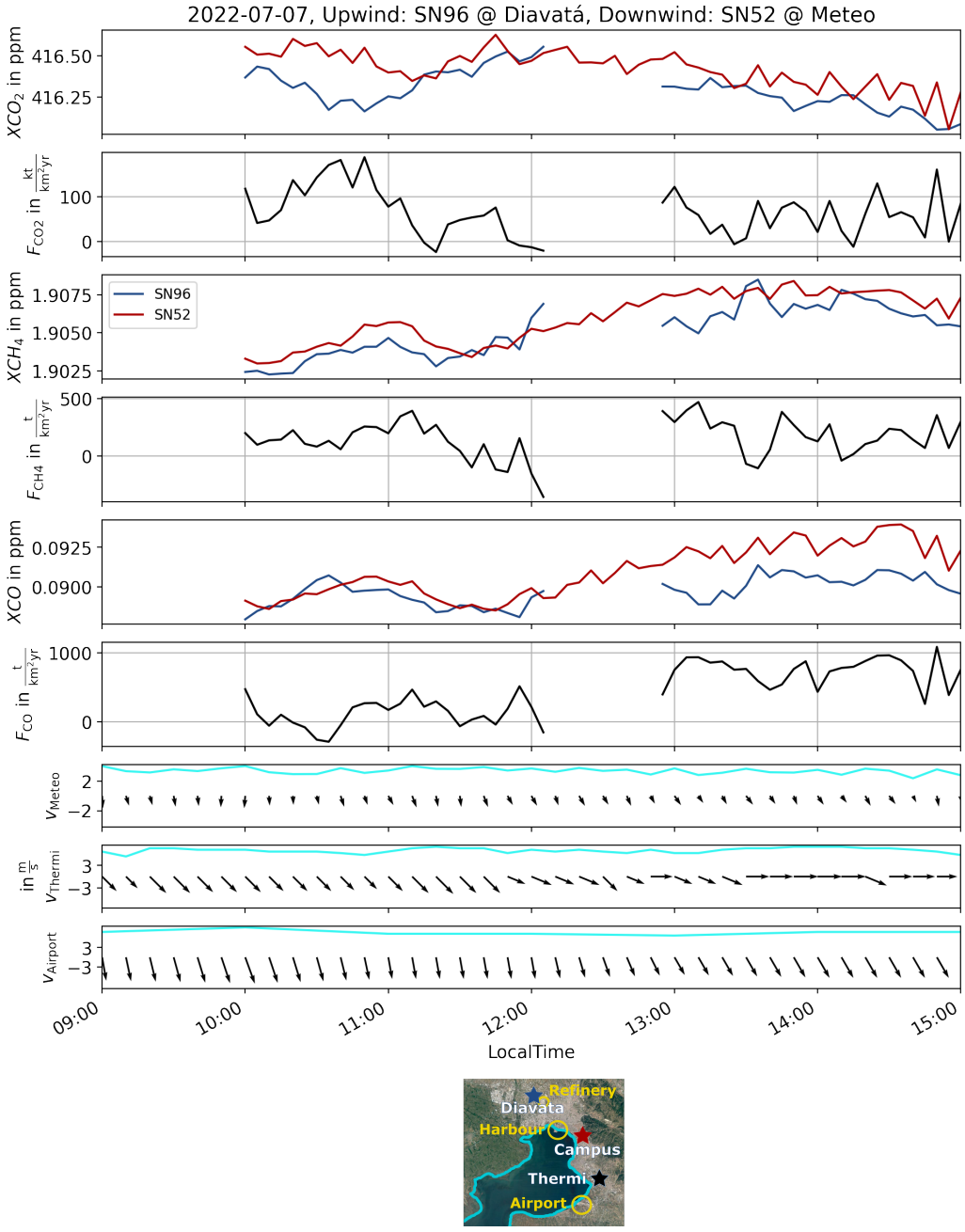

Figure 4.2.: DMFs, area flux and wind data for up- and downwind measurements in Diavatá and on Campus on 2022-07-07. The emission flux is calculated with a scaling factor of 3.428 as discussed in section 3.5. The wind data is displayed one hour earlier because the effects of the wind are measured late. The small map serves for orientation concerning wind direction.

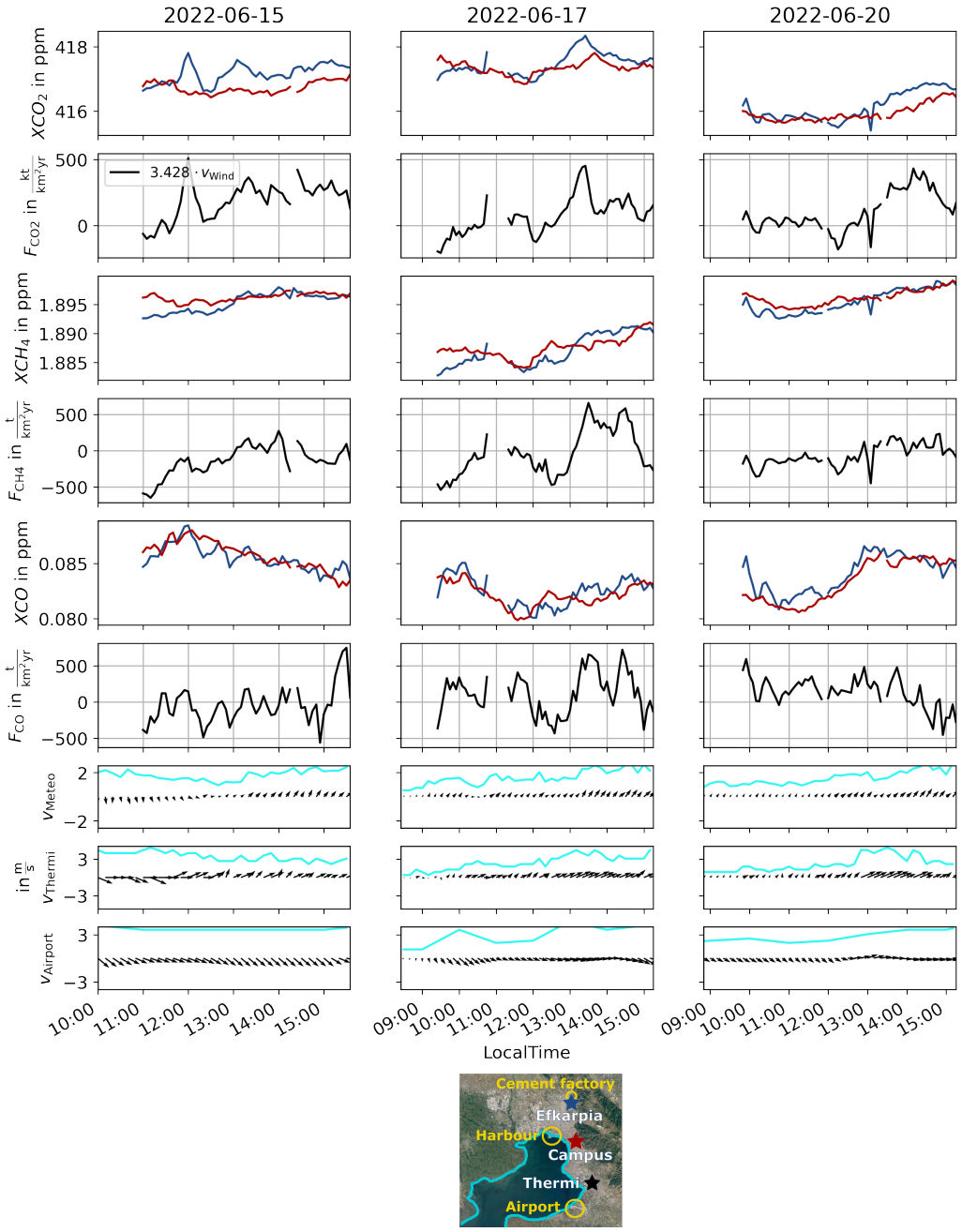

Figure 4.3.: DMFs, area flux and wind data for up- and downwind measurements in Efkarpía and on Campus on 2022-06-15, 2022-06-17 and 2022-06-20. The emission flux is calculated with a scaling factor of 3.428 as discussed in section 3.5. The wind data is displayed one hour earlier because the effects of the wind are measured late. The small map serves for orientation concerning wind direction.

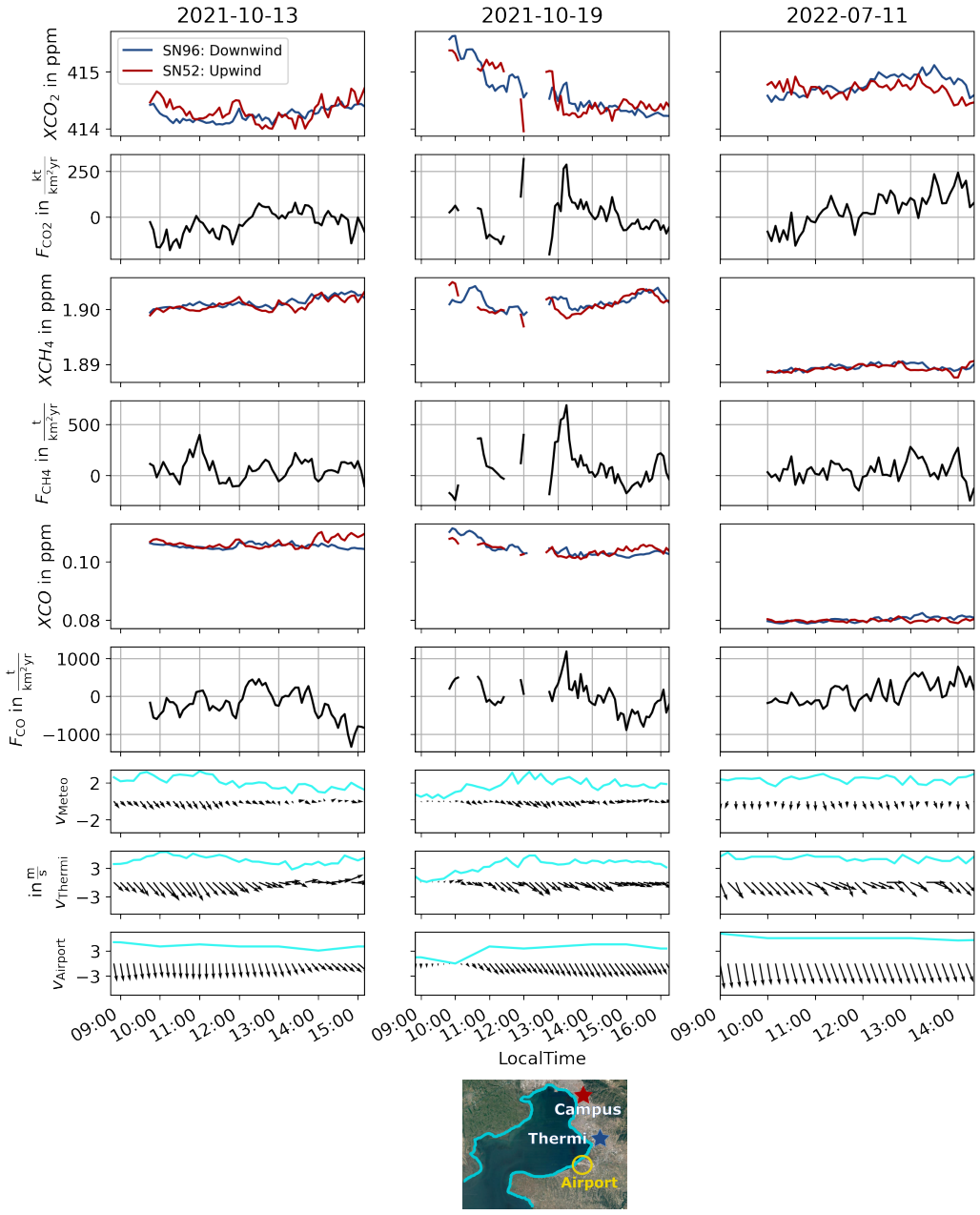

Figure 4.4.: DMFs, area flux and wind data for up- and downwind measurements in Thermi and on Campus on 2021-10-13 and 2012/10/19 and 2022-07-11. The emission flux is calculated with a scaling factor of 3.428 as discussed in section 3.5. The wind data is displayed one hour earlier because the effects of the wind are measured late. The small map serves for orientation concerning wind direction.

at this point but are caused by the structure of the box model and different reasons for a variability in XCO_2 (as e.g. shown by the background measurements in section 4.1). The scale of the positive emission flux for CO_2 and CH_4 is comparable to that in for Diavatá in Figure 4.2.

Figure 4.5 shows the measured data for the up- and downwind setup on 2022-07-04 and 2022-07-05 in Seych Sou (SN96) and on Campus (SN52). Again, plots for the single days can be found in the Appendix A.2.4. Seych Sou is a park limiting the city to the northeastern side. The difference in altitude for this setup is the largest of all setups while the distance between the sites is the smallest. For this configuration, there is mostly urban area, one main road and some hundred meters of trees in between the measurement sites. Wind conditions on these days can be classified as sea breeze considering all three wind data sets (compare to map in Figure 4.4). The emission fluxes for all tracers show relatively large scales especially on 2022-07-04, while the largest emissions are negative, again most probable hinting a variability not well described by the box model. Further, correlating emissions in CH_4 and CO are visible on 2022-07-04 which could be caused by a local source near the Campus or at the harbour, or a wind field differing strongly from the measured on ground level. The significance of the measurements in Seych Sou seem to be limited in view of the large scales with negative emission values and the relatively complicated topographical situation. Due to that, the results of the Seych Sou measurement days are not included in the final results that will be presented in subsection 4.2.2.

4.2.2. Estimation of Errors and Results for Emission Flux

In the following, a simple estimate of the possible errors is provided. Due to the simplistic approach of the box model and limited availability of meteorological data, significant uncertainties are expected. Therefore, the errors of the underlying quantities (Table 4.5) shall be taken into account and an overall error based on those calculated. Hereby, many relatively small errors can be neglected in comparison to the large inaccuracies mainly coming from the assumed background variability on $\Delta X\text{gas}$. The error variables are assumed to be uncorrelated, which is only an approximation, as the ground pressure P_{gr} is used by `PROFFAST` to retrieve the DMFs. The errors then are calculated by the error propagation formula [Ku66] applied to Equation 2.24:

$$\sigma_F = \sqrt{\left(\frac{\partial F}{\partial L}\cdot\sigma_L\right)^2 + \left(\frac{\partial F}{\partial v}\cdot\sigma_v\right)^2 + \left(\frac{\partial F}{\partial P_{\text{gr}}}\cdot\sigma_{P_{\text{gr}}}\right)^2 + \left(\frac{\partial F}{\partial\left(\Delta X\text{gas}\right)}\cdot\sigma_{\Delta X\text{gas}}\right)^2}. \tag{4.2}$$

The overall results, excluding those for Seych Sou, are shown in Figure 4.6 and numerically presented in Table 4.6. Error propagation results in uncertainties of the same order of magnitude as the targets themselves. This might be mainly due to changing wind situation, insufficient wind information at altitude, difficult topographical situations (especially Seych Sou) and limits in the box model itself. Nevertheless, the present choice of up- and downwind measurement days can give a rough idea of the order of magnitude of trace gas emissions in Thessaloniki.

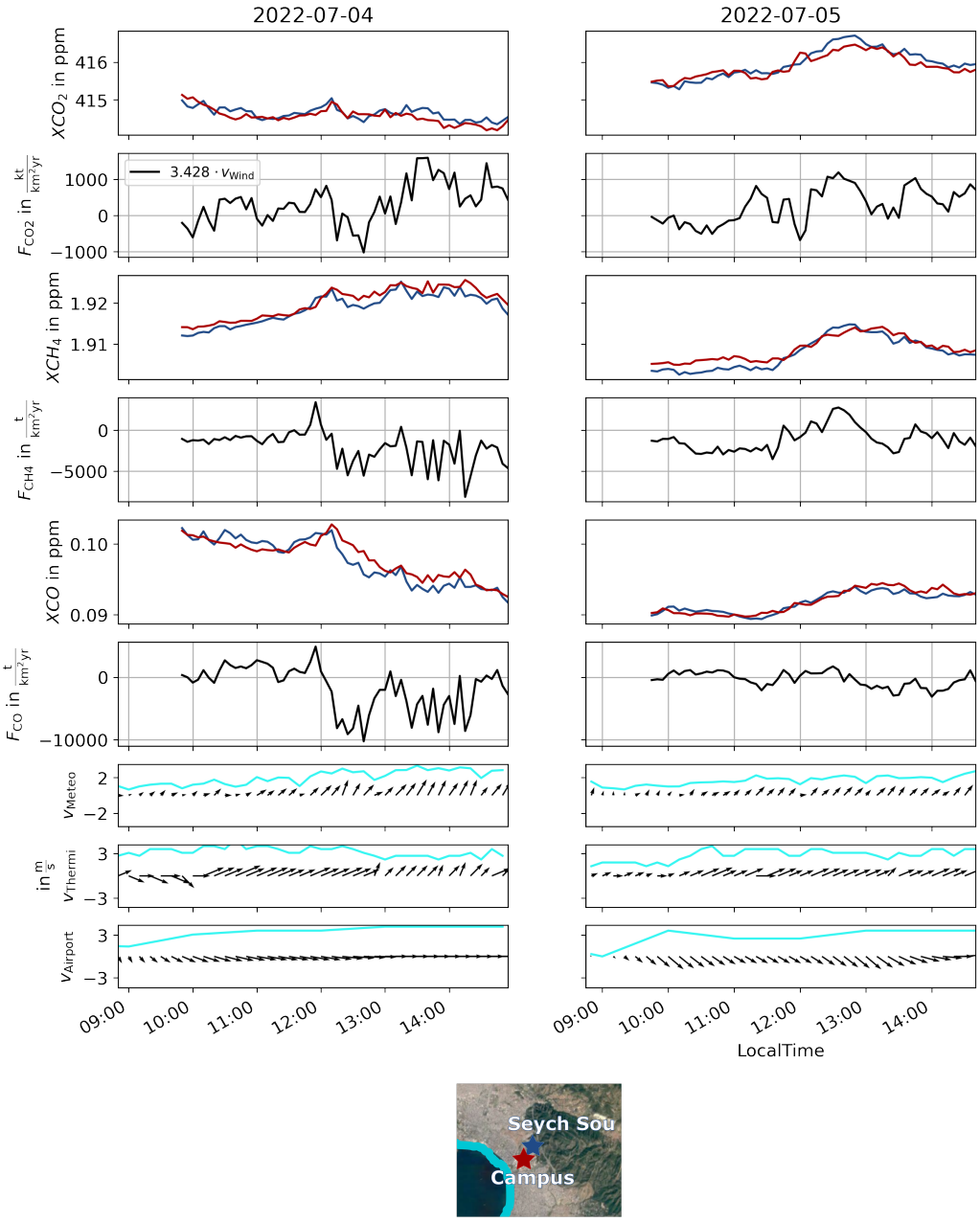

Figure 4.5.: DMFs, area flux and wind data for up- and downwind measurements in Seych Sou and on Campus on 2022-07-04 and 2022-07-05. The emission flux is calculated with a scaling factor of 3.428 as discussed in section 3.5. The wind data is displayed one hour earlier because the effects of the wind are measured late. The small map serves for orientation concerning wind direction.

Table 4.5.: Inaccuracies on the quantities used for the calculation of area emission fluxes with the box model

Quantity	Error	Source of original value
$\sigma_{TC^{SN52}_{DryAir}}$	negligible	Equation 2.6 + quantities below
$\sigma_{TC^{SN52}_{H_2O}}$	negligible	SN52 (Campus)
$\sigma_{P_{gr}}$	2 hPa	Vaisala/KEΔEK + Table 3.5
$\sigma_{m_{DryAir}}$	negligible	[GHK08]
$\sigma_{m_{H_2O}}$	negligible	Periodic Table of Elements
$\sigma_{M_{CO2}}$	negligible	Periodic Table of Elements
$\sigma_{M_{CH4}}$	negligible	Periodic Table of Elements
$\sigma_{M_{CO2}}$	negligible	Periodic Table of Elements
$\sigma_{\langle g \rangle}$	negligible	Table 4.4
σ_{N_A}	negligible	`Scipy Constants` [Vir+20]
σ_L	±50 m	*Google Maps Range Finder* (Dec 2022)
σ_v	$\pm 0.5 \frac{m}{s}$	5 % of 6 $\frac{m}{s}$ + ≈ 0.2 $\frac{m}{s}$ from k_{Wind} (section 3.5)
$\sigma_{\Delta XCO_2}$	0.106744 ppm	Small distance background variability (Table 4.2)
$\sigma_{\Delta XCH_4}$	0.000474 ppm	"
$\sigma_{\Delta XCO}$	0.000546 ppm	"

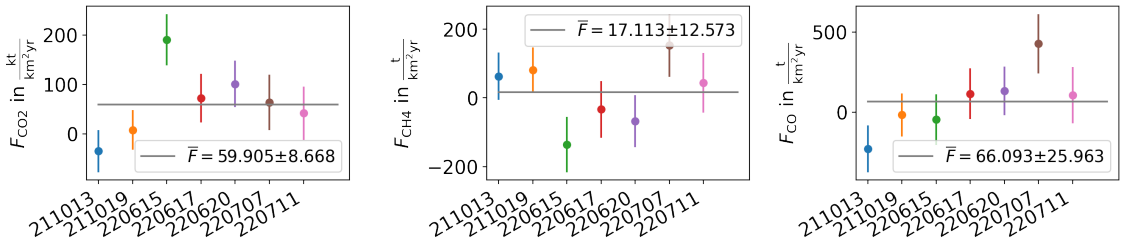

Figure 4.6.: Results for area emission fluxes for the up- and downwind measurements. The given mean value $\overline{F}$ for each trace gas is weighted by the measuring time of each day, as well as the attached standard deviation. The daily data fluxes are mean values with an attached error bars obtained via error propagation. Further, the results are for the scaled wind speed $v = v_{Meteo} \cdot k_{Wind}$ (section 3.5).

Table 4.6.: Final numerical results for area emission flux obtained via up- and downwind setup with attached errors. The standard deviations are corresponding to the mean values of the daily results as shown in Figure 4.6.

	Mean Value	Error Propagation	Standard Deviation
F_{CO2} in $\frac{kt}{km^2yr}$	59.905	48.153	8.668
F_{CH4} in $\frac{t}{km^2yr}$	17.113	78.133	12.573
F_{CO} in $\frac{t}{km^2yr}$	66.093	156.072	25.963

4.2.3. Trace Gas Correlations

To identify possible sources or sinks of GHGs, investigating correlations between them can be useful. In the following, two different correlations are considered: that between ΔXCO and ΔXCO_2 which is valuable to seek for hotspots where biomass incineration take place. A second interesting quantity is the correlation between ΔXCH_4 and ΔXCO_2. This correlation helps to recognize the existence of source areas contributing both CO2 and CH4 emissions. Low correlation would support the hypothesis that areas emitting CO2 and CH4, respectively, are not congruent. To calculate correlations for a up- and downwind setup, it is reasonable to subtract the DMF measured by the upwind instrument from that by the downwind instrument. The used correlation coefficients are Pearson correlation coefficient, obtained by the corresponding *pandas function* [McK10].

Figure 4.7 shows the summarized plot of both types of correlation for all up- and downwind measurement days. For a given instrument setup, each measurement day is marked by a different shade of the same color. The three measurement days with the setup Campus-Thermi yield positive correlation coefficients above 0.3 for both types of correlations with a significant correlation for $\Delta XCO_2/\Delta XCO$. Concerning source strength ($\Delta XCO_2/\Delta XCH_4$), the three days measuring at the Campus and in Efkarpía show a clear signal with a minimum correlation coefficient of 0.687. As many of the corresponding data points in Figure 4.7 lie in negative ΔXCH_4, the enhanced concentrations for CH_4 are measured by the upwind instrument which weakens the statement of a possible source. ΔXCO_2 and ΔXCO are only weakly correlated. No clear correlations are observed for the day in Diavatá. Noticeable is the contrast in the $\Delta XCO_2/\Delta XCH_4$ correlation coefficients between 2022-07-04 and 2022-07-05 for the downwind instrument in the Seych Sou park. While on 2022-07-04 the data is nearly randomly distributed, a strong linear slope is observed in 2022-07-05.

Another information that can be extracted of Figure 4.7 is the measured variability, shown by the scale of the axes, which can be compared to that of the inverse calculation from EDGAR numbers in subsection 3.3.2. Hereby, both measured trace gases lie within the range of the EDGAR values, ΔXCO_2 with a maximum EDGAR value of 0.240 ppm and ΔXCH_4 with 0.00378 ppm.

4.3. Estimation of Emission Flux for Calm Wind Conditions

Another model to get an estimate of area emission fluxes is assuming a locally uniform, but time dependent trace gas concentration and wind speed $v_{\text{Wind}} \to 0$ (see subsection 2.2.4). It can provide an estimation for local emissions around the city center. Therefore, the main interest is an application of this model to data collected by the instrument (SN52) located at the AUTh Campus in a central location in the city area.

Figure 4.8 shows the connection of the variability of trace gases ΔXgas between the instruments and the wind speed v_{Wind}. The wind data is taken from the Meteorology station which seems reasonable as the previous plots shown in this work hint a correlation of the wind speeds of the three wind data sources. ΔXgas is shown for all campaign days in October 2021 and summer 2022. In the present visualization, $\Delta X\text{gas}^{-1}$ is plotted in a

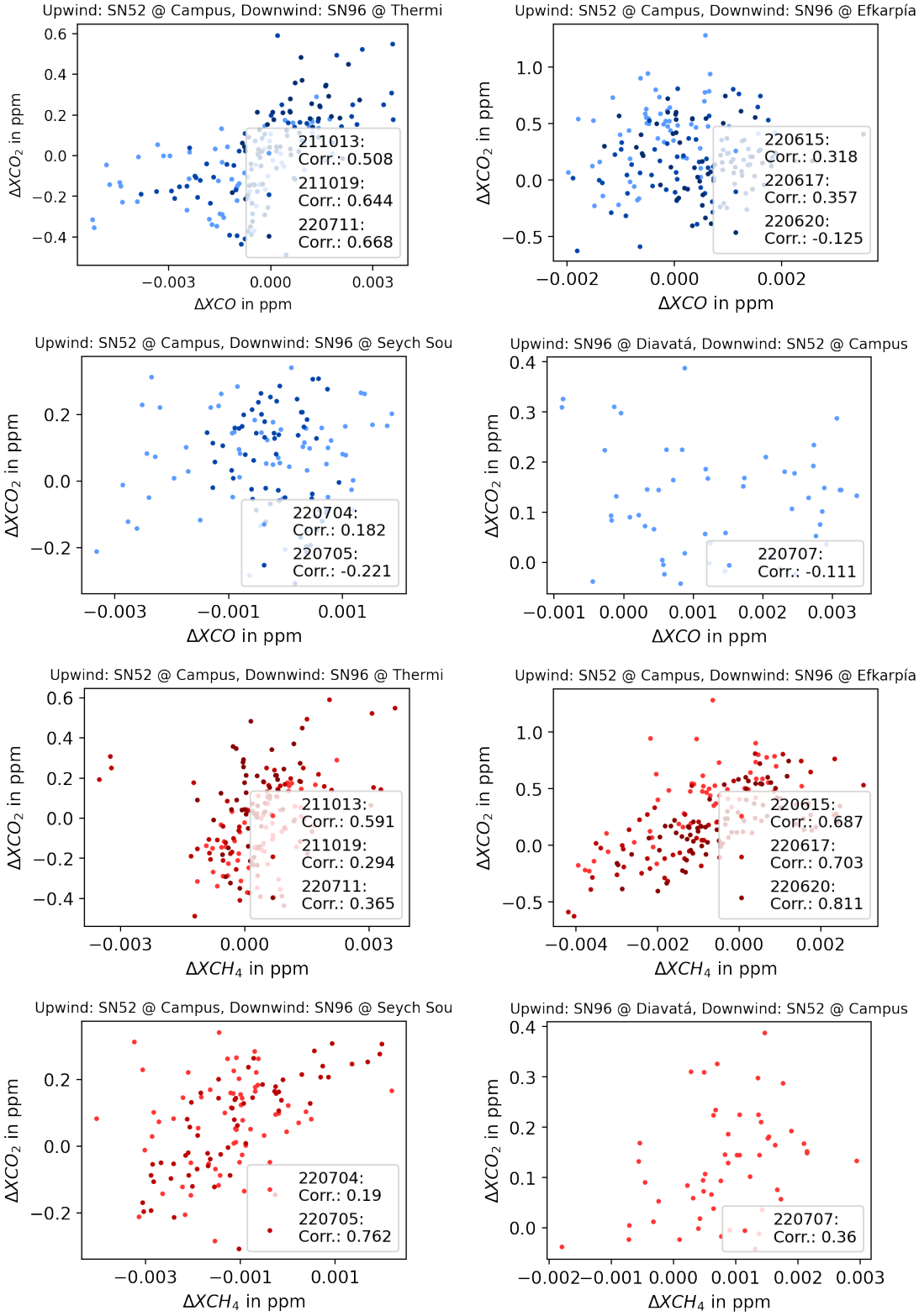

Figure 4.7.: Correlations between XCO_2 and XCO as well as for XCO_2 and XCH_4 for up- and downwind measurement days.

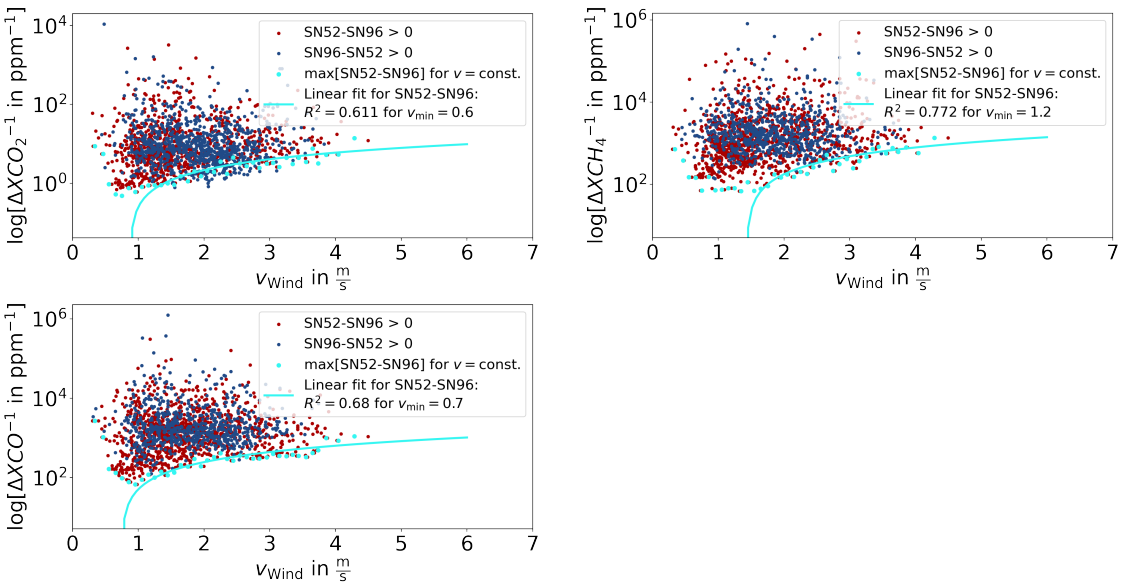

Figure 4.8.: Correlation between $\Delta X\text{gas}$ and wind speed v with fit. Red dots show enhanced concentrations at the Campus site in the city center (SN52) relative to SN96, while the blue dots represent those if the instrument SN96 measures larger concentration. The logarithmic scale is chosen to cover large values of $\Delta X\text{gas}^{-1}$. The data displayed in turquoise shows maximum values of $\Delta X\text{gas}$ for amplified concentration in the city center (SN52-SN96). The linear function is fitted to the data shown in turquoise. Hereby, v_{min} is optimized to maximum R^2 for each tracer. Wind speed data is from the Meteorology station at AUTh.

Table 4.7.: Selected time intervals and wind speed and for the estimation of emission fluxes at calm wind conditions. The mean values and standard deviations correspond to averages of all three wind data sources used in the chosen interval. As the average wind speed on 2022-05-17 is relatively high, the result for this day can be interpreted as a test of the model in that case.

Date	Chosen Time Interval (Local Time)	$(\overline{v}_{\mathrm{Wind}} \pm \sigma)$ in $\frac{\mathrm{m}}{\mathrm{s}}$
2021-10-20	10:05 - 10:35	0.934 ± 0.164
2021-10-22	10:00 - 11:40	0.870 ± 0.271
2022-05-17	10:00 - 12:40	1.885 ± 0.660
2022-06-09	8:50 - 9:10	0.895 ± 0.289
2022-06-22	9:10 - 9:45	1.219 ± 0.478

logarithmic scale against v_{Wind}. Choosing this kind of scale is due to values $\Delta X\mathrm{gas} \rightarrow 0$ yielding large values in the reciprocal. The relative enhancements of Xgas are split, distinguishing the instruments: an enhanced concentration measured by SN96 (especially interesting for up- and downwind measurements) is displayed by blue dots while red dots are used for the opposite case. As the main interest in this section is quantifying possible enhancements measured in the city center, the maximum values of ΔXgas (minimum values of $\Delta X\mathrm{gas}^{-1}$, respectively) for small intervals of v_{Wind} are taken and linearly fitted. The linear fit is optimized in the coefficient of determination R^2 for variable v_{Wind} to find v_{min} with the best possible linear fit. Therefore, one can state that the behaviour of ΔXgas for $v_{\mathrm{Wind}} < v_{\mathrm{min}}$ cannot be described by the box model with a linear relationship (Equation 2.24). Finding a changing wind dependency of ΔXgas for small v_{Wind} underlines the approach of the light wind case. Figure 4.8 further shows that for small wind speed, the concentration enhancement in the city center (red dots) are higher than for the "satellite" instrument SN96.

For this estimation the chosen relative alignment of the two instruments is not important. Therefore, all measurement days of the present campaign are considered. Of interest are intervals with low wind speeds (average under $1\,\frac{\mathrm{m}}{\mathrm{s}}$) and steadily increasing trace gas concentration. With these requirements, time intervals are selected and listed in Table 4.7. To get a general idea of the global wind situation in and around the city, all available wind data sets are used and averaged. For the calculation of the area emission flux, the formula given in Equation 2.27 is used. The gas specific constant k_{gas} and the total dry air column TC_{DryAir} are obtained as listed in Table 4.4. Temporal changes in Xgas are calculated discretely in 5 minute intervals:

$$\frac{\partial X_{\mathrm{gas}}}{\partial t} \rightarrow \frac{X_{\mathrm{gas}}(t + 5\,\mathrm{min}) - X_{\mathrm{gas}}(t)}{5\,\mathrm{min}}. \tag{4.3}$$

Using this interval size is reasonable as it is the same as for the resampled spectrometric data (preparation in subsection 4.0.1). Wind data is accordingly linearly interpolated to 5 minute intervals to fit the spectrometric data.

Figure 4.9 shows an exemplary plot of the data measured at light wind conditions. The remaining days can be seen in the Appendix A.2.5. The data displayed in Figure 4.9 has

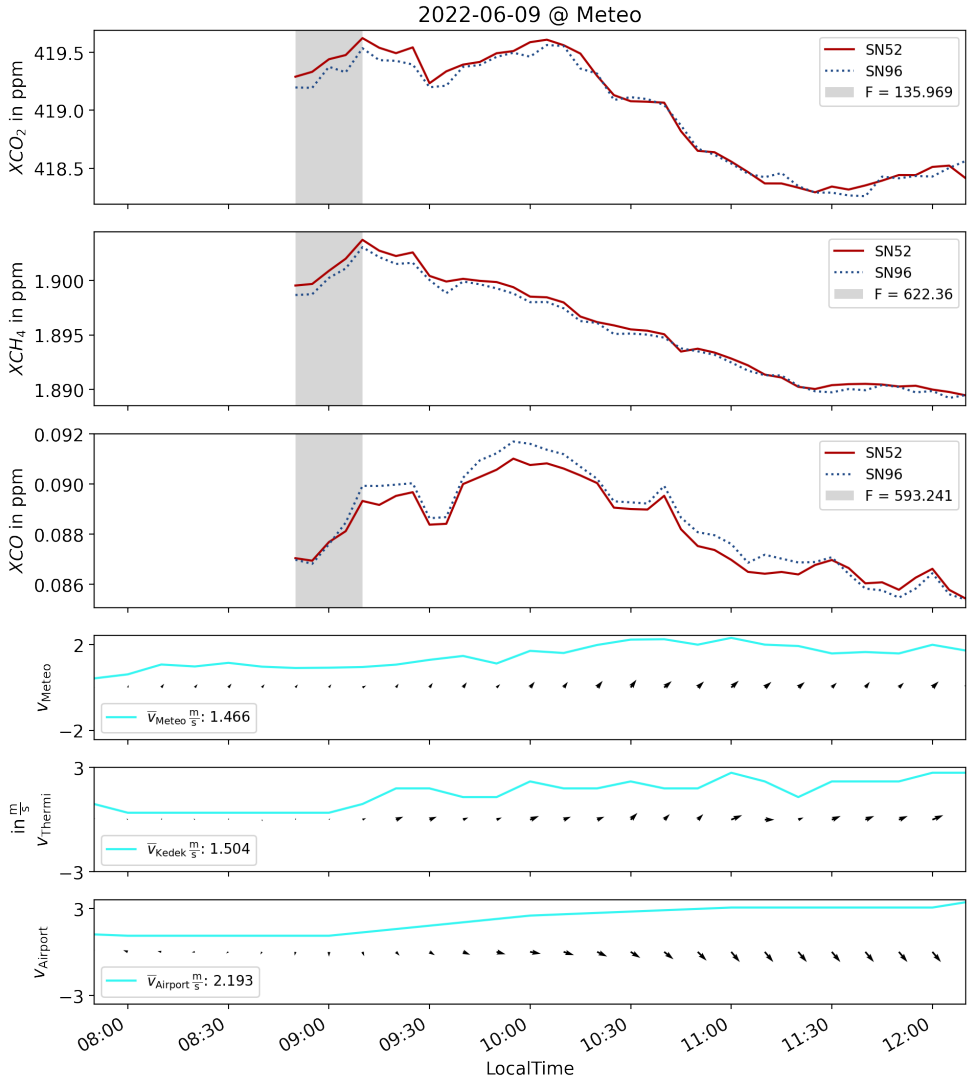

Figure 4.9.: Exemplary plot of DMFs, area flux and wind data for measurements with light wind conditions on the Campus on 2022-06-09. The emission fluxes are calculated for the SN52 instrument located at the Campus in the chosen time interval as given in Table 4.7. The wind data is displayed one hour earlier because the effects of the wind are measured late. The according visualization of the other light wind days can be found in the Appendix A.2.5.

Table 4.8.: Final numerical results for the estimated emission fluxes at calm wind conditions with attached errors. The standard deviations are corresponding to the mean values of the daily results.

	Mean Value	Error Propagation	Standard Deviation
F_{CO2} in $\frac{kt}{km^2 yr}$	179.247	0.356	17.846
F_{CH4} in $\frac{t}{km^2 yr}$	262.802	0.521	35.275
F_{CO} in $\frac{t}{km^2 yr}$	559.746	1.105	100.755

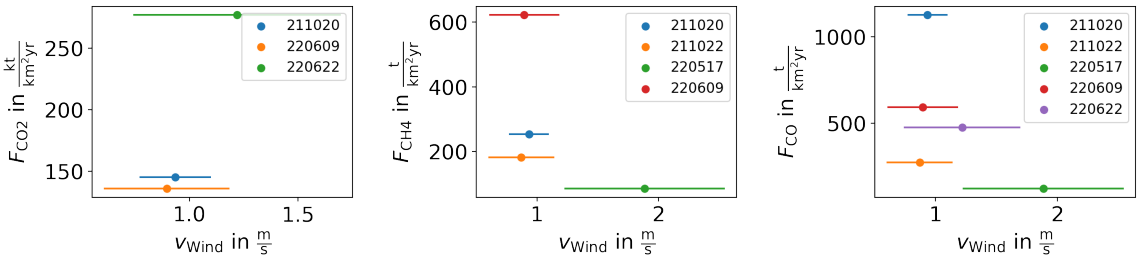

Figure 4.10.: Mean area emission fluxes for calm wind conditions. For the given dates (e.g. "211020"), the flux is calculated for the selected interval as given in Table 4.7. Wind speed is the average $\bar{v}_{Wind}$ between v_{Meteo}, v_{Thermi} and $v_{Airport}$ in the chosen interval while the error bars are the corresponding mean standard deviations.

been collected on 2022-06-09 with SN52 placed on Campus and the SN96 in Thermi. A correlated increase of concentration for all three trace gases is visible in the time period between 8:54 - 9:10. The wind speed is low in this period as well as in the hour before, hinting a possible accumulation of gases.

The averaged results for the area emission flux calculated for low wind speed are displayed in Table 4.8. Hereby, the averages are calculated for the intervals given in Table 4.7. To get the overall average, value obtained for each interval is weighted with the interval length. For the mean area emission flux, the values exceed the "up- and downwind" fluxes (Figure 4.6) and the EDGAR based values (Table 3.2) by one order of magnitude. Attached to the results are errors calculated via error propagation (subsection 4.2.2): in this case the only assumed error is on the ground pressure $\sigma_{P_{gr}} = \pm 2$ hPa. For the considered boundary case, the statistical error represented by the standard deviation of the mean value of all measurement days is the dominant error. This could be due to only few parameters going into the calculation but large uncertainty through the assumption $v_{Wind} \rightarrow 0$ and the natural deviation from it.

To further evaluate those large variations in area emission flux, the underlying model should be kept in mind. Wind speed near zero is a rare situation in Thessaloniki. Considering the full data plots in Appendix A.2.5, a correlation between wind speed and emission flux can be observed. In Figure 4.10, the mean area flux is plotted against the averaged wind speeds in the chosen intervals. This partly illustrates the suspected correlation in that aspect that high emissions correspond to low wind speeds. A greater amount of

Table 4.9.: Final results for estimation of area emission flux including the wind scaling factor k_{Wind} for F_{UpDown}.

Tracer	F_{UpDown} (Table 4.6)	$F_{v\to 0}$ (Table 4.8)
CO_2	$(59.905 \pm 49.153 \pm 8.668)\ \frac{\mathrm{kt}}{\mathrm{km^2 yr}}$	$(179.247 \pm 0.356 \pm 17.846)\ \frac{\mathrm{kt}}{\mathrm{km^2 yr}}$
CH_4	$(17.113 \pm 78.133 \pm 12.573)\ \frac{\mathrm{t}}{\mathrm{km^2 yr}}$	$(262.802 \pm 0.521 \pm 35.275)\ \frac{\mathrm{t}}{\mathrm{km^2 yr}}$
CO	$(66.093 \pm 156.072 \pm 25.963)\ \frac{\mathrm{t}}{\mathrm{km^2 yr}}$	$(559.746 \pm 1.105 \pm 100.755)\ \frac{\mathrm{t}}{\mathrm{km^2 yr}}$

Table 4.10.: Literature values for area emission flux to compare with.

Tracer	F in $\frac{\mathrm{kt}}{\mathrm{km^2 yr}}$	City	Source
CO_2	23.8	Thessaloniki	EDGAR data base (Table 3.2)
	28.3	Berlin	[Has+15]
	$40 - 89$	St. Petersburg	[Mak+21]
	29.1	London	[OSh+14]
	F in $\frac{\mathrm{t}}{\mathrm{km^2 yr}}$		
CH_4	136.9	Thessaloniki	EDGAR data base
	$120 - 170$	St. Petersburg	[Mak+21]
	65.6	London	[OSh+14]
CO	$90 - 333$	St. Petersburg	[Mak+21]
	106.0	London	[OSh+14]

data could collected at calm wind conditions could support the statement of a possible correlation between emission flux and wind speeds.

4.4. Discussion of the Results

Having applied different methods to analyze the present data set, the results are summarized in the following. Thereby, the main focus is to bring together the different results for area emission fluxes of the measured trace gases CO_2, CH_4 and CO. These results then can be compared to results for the corresponding quantities provided by literature.

Table 4.9 presents the final results of area emission fluxes for CO_2, CH_4 and CO. The values obtained from the up- downwind measurement include the wind scaling factor $k_{\mathrm{Wind}} = 3.428$. The given numbers consist of the mean value for all considered days of each setup with the added error propagation and the standard deviation corresponding to the mean value. One should keep in mind, that F_{UpDown} is obtained for up- and downwind setups covering a different part of the city. In contrast, $F_{v\to 0}$ only contains the data from the Campus site near the city center.

Comparing the retrieved results in (Table 4.9) to those from literature in (Table 4.10), an overlap is noticed. The emission flux F_{UpDown} of CO_2 is in agreement with the inventory

values while for CH_4, the measured emissions are lower but with a large uncertainty. F_{UpDown} for CO is smaller concerning its mean value than found in the literature. Considering the results obtained with the light wind estimate, $F_{v\to 0}$, the values exceed the emissions given by the inventory. It should be noted that the figures given in the literature are based on up- and downwind measurements. It is therefore difficult to compare results obtained in calm conditions with them.

The obtained deviations on the area flux reflect the simplistic approach of the box model itself (including the light wind case). Meteorological conditions in 3D are difficult to describe in a 1D model. The analysis could be modified in many ways, with different wind situations in certain intervals, deviations of the ideal instrument alignment, or scaling of the wind parameters to different altitude or even in a lateral direction.

Besides a refined analysis, an important source of uncertainty is having a relatively low amount of measurement data in comparison to the amount of parameters: covering the area of the city with more instruments on each day would support the significance of statements for differing wind directions. One possibility would be installing instruments to secure places and operate them remotely. Several approaches to protect the sensitive spectrometers from precipitation are already applied or in development. More reliable wind data from different locations in and around the city and especially for altitude could also be used to improve the analysis. Finally, more measurement days and longer daily measuring with the result of increasing the chance for more days of different wind situations.

Taken the hardware of the present campaign, more humanpower would help to position the instruments more flexible by moving both instruments on a daily basis. The satellite-like setup has a limited potential to cover the city.

5. Summary and Outlook

Here, the outcomes of a measurement campaign with two Bruker^{TM} EM27/SUN spectrometers in Thessaloniki, Greece, are presented. The campaign was in October 2021 and summer 2022, supplementing the long-term measurements in Thessaloniki [Mer+21] as a contribution to the COCCON network. Using a pair of EM27/SUNs, the goal of the campaign was the estimation of area emission fluxes for the GHGs CO_2, CH_4 and CO.

An important tool that is used to estimate emission fluxes is a box model. It is fed by measurements with an up- and downwind alignment of a pair of spectrometers measuring column-averaged DMFs: one instrument set in upwind position, ideally measuring background concentrations and a second instrument in downwind measuring possible signals from emission in between the spectrometers. As the ideal alignment cannot be realized in practice, background measurements are performed to quantify the lateral variability. The observed variability allows an estimate of the background-induced uncertainties in the emission fluxes. As another method to estimate GHG emissions, a boundary case of the box model is applied: for low wind speeds $v \rightarrow 0$, accumulations near the instrument's location can be measured.

The EM27/SUN spectrometer measures total column abundances of trace gases in the atmosphere. To convert them into DMFs, data of reliable ground pressure is important. Therefore, a scaling factor for each measurement site is calculated relative to a reference height. This is done by carrying a portable pressure sensor to each measurement site and observing the deviations relative to a fix located reference pressure level. For all parts of the further analysis, wind data plays a key role. As the wind data sets available in reasonably short time steps are measured near ground level, a scaling of the wind speed to altitude is performed, using openly available sounding data from the nearby airport. This leads to a wind speed scaling factor of 3.428 ± 1.123, converting the wind speeds measured in the city center at ground level to the mean wind speed in the PBL. It is applied in the calculations of area emission fluxes. To ensure comparability of DMFs on a sub percent level, a total of eight calibration days of the instruments are executed before, during and at the end of the campaign. Calibration factors measured on three days in October 2021 and five days in summer 22 are averaged to obtain one factor for each GHG to be used in the analysis. Further, one of the campaign instruments is calibrated before the campaign to the COCCON reference device in Karlsruhe.

The results for the area emission flux of the considered trace gases are 59.9 $\frac{\mathrm{kt}}{\mathrm{km^2 yr}}$ for CO_2, 17.1 $\frac{\mathrm{t}}{\mathrm{km^2 yr}}$ for CH_4 and 66.1 $\frac{\mathrm{t}}{\mathrm{km^2 yr}}$ for CO. Those results are obtained using eight days of measurements with the up- and downwind setup. Decisive for the selection of the included days is how the wind direction corresponds to the chosen instrument configuration on the particular day. Further, two days of measuring in the up- and downwind setup has been excluded from the results due to highly deviating numbers probably caused by the

topographical situation of the involved sites. The results are subject to uncertainties in order of 100 %. In the error propagation integrated are the measured deviations ΔXgas for the background configuration with small distance. Using a boundary calculation for the box model at calm wind conditions to estimate area emission fluxes, the following values are found: 179.2 $\frac{\mathrm{kt}}{\mathrm{km^2 yr}}$ for CO_2, 262.8 $\frac{\mathrm{t}}{\mathrm{km^2 yr}}$ for CH_4 and 559.7 $\frac{\mathrm{t}}{\mathrm{km^2 yr}}$ for CO. The uncertainty on these values is caused by the systematic error due to the boundary approximation assuming $v \rightarrow 0$ and lies at a maximum 18 %. Compared to literature values of emission fluxes from other cities or EDGAR based figures, the values obtained for Thessaloniki with the models used are in the same range.

Partly reflected in the large inaccuracies are limitations of the performed measurement campaign. Those are a limited coverage of the city due to only two instruments with one movable. On the other side, this has the advantage of low infrastructural effort and low cost. Further, information concerning the wind situation at altitude is extrapolated in a simplistic way potentially leading to wrong assessments. Precise and also three-dimensional wind data would support analyzing the results. Potentially, the numerical weather forecast model Icon-ART is applicable to reach a more realistic trace gas distribution and transport. Research on this is currently in progress [Fel+21]. Lastly, a larger data set would increase the statistical significance of the results. For the emission estimations at calm wind conditions, the long-term measurements at AUTh [Mer+21] could be used too.

Bibliography

[Alb+22a] Carlos Alberti et al. “Improved calibration procedures for the EM27/SUN spectrometers of the COllaborative Carbon Column Observing Network (COCCON)”. In: (2022). Medium: PDF Publisher: Copernicus Publications. DOI: 10.5445/IR/1000145878. URL: https://publikationen.bibliothek.kit.edu/1000145878 (visited on 06/16/2022).

[Alb+22b] Carlos Alberti et al. “Investigation of spaceborne trace gas products over St Petersburg and Yekaterinburg, Russia, by using COllaborative Column Carbon Observing Network (COCCON) observations”. In: *Atmospheric Measurement Techniques* 15.7 (Apr. 13, 2022), pp. 2199–2229. ISSN: 1867-8548. DOI: 10.5194/amt-15-2199-2022. URL: https://amt.copernicus.org/articles/15/2199/2022/ (visited on 01/09/2023).

[APK22] Peter W. Atkins, Julio de Paula, and James J. Keeler. *Physikalische Chemie. Hauptband*. Trans. by Cord Hartmann. 6. Auflage. Weinheim: WILEY-VCH, 2022. 1203 pp. ISBN: 978-3-527-82833-3.

[Bal21] C. Balaji. “Introduction to Atmospheric Radiation”. In: *Essentials of Radiation Heat Transfer*. Cham: Springer International Publishing, 2021, pp. 185–191. ISBN: 978-3-030-62617-4. DOI: 10.1007/978-3-030-62617-4_6. URL: http://link.springer.com/10.1007/978-3-030-62617-4_6 (visited on 01/20/2023).

[Bar] Vaisala Barocap. “PTB330 Digital Barometer for Professional Meteorology, Aviation, and Industrial Users”. In: (). URL: https://www.vaisala.com/sites/default/files/documents/PTB330-datasheet-B210708EN-E.pdf.

[Bec+18] Hylke E. Beck et al. “Present and future Köppen-Geiger climate classification maps at 1-km resolution”. In: *Scientific Data* 5.1 (Dec. 18, 2018), p. 180214. ISSN: 2052-4463. DOI: 10.1038/sdata.2018.214. URL: http://www.nature.com/articles/sdata2018214 (visited on 12/14/2022).

[Bee92] Reinhard Beer. *Remote sensing by Fourier transform spectrometry*. Vol. 170. John Wiley & Sons, 1992. ISBN: 978-0-471-55346-5.

[BHM20] Arne Babenhauserheide, Frank Hase, and Isamu Morino. “Net CO_2 fossil fuel emissions of Tokyo estimated directly from measurements of the Tsukuba TCCON site and radiosondes”. In: *Atmospheric Measurement Techniques* 13.5 (May 27, 2020), pp. 2697–2710. ISSN: 1867-8548. DOI: 10.5194/amt-13-2697-2020. URL: https://amt.copernicus.org/articles/13/2697/2020/ (visited on 11/23/2022).

[Cha60] Subrahmanyan Chandrasekhar. *Radiative transfer*. Dover books on physics. New York: Dover Publications, 1960. 393 pp. ISBN: 0-486-60590-6.

[Dav] Davis Instruments. *Used Manual for Vantage Pro2 and Vantage Pro2 Plus Weather Stations*. URL: https://cdn.shopify.com/s/files/1/0515/5992/3873/files/07395_234_Manual_VP2_Console_RevZ_web.pdf?v=1656098534 (visited on 12/10/2023).

[Dem16] Wolfgang Demtröder. "Moleküle". In: *Experimentalphysik 3*. Series Title: Springer-Lehrbuch. Berlin, Heidelberg: Springer Berlin Heidelberg, 2016, pp. 275–330. ISBN: 978-3-662-49094-5. DOI: 10.1007/978-3-662-49094-5_9. URL: http://link.springer.com/10.1007/978-3-662-49094-5_9 (visited on 01/19/2023).

[Die+21] Florian Dietrich et al. "MUCCnet: Munich Urban Carbon Column network". In: *Atmospheric Measurement Techniques* 14.2 (Feb. 11, 2021), pp. 1111–1126. ISSN: 1867-8548. DOI: 10.5194/amt-14-1111-2021. URL: https://amt.copernicus.org/articles/14/1111/2021/ (visited on 01/25/2023).

[Dor+11] Kelen Dornelles et al. "THERMAL PERFORMANCE OF WHITE SOLAR-REFLECTIVE PAINTS FOR COOL ROOFS AND THE INFLUENCE ON THE THERMAL COMFORT AND BUILDING ENERGY USE IN HOT CLIMATES". In: (2011). Publisher: Unpublished. DOI: 10.13140/RG.2.1.1745.5843. URL: http://rgdoi.net/10.13140/RG.2.1.1745.5843 (visited on 01/16/2023).

[Dör12] Andreas Dörnbrack. "The Atmosphere: Vast, Shallow, and Full of Subtleties". In: *Atmospheric Physics*. Ed. by Ulrich Schumann. Series Title: Research Topics in Aerospace. Berlin, Heidelberg: Springer Berlin Heidelberg, 2012, pp. 3–16. ISBN: 978-3-642-30182-7. DOI: 10.1007/978-3-642-30183-4_1. URL: http://link.springer.com/10.1007/978-3-642-30183-4_1 (visited on 01/17/2023).

[Eur21] European Commission. Joint Research Centre. *GHG emissions of all world: 2021 report.* LU: Publications Office, 2021. URL: https://data.europa.eu/doi/10.2760/173513 (visited on 12/16/2022).

[Eur22] European Commission. Joint Research Centre. *CO2 emissions of all world countries :JRC/IEA/PBL 2022 report.* LU: Publications Office, 2022. URL: https://data.europa.eu/doi/10.2760/730164 (visited on 01/11/2023).

[Fel+21] Lena Feld et al. *Quantification of greenhouse gas emissions in Thessaloniki.* other. oral, Dec. 18, 2021. DOI: 10.5194/dach2022-230. URL: https://meetingorganizer.copernicus.org/DACH2022/DACH2022-230.html (visited on 12/19/2022).

[Fra+15] C. Frankenberg et al. "The Orbiting Carbon Observatory (OCO-2): spectrometer performance evaluation using pre-launch direct sun measurements". In: *Atmospheric Measurement Techniques* 8.1 (Jan. 14, 2015), pp. 301–313. ISSN: 1867-8548. DOI: 10.5194/amt-8-301-2015. URL: https://amt.copernicus.org/articles/8/301/2015/ (visited on 01/06/2023).

[Fre+15] M. Frey et al. “Calibration and Application of an Array of Portable FTIR Spectrometers (EM27/SUN) for Detecting Greenhouse Gas Emissions”. In: 2015 (Dec. 1, 2015). Conference Name: AGU Fall Meeting Abstracts ADS Bibcode: 2015AGUFM.A21G0240F, A21G–0240. URL: https://ui.adsabs.harvard.edu/abs/2015AGUFM.A21G0240F (visited on 01/23/2023).

[Fre+19] Matthias Frey et al. “Building the COllaborative Carbon Column Observing Network (COCCON): long-term stability and ensemble performance of the EM27/SUN Fourier transform spectrometer”. In: *Atmospheric Measurement Techniques* 12.3 (Mar. 11, 2019), pp. 1513–1530. ISSN: 1867-8548. DOI: 10.5194/amt-12-1513-2019. URL: https://amt.copernicus.org/articles/12/1513/2019/ (visited on 12/01/2022).

[Fre18] Matthias Max Frey. “Characterisation and application of portable solar absorption spectrometers for the detection of greenhouse gas emissions from regional anthropogenic sources”. In: (2018). Medium: PDF Publisher: Karlsruhe. DOI: 10.5445/IR/1000088312. URL: https://publikationen.bibliothek.kit.edu/1000088312 (visited on 11/28/2022).

[Gad10] Kenneth Gade. “A Non-singular Horizontal Position Representation”. In: *Journal of Navigation* 63.3 (July 2010), pp. 395–417. ISSN: 0373-4633, 1469-7785. DOI: 10.1017/S0373463309990415. URL: https://www.cambridge.org/core/product/identifier/S0373463309990415/type/journal_article (visited on 01/11/2023).

[GHK08] Donald Gatley, Sebastian Herrmann, and Hans-Joachim Kretzschmar. “A Twenty-First Century Molar Mass for Dry Air”. In: *HVAC&R Research* 14.5 (Sept. 1, 2008), pp. 655–662. ISSN: 1078-9669. DOI: 10.1080/10789669.2008.10391032. URL: http://www.tandfonline.com/doi/abs/10.1080/10789669.2008.10391032 (visited on 11/22/2022).

[Gis+11] M. Gisi et al. “Camtracker: a new camera controlled high precision solar tracker system for FTIR-spectrometers”. In: *Atmospheric Measurement Techniques* 4.1 (Jan. 19, 2011), pp. 47–54. ISSN: 1867-8548. DOI: 10.5194/amt-4-47-2011. URL: https://amt.copernicus.org/articles/4/47/2011/ (visited on 03/29/2022).

[Gis+12] M. Gisi et al. “XCO_2-measurements with a tabletop FTS using solar absorption spectroscopy”. In: *Atmospheric Measurement Techniques* 5.11 (Nov. 29, 2012), pp. 2969–2980. ISSN: 1867-8548. DOI: 10.5194/amt-5-2969-2012. URL: https://amt.copernicus.org/articles/5/2969/2012/ (visited on 01/06/2023).

[Gis12] Michael Gisi. “Setup of precise camera based solar tracker systems and greenhouse gas measurements using a modified portable spectrometer”. In: (2012). Medium: PDF Publisher: Karlsruhe. DOI: 10.5445/IR/1000031248. URL: https://publikationen.bibliothek.kit.edu/1000031248 (visited on 01/17/2023).

[Gor+22] Iouli Gordon et al. "HITRAN2020: new and improved molecular spectroscopic data for modelling spectra of planetary atmospheres". In: 54 (Dec. 1, 2022). Conference Name: AAS/Division for Planetary Sciences Meeting Abstracts ADS Bibcode: 2022DPS....5421602G, p. 216.02. URL: https://ui.adsabs.harvard.edu/abs/2022DPS....5421602G (visited on 01/21/2023).

[Has+15] F. Hase et al. "Application of portable FTIR spectrometers for detecting greenhouse gas emissions of the major city Berlin". In: *Atmospheric Measurement Techniques* 8.7 (July 31, 2015), pp. 3059–3068. ISSN: 1867-8548. DOI: 10.5194/amt-8-3059-2015. URL: https://amt.copernicus.org/articles/8/3059/2015/ (visited on 04/11/2022).

[Has+16] Frank Hase et al. "Addition of a channel for XCO observations to a portable FTIR spectrometer for greenhouse gas measurements". In: *Atmospheric Measurement Techniques* 9.5 (May 25, 2016), pp. 2303–2313. ISSN: 1867-8548. DOI: 10.5194/amt-9-2303-2016. URL: https://amt.copernicus.org/articles/9/2303/2016/ (visited on 01/06/2023).

[Has00] Frank Hase. "Inversion von Spurengasprofilen aus hochaufgelösten bodengebundenen FTIR-Messungen in Absorption". PhD thesis. Dissertation, Karlsruhe, Universität Karlsruhe (TH), 2000, 2000. URL: https://d-nb.info/115193836X/34.

[Has12] F. Hase. "Improved instrumental line shape monitoring for the ground-based, high-resolution FTIR spectrometers of the Network for the Detection of Atmospheric Composition Change". In: *Atmospheric Measurement Techniques* 5.3 (Mar. 23, 2012), pp. 603–610. ISSN: 1867-8548. DOI: 10.5194/amt-5-603-2012. URL: https://amt.copernicus.org/articles/5/603/2012/ (visited on 01/18/2023).

[HBH82] Steven R. Hanna, Gary A. Briggs, and Rayford P. Hosker. *Handbook on atmospheric diffusion: prepared for the Office of Health and Environmental Research, Office of Energy Research, U.S. Department of Energy*. In collab. with United States and United States. Oak Ridge, TN: Technical Information Center, U.S. Dept. of Energy, 1982. 102 pp. ISBN: 978-0-87079-127-7.

[HBP99] Frank Hase, Thomas Blumenstock, and Clare Paton-Walsh. "Analysis of the instrumental line shape of high-resolution Fourier transform IR spectrometers with gas cell measurements and new retrieval software". In: *Applied Optics* 38.15 (May 20, 1999), p. 3417. ISSN: 0003-6935, 1539-4522. DOI: 10.1364/AO.38.003417. URL: https://opg.optica.org/abstract.cfm?URI=ao-38-15-3417 (visited on 01/18/2023).

[Hel22] Hellenic Statistical Authority (ELSTAT). *Customer Residents 2021*. July 19, 2022. URL: https://elstat-outsourcers.statistics.gr/Census2022_GR.pdf (visited on 01/22/2023).

[HS15] Ingolf V. Hertel and Claus-Peter Schulz. *Atoms, Molecules and Optical Physics 2*. Graduate Texts in Physics. Berlin, Heidelberg: Springer Berlin Heidelberg, 2015. ISBN: 978-3-642-54313-5. DOI: 10.1007/978-3-642-54313-5. URL: http://link.springer.com/10.1007/978-3-642-54313-5 (visited on 01/19/2023).

[IPC21] IPCC. *Climate Change 2021: The Physical Science Basis. Contribution of Working Group I to the Sixth Assessment Report of the Intergovernmental Panel on Climate Change*. Vol. In Press. Type: Book. Cambridge, United Kingdom and New York, NY, USA: Cambridge University Press, 2021. DOI: 10.1017/9781009157896.

[IPC22] IPCC. *Global Warming of 1.5°C: IPCC Special Report on Impacts of Global Warming of 1.5°C above Pre-industrial Levels in Context of Strengthening Response to Climate Change, Sustainable Development, and Efforts to Eradicate Poverty*. 1st ed. Cambridge University Press, June 9, 2022. ISBN: 978-1-00-915794-0. DOI: 10.1017/9781009157940. URL: https://www.cambridge.org/core/product/identifier/9781009157940/type/book (visited on 01/20/2023).

[Ken+09] Christopher Kennedy et al. "Greenhouse Gas Emissions from Global Cities". In: *Environmental Science & Technology* 43.19 (Oct. 1, 2009), pp. 7297–7302. ISSN: 0013-936X, 1520-5851. DOI: 10.1021/es900213p. URL: https://pubs.acs.org/doi/10.1021/es900213p (visited on 01/07/2023).

[Kie16] Matthäus Kiel. "Trace gas measurements from different spectral regions using FTIR spectroscopy". In: (2016). Publisher: Karlsruhe. DOI: 10.5445/IR/1000056859. URL: http://digbib.ubka.uni-karlsruhe.de/volltexte/1000056859 (visited on 01/17/2023).

[Kla+15a] F. Klappenbach et al. "Accurate mobile remote sensing of XCO_2 and XCH_4 latitudinal transects from aboard a research vessel". In: *Atmospheric Measurement Techniques* 8.12 (Dec. 1, 2015), pp. 5023–5038. ISSN: 1867-8548. DOI: 10.5194/amt-8-5023-2015. URL: https://amt.copernicus.org/articles/8/5023/2015/ (visited on 12/09/2022).

[Kla+15b] Friedrich Klappenbach et al. "Remote sensing of XCO_2 and XCH_4 above the Atlantic from aboard the research vessel Polarstern". In: (Apr. 1, 2015). Conference Name: EGU General Assembly Conference Abstracts ADS Bibcode: 2015EGUGA..1711798K, p. 11798. URL: https://ui.adsabs.harvard.edu/abs/2015EGUGA..1711798K (visited on 01/06/2023).

[Ku66] H.H. Ku. "Notes on the use of propagation of error formulas". In: *Journal of Research of the National Bureau of Standards, Section C: Engineering and Instrumentation* 70C.4 (Oct. 1966), p. 263. ISSN: 0022-4316. DOI: 10.6028/jres.070C.025. URL: https://nvlpubs.nist.gov/nistpubs/jres/70C/jresv70Cn4p263_A1b.pdf (visited on 01/27/2023).

[Lau+22] Joshua L. Laughner et al. *A new algorithm to generate a priori trace gas profiles for the GGG2020 retrieval algorithm*. preprint. Gases/Remote Sensing/Data Processing and Information Retrieval, Oct. 11, 2022. DOI: 10.5194/amt-2022-

267. URL: https://amt.copernicus.org/preprints/amt-2022-267/ (visited on 01/24/2023).

[Le +15] C. Le Quéré et al. "Global carbon budget 2014". In: *Earth System Science Data* 7.1 (May 8, 2015), pp. 47–85. ISSN: 1866-3516. DOI: 10.5194/essd-7-47-2015. URL: https://essd.copernicus.org/articles/7/47/2015/ (visited on 01/06/2023).

[Mak+21] Maria V. Makarova et al. "Emission Monitoring Mobile Experiment (EMME): an overview and first results of the St. Petersburg megacity campaign 2019". In: *Atmospheric Measurement Techniques* 14.2 (Feb. 10, 2021), pp. 1047–1073. ISSN: 1867-8548. DOI: 10.5194/amt-14-1047-2021. URL: https://amt.copernicus.org/articles/14/1047/2021/ (visited on 03/10/2022).

[McK10] Wes McKinney. "Data structures for statistical computing in python". In: Proceedings of the 9th Python in Science Conference. Vol. 445. Austin, TX, 2010, pp. 51–56.

[Men+17] Víctor M. Mendoza et al. "Atmospheric emissivity with clear sky computed by E-Trans/HITRAN". In: *Atmospheric Environment* 155 (Apr. 2017), pp. 174–188. ISSN: 13522310. DOI: 10.1016/j.atmosenv.2017.01.048. URL: https://linkinghub.elsevier.com/retrieve/pii/S1352231017300560 (visited on 01/30/2023).

[Mer+21] Marios Mermigkas et al. "FTIR Measurements of Greenhouse Gases over Thessaloniki, Greece in the Framework of COCCON and Comparison with S5P/TROPOMI Observations". In: *Remote Sensing* 13.17 (Aug. 26, 2021), p. 3395. ISSN: 2072-4292. DOI: 10.3390/rs13173395. URL: https://www.mdpi.com/2072-4292/13/17/3395 (visited on 04/19/2022).

[Möl19] Detlev Möller. *Fundamentals and Processes*. De Gruyter, Feb. 18, 2019. ISBN: 978-3-11-056126-5. DOI: 10.1515/9783110561265. URL: https://www.degruyter.com/document/doi/10.1515/9783110561265/html (visited on 11/14/2022).

[Mor+11] I. Morino et al. "Preliminary validation of column-averaged volume mixing ratios of carbon dioxide and methane retrieved from GOSAT short-wavelength infrared spectra". In: *Atmospheric Measurement Techniques* 4.6 (June 15, 2011), pp. 1061–1076. ISSN: 1867-8548. DOI: 10.5194/amt-4-1061-2011. URL: https://amt.copernicus.org/articles/4/1061/2011/ (visited on 01/06/2023).

[Nyq28] H. Nyquist. "Certain Topics in Telegraph Transmission Theory". In: *Transactions of the American Institute of Electrical Engineers* 47.2 (Apr. 1928), pp. 617–644. ISSN: 0096-3860. DOI: 10.1109/T-AIEE.1928.5055024. URL: http://ieeexplore.ieee.org/document/5055024/ (visited on 01/18/2023).

[OSh+14] Sebastian J. O'Shea et al. "Area fluxes of carbon dioxide, methane, and carbon monoxide derived from airborne measurements around Greater London: A case study during summer 2012: Area fluxes from airborne measurements". In: *Journal of Geophysical Research: Atmospheres* 119.8 (Apr. 27, 2014), pp. 4940–4952. ISSN: 2169897X. DOI: 10.1002/2013JD021269. URL: http://doi.wiley.com/10.1002/2013JD021269 (visited on 01/04/2023).

[Oza+21] Yukihiro Ozaki et al., eds. *Near-infrared spectroscopy: theory, spectral analysis, instrumentation, and applications*. Singapore: Springer Nature, 2021. 593 pp. ISBN: 978-981-15-8648-4.

[Par+11] Robert Parker et al. "Methane observations from the Greenhouse Gases Observing SATellite: Comparison to ground-based TCCON data and model calculations: GOSAT CH $_4$ OBSERVATIONS". In: *Geophysical Research Letters* 38.15 (Aug. 2011). ISSN: 00948276. DOI: 10.1029/2011GL047871. URL: http://doi.wiley.com/10.1029/2011GL047871 (visited on 01/06/2023).

[PCE] PCE Instruments. *Data Logger PCE-THB 40 Operational Manual*. URL: https://www.pce-instruments.com/english/api/getartfile?_fnr=1047568&_dsp=inline.

[PDS12] Michael Ponater, Simone Dietmüller, and Robert Sausen. "Greenhouse Effect, Radiative Forcing and Climate Sensitivity". In: *Atmospheric Physics*. Ed. by Ulrich Schumann. Series Title: Research Topics in Aerospace. Berlin, Heidelberg: Springer Berlin Heidelberg, 2012, pp. 85–100. ISBN: 978-3-642-30183-4. DOI: 10.1007/978-3-642-30183-4_6. URL: https://link.springer.com/10.1007/978-3-642-30183-4_6 (visited on 01/21/2023).

[Rod00] Clive D. Rodgers. *Inverse methods for atmospheric sounding: theory and practice*. Series on atmospheric, oceanic and planetary physics 2. Singapore: World Scientific, 2000. ISBN: 978-981-02-2740-1.

[Rot+13] L.S. Rothman et al. "The HITRAN2012 molecular spectroscopic database". In: *Journal of Quantitative Spectroscopy and Radiative Transfer* 130 (Nov. 2013), pp. 4–50. ISSN: 00224073. DOI: 10.1016/j.jqsrt.2013.07.002. URL: https://linkinghub.elsevier.com/retrieve/pii/S0022407313002859 (visited on 01/21/2023).

[Rot+87] L. S. Rothman et al. "The HITRAN database: 1986 edition". In: *Applied Optics* 26.19 (Oct. 1, 1987), p. 4058. ISSN: 0003-6935, 1539-4522. DOI: 10.1364/AO.26.004058. URL: https://opg.optica.org/abstract.cfm?URI=ao-26-19-4058 (visited on 01/21/2023).

[RS07] M. Ritzkowski and R. Stegmann. "Controlling greenhouse gas emissions through landfill in situ aeration". In: *International Journal of Greenhouse Gas Control* 1.3 (July 2007), pp. 281–288. ISSN: 17505836. DOI: 10.1016/S1750-5836(07)00029-1. URL: https://linkinghub.elsevier.com/retrieve/pii/S1750583607000291 (visited on 01/06/2023).

[Sag+22] Vijay Kumar Sagar et al. "Ground-based Remote Sensing of Total Columnar CO2, CH4, and CO using EM27/SUN FTIR spectrometer at a suburban location in India and validation of Sentinel-5p/TROPOMI". In: (2022). Publisher: TechRxiv.

[San+98] Vincenzo Santacesaria et al. "Lidar observations of the Planetary Boundary Layer above the city of Thessaloniki, Greece". In: (1998).

[Sha49] C.E. Shannon. "Communication in the Presence of Noise". In: *Proceedings of the IRE* 37.1 (Jan. 1949), pp. 10–21. ISSN: 0096-8390. DOI: 10.1109/JRPROC.1949.232969. URL: http://ieeexplore.ieee.org/document/1697831/ (visited on 01/17/2023).

[SP16] John H. Seinfeld and Spyros N. Pandis. *Atmospheric chemistry and physics: from air pollution to climate change*. Third edition. Hoboken, New Jersey: John Wiley & Sons, 2016. 1 p. ISBN: 978-1-119-22116-6.

[SSB14] Bjoern Ole Sander, Marianne Samson, and Roland J. Buresh. "Methane and nitrous oxide emissions from flooded rice fields as affected by water and straw management between rice crops". In: *Geoderma* 235-236 (Dec. 2014), pp. 355–362. ISSN: 00167061. DOI: 10.1016/j.geoderma.2014.07.020. URL: https://linkinghub.elsevier.com/retrieve/pii/S0016706114002912 (visited on 12/14/2022).

[TFK09] Kevin E. Trenberth, John T. Fasullo, and Jeffrey Kiehl. "Earth's Global Energy Budget". In: *Bulletin of the American Meteorological Society* 90.3 (Mar. 2009), pp. 311–324. ISSN: 0003-0007, 1520-0477. DOI: 10.1175/2008BAMS2634.1. URL: https://journals.ametsoc.org/doi/10.1175/2008BAMS2634.1 (visited on 01/30/2023).

[Tu+22] Qiansi Tu et al. "Quantification of CH_4 emissions from waste disposal sites near the city of Madrid using ground- and space-based observations of COCCON, TROPOMI and IASI". In: *Atmospheric Chemistry and Physics* 22.1 (Jan. 10, 2022), pp. 295–317. ISSN: 1680-7324. DOI: 10.5194/acp-22-295-2022. URL: https://acp.copernicus.org/articles/22/295/2022/ (visited on 04/11/2022).

[Tu19] Qiansi Tu. "Observation of atmospheric greenhouse gas abundances on regional scales in boreal areas using portable FTIR Spectrometers". In: (2019). Medium: PDF Publisher: Karlsruhe. DOI: 10.5445/IR/1000095901. URL: https://publikationen.bibliothek.kit.edu/1000095901 (visited on 12/13/2022).

[Uni15] United Nations. *Paris Agreement 2015*. Dec. 12, 2015. URL: https://treaties.un.org/Pages/ViewDetails.aspx?src=TREATY&mtdsg_no=XXVII-7-d&chapter=27&clang=_en (visited on 01/06/2023).

[Uni97] United Nations Framework Convention on Climate Change (UNFCCC). *Kyoto Protocol to the United Nations Framework Convention on Climate Change*. Dec. 10, 1997. URL: https://unfccc.int/resource/docs/convkp/kpeng.pdf (visited on 01/06/2023).

[Vee+12] J.P. Veefkind et al. "TROPOMI on the ESA Sentinel-5 Precursor: A GMES mission for global observations of the atmospheric composition for climate, air quality and ozone layer applications". In: *Remote Sensing of Environment* 120 (May 2012), pp. 70–83. ISSN: 00344257. DOI: 10.1016/j.rse.2011.09.027. URL: https://linkinghub.elsevier.com/retrieve/pii/S0034425712000661 (visited on 01/06/2023).

[Vir+20] Pauli Virtanen et al. “SciPy 1.0: fundamental algorithms for scientific computing in Python”. In: *Nature Methods* 17.3 (Mar. 2, 2020), pp. 261–272. ISSN: 1548-7091, 1548-7105. DOI: 10.1038/s41592-019-0686-2. URL: http://www.nature.com/articles/s41592-019-0686-2 (visited on 01/12/2023).

[Vui+07] Nicolas Vuichard et al. “Estimating the greenhouse gas fluxes of European grasslands with a process-based model: 2. Simulations at the continental level: GHG FLUXES IN EUROPEAN GRASSLANDS, 2”. In: *Global Biogeochemical Cycles* 21.1 (Mar. 2007). ISSN: 08866236. DOI: 10.1029/2005GB002612. URL: http://doi.wiley.com/10.1029/2005GB002612 (visited on 01/06/2023).

[Wun+11] Debra Wunch et al. “The Total Carbon Column Observing Network”. In: *Philosophical Transactions of the Royal Society A: Mathematical, Physical and Engineering Sciences* 369.1943 (May 28, 2011), pp. 2087–2112. ISSN: 1364-503X, 1471-2962. DOI: 10.1098/rsta.2010.0240. URL: https://royalsocietypublishing.org/doi/10.1098/rsta.2010.0240 (visited on 01/06/2023).

[WW08] Jerry Workman and Lois Weyer. *Practical guide to interpretive near-infrared spectroscopy*. OCLC: 1328811477. Boca Raton: CRC Press, 2008. ISBN: 978-0-429-11957-6.

A. Appendix

A.1. Appendix 1: Further Theoretical Derivations

A.1.1. Derivation of the Barometric Formula

An important relation in the present work is the behaviour of barometric pressure with altitude. Considering a surface parallel to the earth's surface with area A in the atmosphere, the pressure p acting on it is given by the mass m of the particles in the column above with height z and the gravitational acceleration g. With the density in the column $\rho = \frac{m}{V} = \frac{m}{A \cdot z}$, this can be written as

$$p = \frac{F}{A} = \frac{m \cdot g}{A} = \frac{\rho \cdot V \cdot g}{A} = \rho \cdot z \cdot g. \tag{A.1}$$

Moving on to a volume with infinitesimal height $\mathrm{d}z$ and the corresponding infinitesimal difference in pressure $\mathrm{d}p$, the equation from above reads

$$\begin{aligned} & p(z) - p(z + \mathrm{d}z) = g(z) \cdot \rho(z) \cdot \mathrm{d}z \\ \Leftrightarrow\ & p(z + \mathrm{d}z) - p(z) = -g(z) \cdot \rho(z) \cdot \mathrm{d}z \\ \Leftrightarrow\ & \frac{p(z + \mathrm{d}z) - p(z)}{\mathrm{d}z} = -\left(g(z) \cdot \frac{\rho(z)}{\mathrm{d}z} \cdot \mathrm{d}z + g(z) \cdot \rho(z) \cdot \frac{\mathrm{d}z}{\mathrm{d}z} \right), \end{aligned} \tag{A.2}$$

where in the last step was derived with respect to z. Letting $\mathrm{d}z \to 0$ then yields

$$\frac{\mathrm{d}p}{\mathrm{d}z} = -g(z) \cdot \rho(z). \tag{A.3}$$

As the atmosphere is mainly filled by gases, the ideal gas law provides an approximate description:

$$p \cdot V = n \cdot R \cdot T, \tag{A.4}$$

with the pressure p, the volume V, the temperature T, the amount of substance n and the ideal gas constant R. Putting the ideal gas equation in Equation A.3 and performing an integration from ground level $z = 0$ to z gives:

$$
\begin{aligned}
&\frac{1}{p(z)} \cdot \frac{\mathrm{d}p}{\mathrm{d}z} = -\frac{g \cdot m}{n \cdot R \cdot T} \equiv -\frac{1}{H} \\
\Leftrightarrow &\int_0^z \mathrm{d}z' \, \frac{\mathrm{d}p}{\mathrm{d}z'} \cdot \frac{1}{p(z)} = -\int_0^z \frac{\mathrm{d}z'}{H(z')} \\
\Leftrightarrow &\int_{p(0)}^{p(z)} \frac{\mathrm{d}p'}{p'(z)} = -\int_0^z \frac{\mathrm{d}z'}{H(z')} \\
\Leftrightarrow &\ln\left(\frac{p(z)}{p(0)}\right) = -\int_0^z \frac{\mathrm{d}z'}{H(z')} \\
\Leftrightarrow &\boxed{p(z) = p(0) \cdot \exp\left(-\int_0^z \frac{\mathrm{d}z'}{H(z')}\right).}
\end{aligned}
\tag{A.5}
$$

This equation is named the barometric formula with the scale height $H(z) = \frac{nRT(z)}{mg(z)} = \frac{RT(z)}{Mg(z)}$ ($M = \frac{m}{n}$ is the molar mass). The assumption that the temperature T and the gravitational acceleration g are independent of the height z lead to the often used approximation

$$
p(z) = p(0) \cdot \mathrm{e}^{-z/H} \tag{A.6}
$$

T is approximately linear with a slope < 2 [SP16] and g decreases with $\left(\frac{r_\mathrm{e}}{r_\mathrm{e}+z}\right)^2$ (r_e is the earth's radius) which is both a slower than the exponential behaviour of p. The scale height names the height for that the pressure decreases by a factor of e.

A.1.2. Derivation of the Total Column of Dry Air

The definition of total column amounts is given as the number of particles on the base area of the column:

$$
TC_\mathrm{DryAir} = \frac{N_\mathrm{DryAir}}{A}. \tag{A.7}
$$

As an educated guess, it is useful to consider the ground pressure P_gr, which is created by the mass of the wet air particles in the column above the ground. The entirety of particles can be split into dry air particles and water. With $\langle g \rangle$ being the column averaged gravitational factor and m the molecular masses, P_gr can be expressed as:

$$
P_\mathrm{gr} = \frac{\langle g \rangle}{A} \cdot \left(m_\mathrm{DryAir} \cdot N_\mathrm{DryAir} + m_{\mathrm{H_2O}} \cdot N_{\mathrm{H_2O}}\right). \tag{A.8}
$$

Solving this for $\frac{N_\mathrm{DryAir}}{A}$ and putting it into Equation A.7 yields

$$
TC_\mathrm{DryAir} = \frac{P_\mathrm{gr}}{\langle g \rangle \cdot m_\mathrm{DryAir}} - TC_{\mathrm{H_2O}} \cdot \frac{m_{\mathrm{H_2O}}}{m_\mathrm{DryAir}}, \tag{A.9}
$$

with $TC_{\mathrm{H_2O}} = \frac{N_{\mathrm{H_2O}}}{A}$.

A.1.3. Daily Measurement Notes: October Measurements

Table A.1.: Measurement notes for October 2021, Time is LocalTime, UTC+3

Date	SN52	SN96	Mode	Start	Stop	Comments
2021-10-04	Physics	Physics	Calibration	08:35	18:07	
2021-10-05	Physics	Physics	Calibration	09:07	17:30	
2021-10-06	Physics	Physics	Calibration	09:40	10:30	Cloudy, nearly no data
2021-10-13	Physics	Thermi	Up-Down	09:00	18:00	
2021-10-19	Physics	Thermi	Up-Down	09:05	18:00	
2021-10-20	Physics	Thermi	Background	09:50	16:40	Backgr. not from Sea
2021-10-22	Physics	Thermi	Background	09:30	15:30	

A.1.4. Daily Measurement Notes: Summer Measurements

Table A.2.: Measurement notes for summer 2022, Time is LocalTime, UTC+3

Date	SN52	SN96	Mode	Start	Stop	Comments
2022-05-12	Thermi	Thermi	Calibration	09:15	14:50	SN52: at 10:45: Fixed radius problem
2022-05-13	Thermi	Thermi	Calibration	09:45	15:30	
2022-05-17	Meteo	Galini	Up-Down	10:00	15:20	
2022-05-20	Meteo	Thermi	Up-Down	09:45	15:30	SN52: Until 10:40: `CamTracker` problems
2022-05-24	Meteo	Galini	Up-Down	09:45	13:55	SN96: Until 11:05: Loose cable, 1/2h data loss
2022-05-25	Meteo	Galini	Up-Down	09:40	14:30	
2022-06-09	Meteo	Meteo	Calibration	08:30	12:10	
2022-06-14	Meteo	Galini	Up-Down	09:30	13:30	SN96: 10:05: Sun not cen-, tered, corrected morph
2022-06-15	Meteo	Efkarpia	Up-Down	10:50	15:45	
2022-06-17	Meteo	Efkarpia	Up-Down	08:45	15:20	SN96: Until 11:20: Ca. 1/2h sun not centered
2022-06-20	Meteo	Efkarpia	Up-Down	09:40	15:15	
2022-06-21	Meteo	Diavata	Up-Down	09:55	15:30	
2022-06-22	Meteo	Diavata	Up-Down	09:00	12:50	
2022-06-24	Meteo	Thermi	Up-Down	13:00	15:45	SN96: Until 14:30: Unstable position of device, cloudy
2022-06-27	Meteo	Thermi	Background	09:40	13:25	SN52: CH2 A x8 Signal and x4 Background. Possibly unreliable data from 9.6.
2022-06-29	Meteo	Thermi	Up-Down	11:45	16:25	SN96: 16:00 Sun not centered (not enough Power)
2022-07-01	Meteo	Physics	Background	11:00	16:30	
2022-07-02	Meteo	Physics	Background	11:00	14:30	SN52: clicking noise increases, end of spectra with artefacts
2022-07-04	Meteo	Seych Sou	Up-Down	10:45	15:00	
2022-07-05	Meteo	Seych Sou	Up-Down	09:30	15:00	SN52: Blackout at morning
2022-07-06	Meteo	Meteo	Calibration	09:45	16:15	
2022-07-07	Meteo	Diavata	Up-Down	09:50	15:00	SN96: 12:00 short break due to a tractor mowing meadow
2022-07-11	Meteo	Thermi	Up-Down	09:50	14:30	
2022-07-12	Meteo	Meteo	Calibration	09:45	15:38	SN96: 12:00 Sun not Centered

A.1.5. Daily Measurement Notes: History of Pressure Sensor Location

Table A.3.: History of pressure sensor location in summer 2022

Date	Departure	Arrival	Destination	Comment
2022-05-09	18:00	18:30	Ano Poli	Timestamp: UTC
2022-05-13	04:42	06:08	Thermi	
2022-05-13	12:51	14:36	Ano Poli	
2022-05-17	04:43	06:30	Galini	
2022-05-17	12:31	13:50	Ano Poli	
2022-05-18	06:18	06:51	Meteo Up	
2022-05-18	12:35	14:07	Ano Poli	
2022-05-19	07:10	07:28	Meteo Up	
2022-05-19	13:48	14:09	Ano Poli	
2022-05-20	05:54	06:34	Thermi	
2022-05-20	09:58	10:28	Ano Poli	
2022-05-24	04:01	05:23	Galini	Timestamp: UTC-1
2022-05-24	10:08	12:09	Ano Poli	
2022-05-25	03:58	05:32	Galini	
2022-05-25	10:45	12:48	Ano Poli	
2022-06-09	04:40	04:57	Meteo Up	
2022-06-09	12:38	13:00	Ano Poli	
2022-06-14	04:10	05:20	Galini	
2022-06-14	09:45	10:35	Meteo Down	
2022-06-15	06:15	06:42	Efkarpia	
2022-06-15	12:05	12:34	Meteo Down	
2022-06-17	03:59	04:37	Efkarpia	
2022-06-17	11:42	12:14	Meteo Down	
2022-06-20	05:00	05:22	Efkarpia	
2022-06-20	11:29	11:56	Meteo Down	
2022-06-21	05:04	05:48	Diavata	
2022-06-21	12:01	12:43	Meteo Down	
2022-06-22	03:58	04:52	Diavata	
2022-06-22	09:01	09:49	Meteo Down	
2022-06-24	05:03	05:46	Thermi	
2022-06-29	13:15	13:52	Meteo Down	
2022-07-01	06:27	07:04	Physics	
2022-07-04	05:11	05:36	Seych Sou	
2022-07-04	11:12	11:36	Meteo Down	
2022-07-05	05:00	05:23	Seych Sou	
2022-07-05	11:11	11:35	Meteo Down	
2022-07-06	05:12	06:25	Meteo Up	
2022-07-06	12:03	13:22	Meteo Down	
2022-07-07	05:10	05:45	Diavata	
2022-07-07	11:16	12:32	Meteo Down	
2022-07-11	05:01	06:12	Thermi	
2022-07-11	11:03	11:47	Meteo Down	
2022-07-12	05:12	06:00	Meteo Up	

A.2. Appendix 2: Data Collection

A.2.1. Calibration

A.2.1.1. Calibrations in Karlsruhe

The full data set of DMFs for CO_2, CH_4, CO and dry air for the side-by-side measurements in Karlsruhe is given in Figure A.1. Additionally, the solar zenith angle is shown to connect with the cut out areas. The method explained in subsection 3.6.1 is applied.

Having a look at *XAIR* in Figure A.1 to check the data for possible measurement issues, there are obvious signs on 21/09/01 and 21/09/02: Some lacking data and jumps in the *XAIR* graph for the SN96 device on 21/09/01 as well as a drifting curve followed by lacking data in the SN37 graph on 21/09/02. As there are no measurement notes available for these days, it is difficult to find the reason for these effects. Investigating `CamTracker` pictures especially on 21/09/02 could give a hint of possibly not optimal sun focus. Unfortunately on this day there were no pictures taken. Therefore, it is reasonable to cut out time intervals with unsafe data, which is on 21/09/01 from 12:30 to 16:30 and on 21/09/02 until 13:55. Further on 21/09/03, late times are cut out due to large SZA.

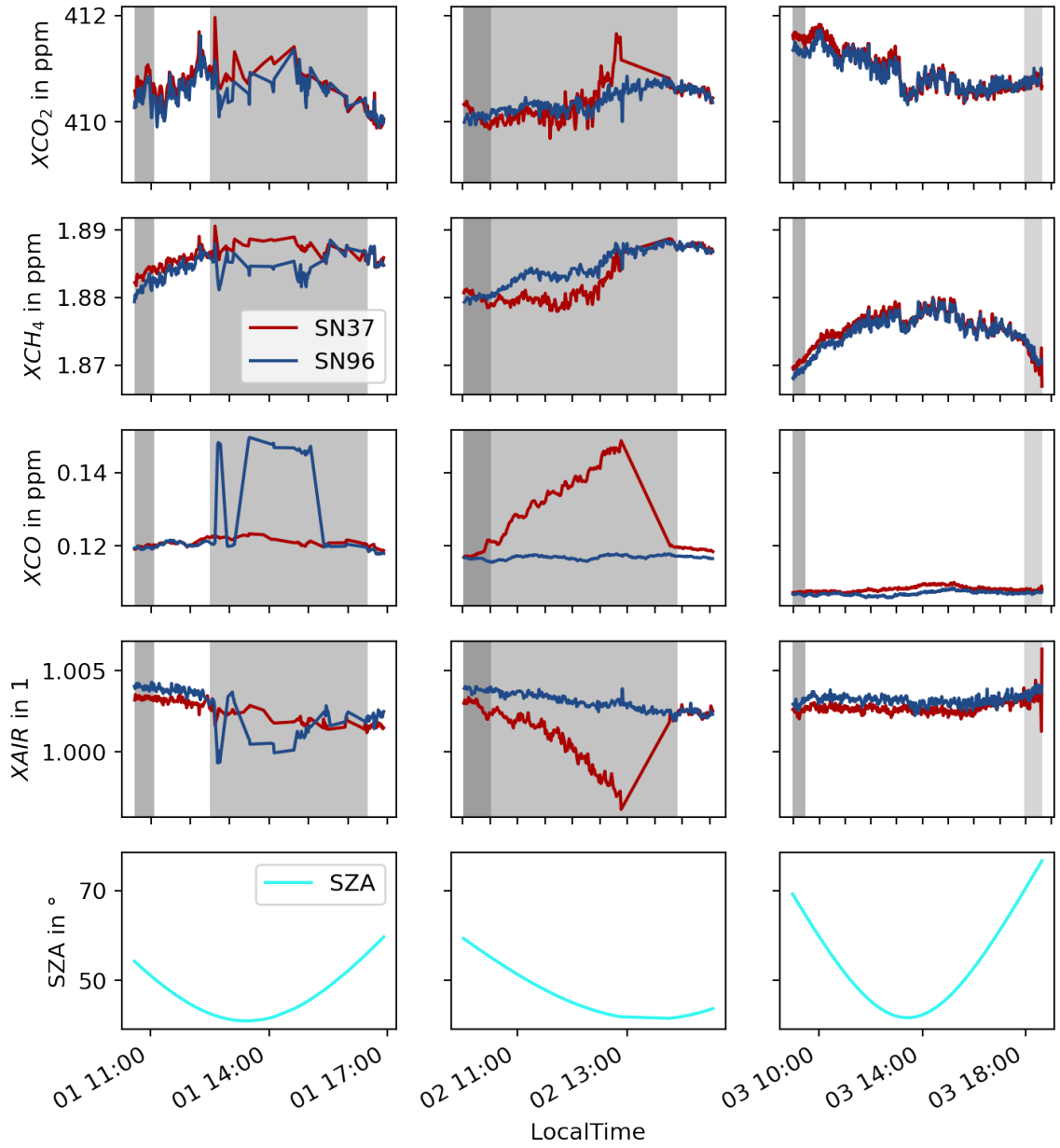

Figure A.1.: Retrieved column-averaged DMFs and solar zenith angles (SZA) for the pre-campaign calibration in Karlsruhe between 21/09/01 and 21/09/03. Here the complete data set is shown with the first 30 minutes each day (darkest grey), the intervals with measurement issues (medium grey) and those with SZA > 70° (lightest grey) being marked.

A.2.1.2. Calibrations in Thessaloniki

The full data set of DMFs for CO_2, CH_4, CO and dry air for the side-by-side measurements in Thessaloniki is given in Figure A.2. Additionally, the solar zenith angle is shown to connect with the cut out areas. The method explained in subsection 3.6.1 is applied. Measurement complications are listed in Appendix A.2.

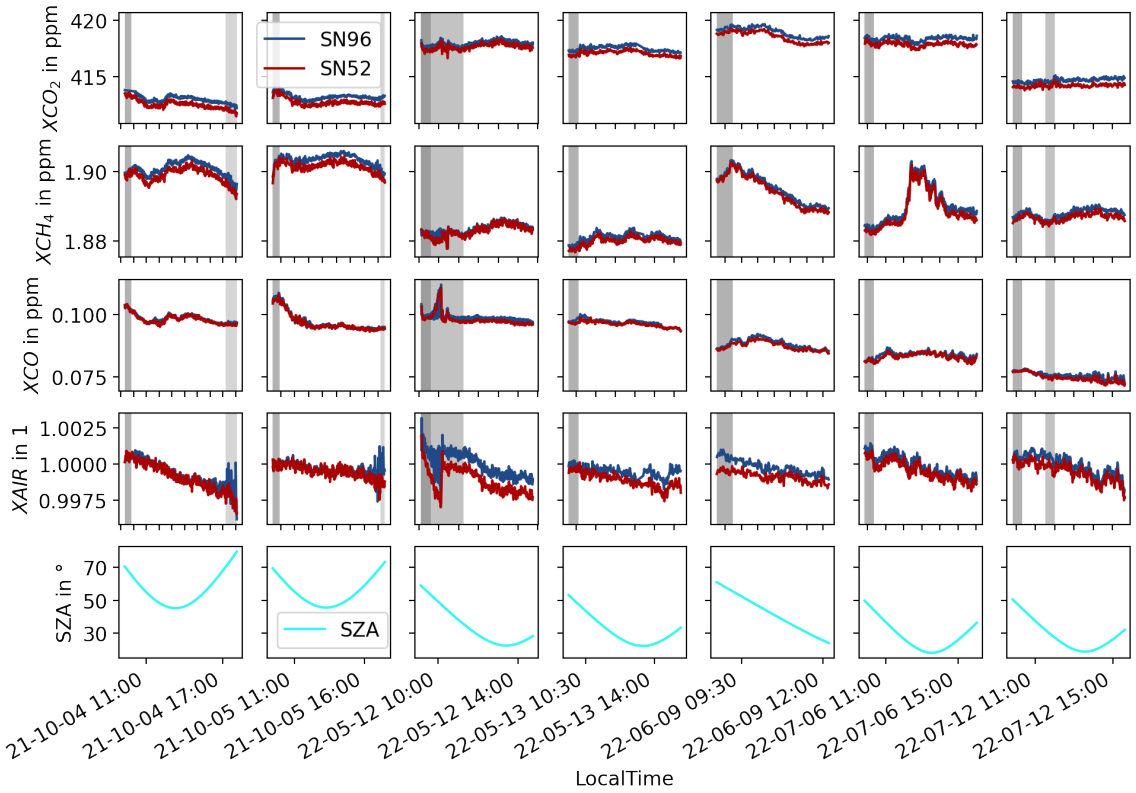

Figure A.2.: Retrieved column-averaged DMFs and solar zenith angles (SZA) for the calibration in Thessaloniki in October 2021 and summer 2022. Here the complete data set is shown with the first 30 minutes each day (darkest grey), the intervals with measurement issues (medium grey) and those with SZA > 70° (lightest grey) being marked.

A.2.2. Dry-air Mole Fractions for all Campaign Days

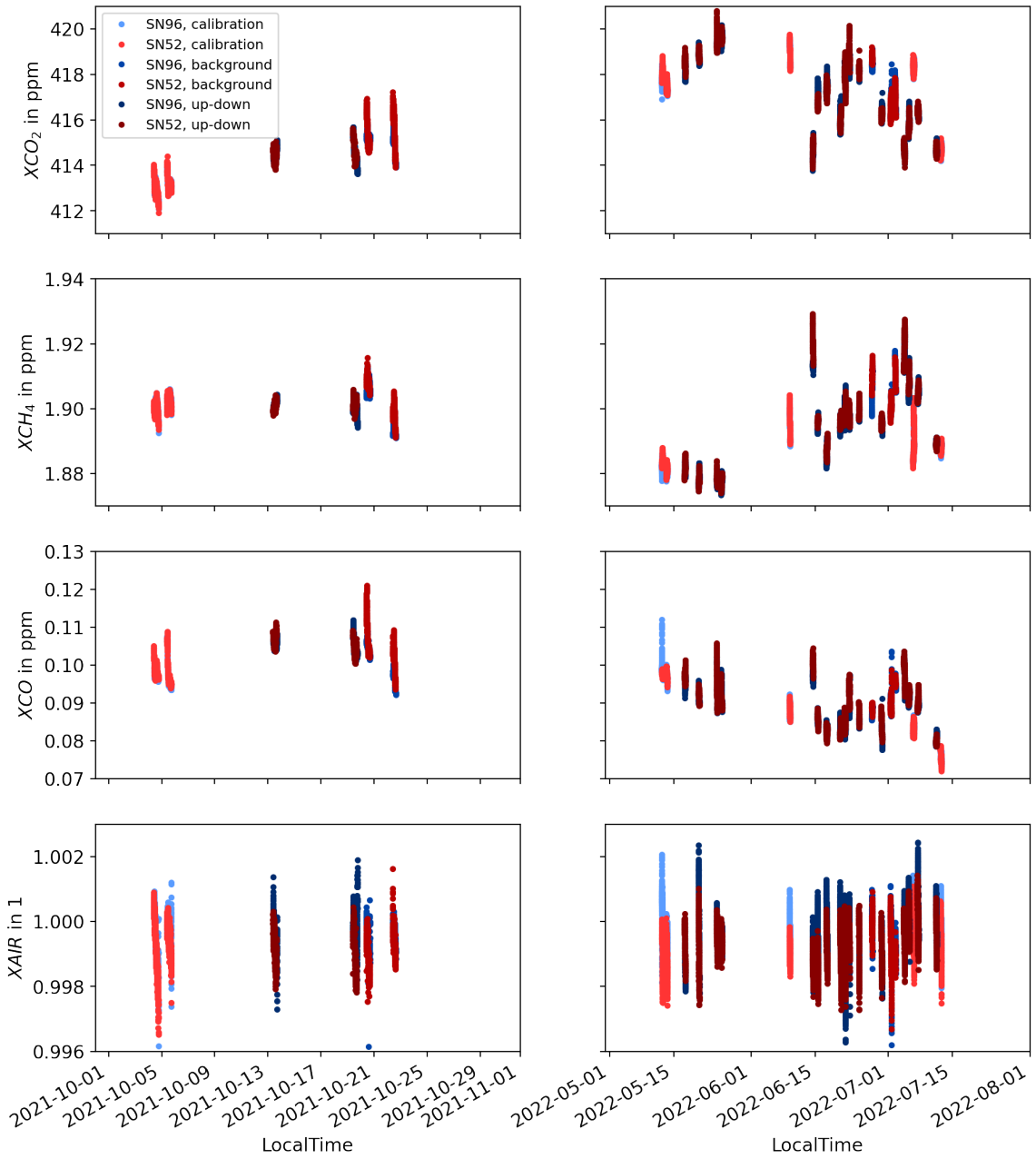

Figure A.3.: DMFs for all campaign days. *XAIR* differs from the ideal value 1 by maximum 0.4 % with an average of 0.999464 ± 0.000745 (mean value ± standard deviation) over the campaign.

A.2.3. Background Measurements

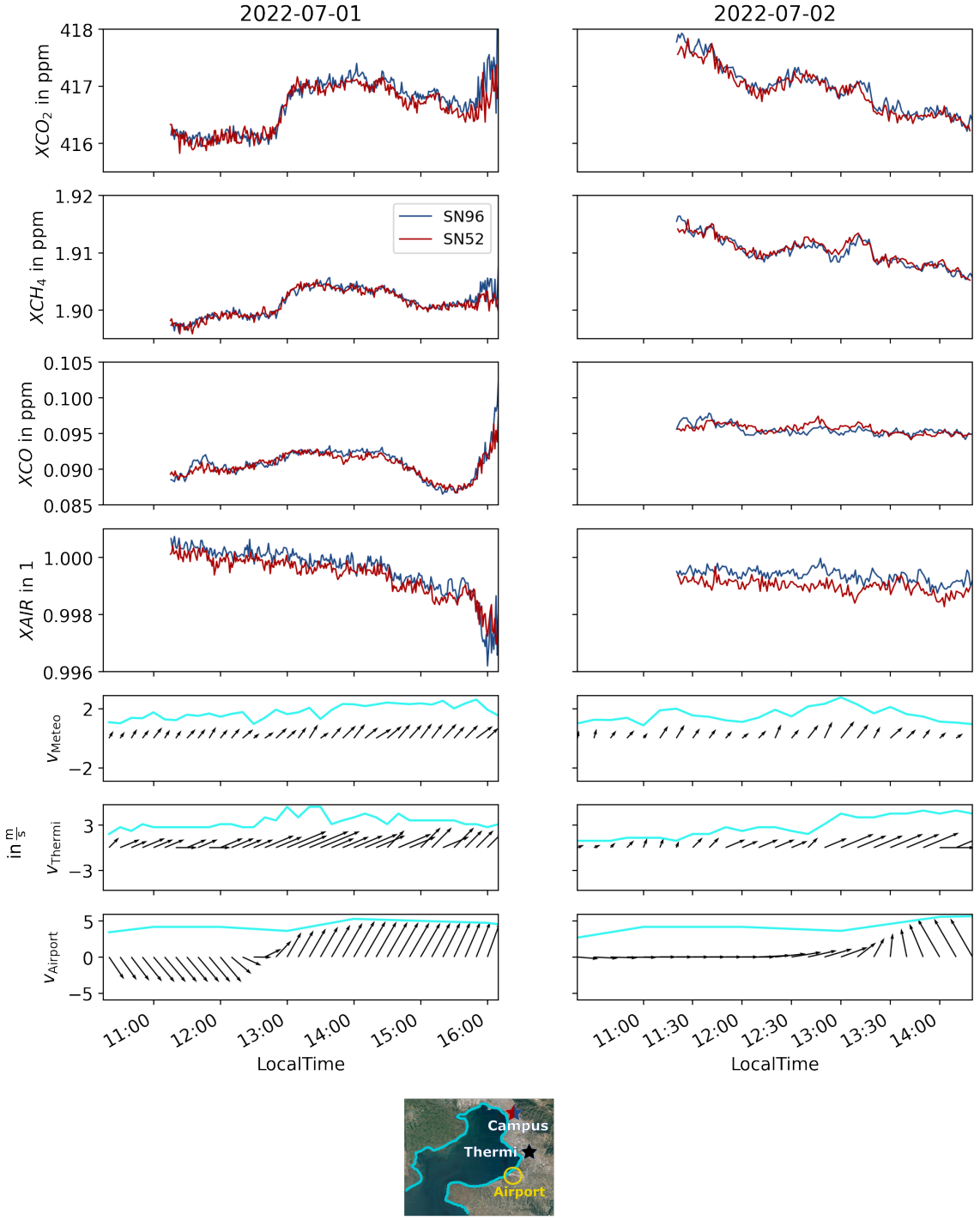

Figure A.4.: DMFs and wind data for background setup on 2022-07-01 and 2022-07-02. The small map serves for orientation concerning wind direction, which is mostly sea breeze for these days. The wind data is displayed one hour earlier because the effects of the wind are measured late.

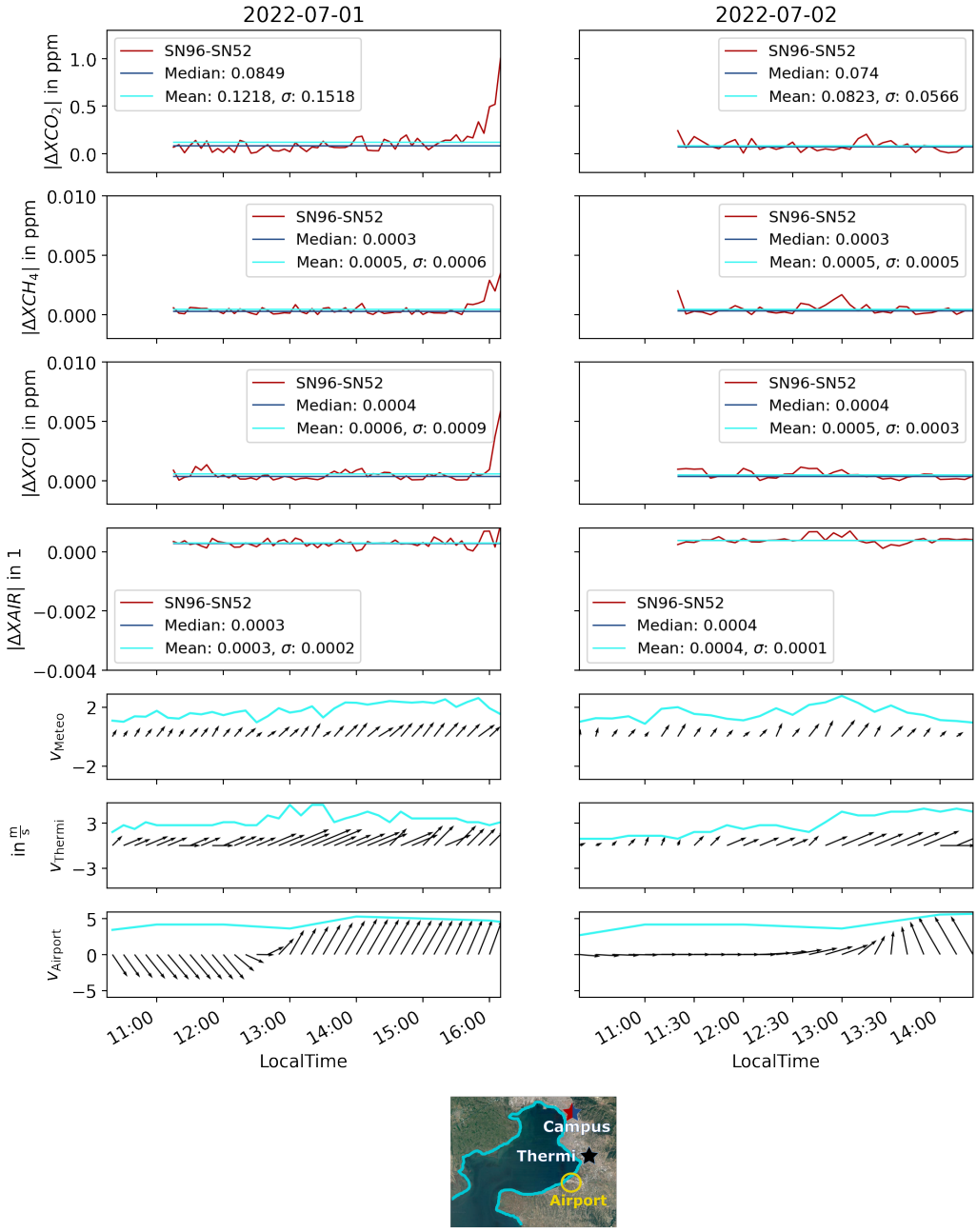

Figure A.5.: Background variability in dry-air mole fractions and wind data for Campus background setup on 2022-07-01 and 2022-07-02. The small map serves for orientation concerning wind direction, which is mostly sea breeze for these days.

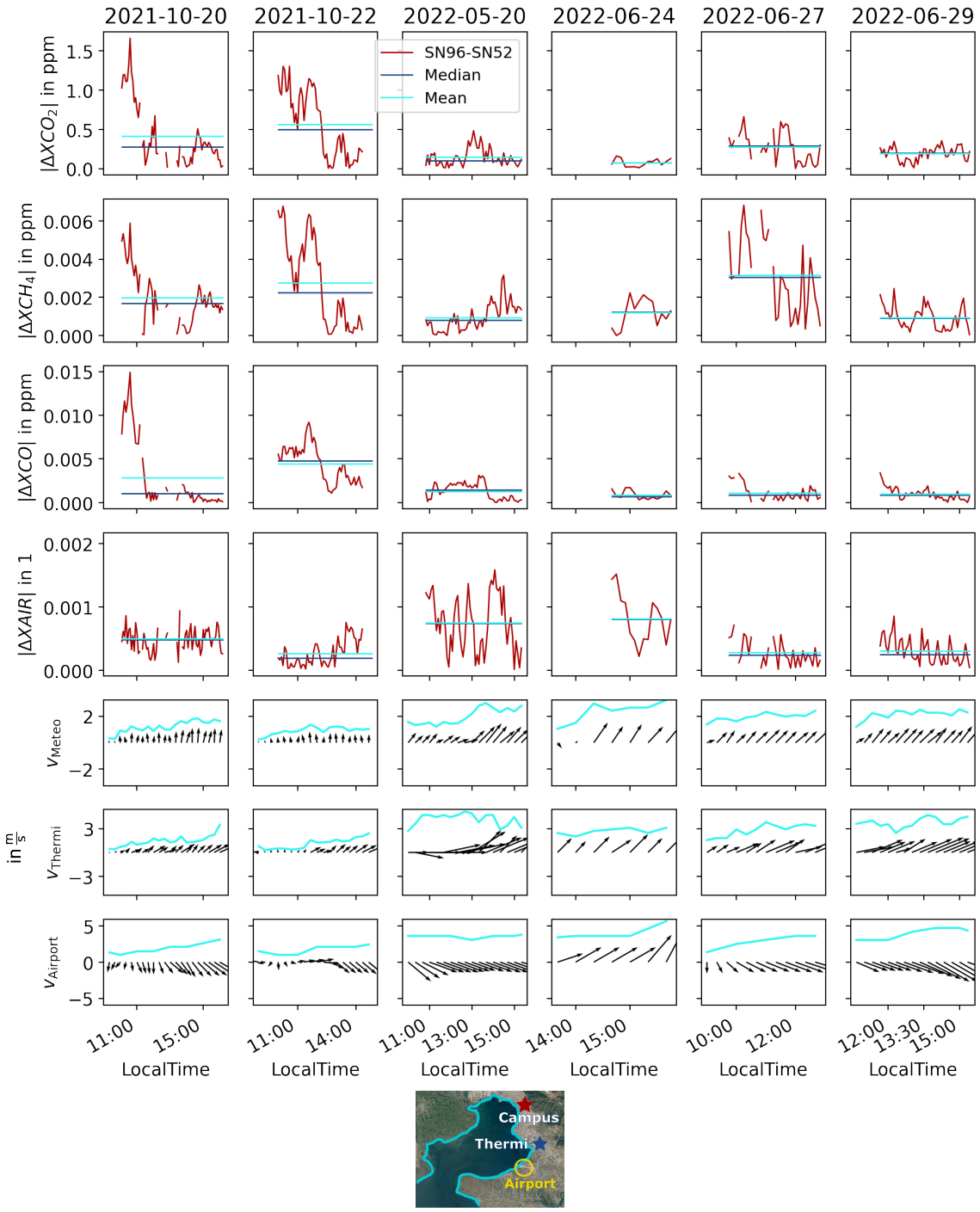

Figure A.6.: Variability in dry-air mole fractions and wind data for background measurements with larger distance on 2021-10-20, 2021-10-22, 2022-05-20, 2022-06-24, 2022-06-27 and 2022-06-29. SN52 is located at the Meteorology building on the Campus and SN96 at Thermi (ΚΕΔΕΚ). The small map serves for orientation concerning wind direction, which is mostly sea breeze for these days. The wind data is displayed one hour earlier because the effects of the wind are measured late.

A.2.4. Emission Flux: Up- and Downwind Measurements

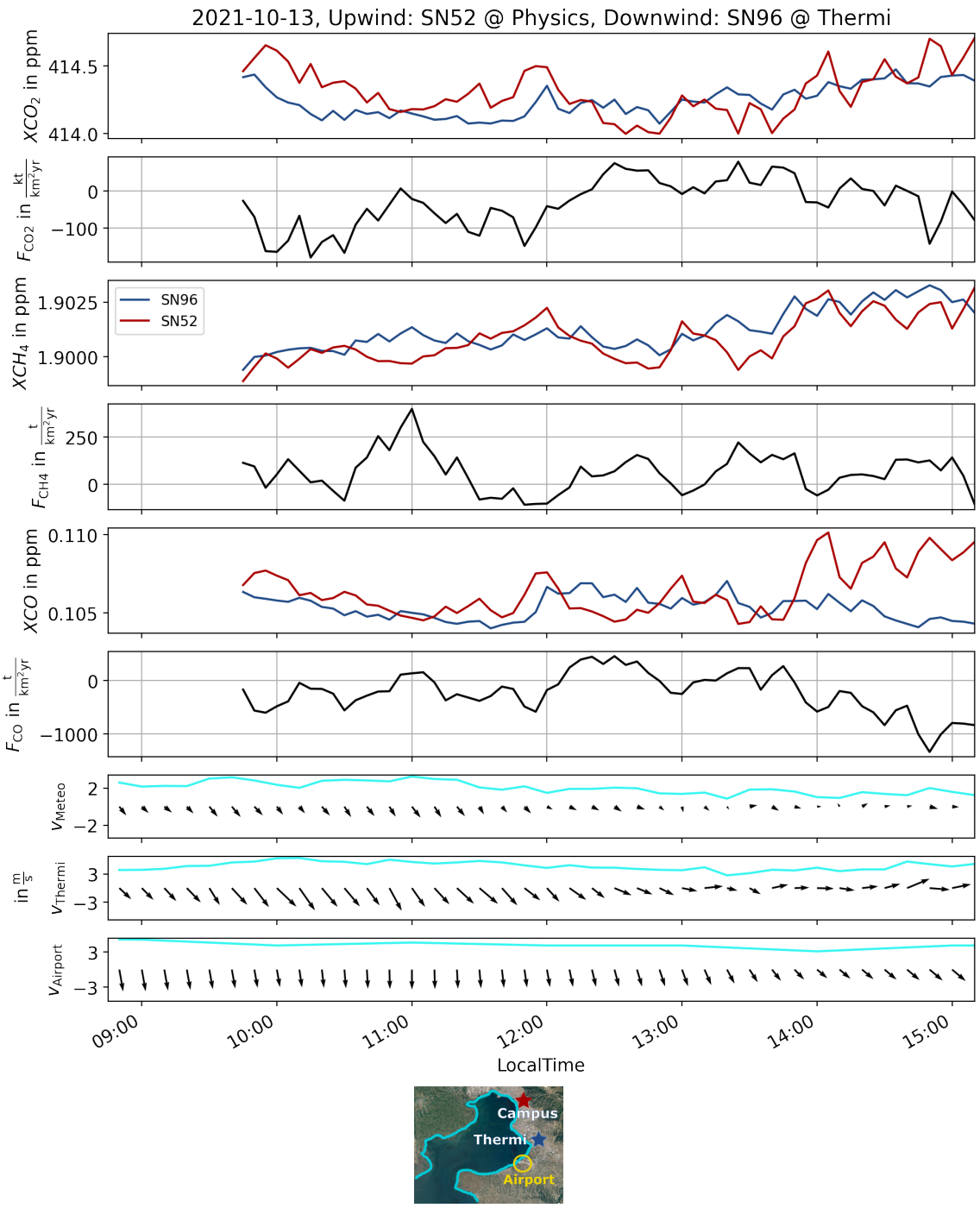

Figure A.7.: DMFs, area flux and wind data for 2021-10-13. The emission flux is calculated with a scaling factor of 3.428 as discussed in section 3.5. The wind data is displayed one hour earlier because the effects of the wind are measured late. The small map serves for orientation concerning wind direction.

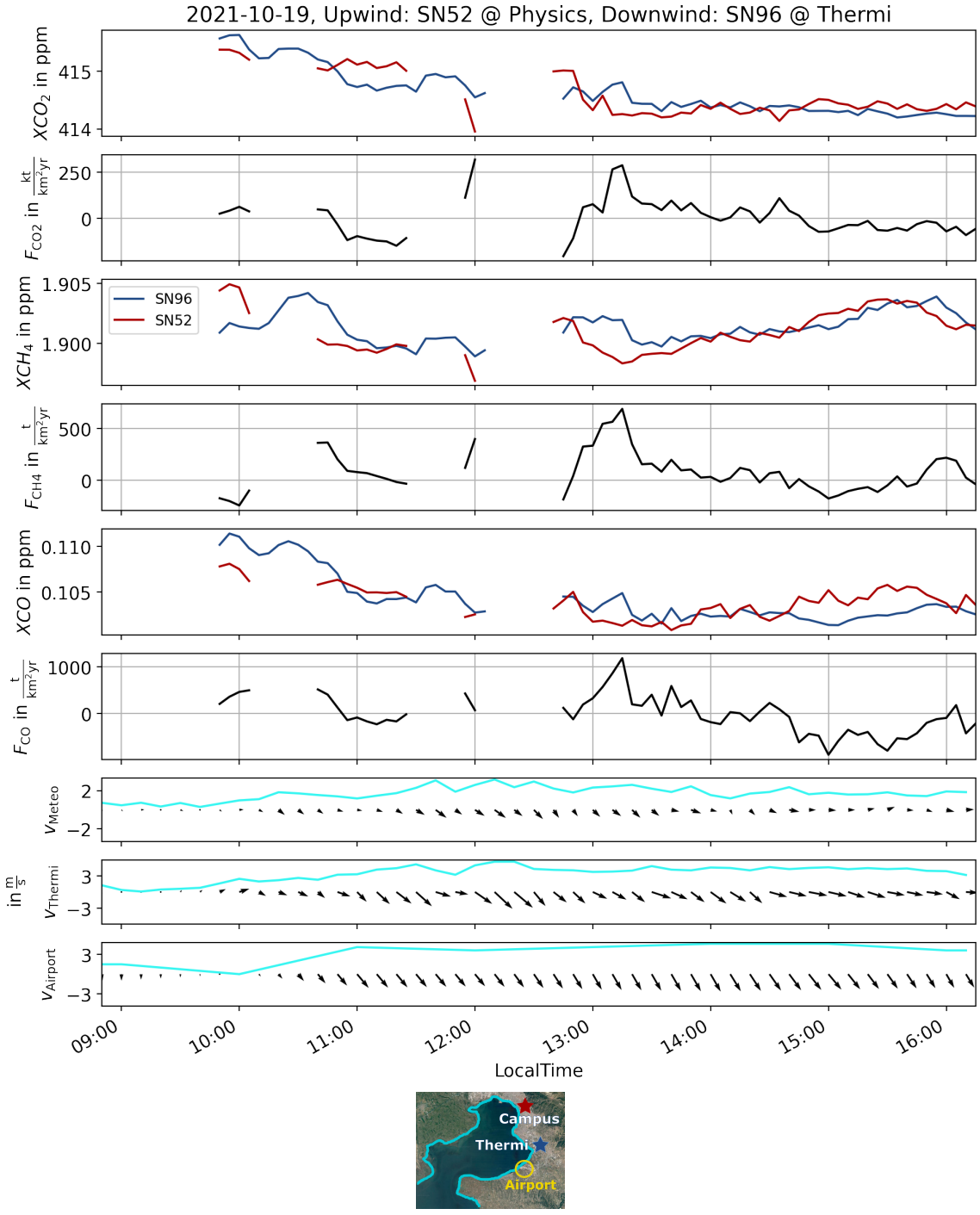

Figure A.8.: DMFs, area flux and wind data for 2021-10-19. The emission flux is calculated with a scaling factor of 3.428 as discussed in section 3.5. The wind data is displayed one hour earlier because the effects of the wind are measured late. The small map serves for orientation concerning wind direction.

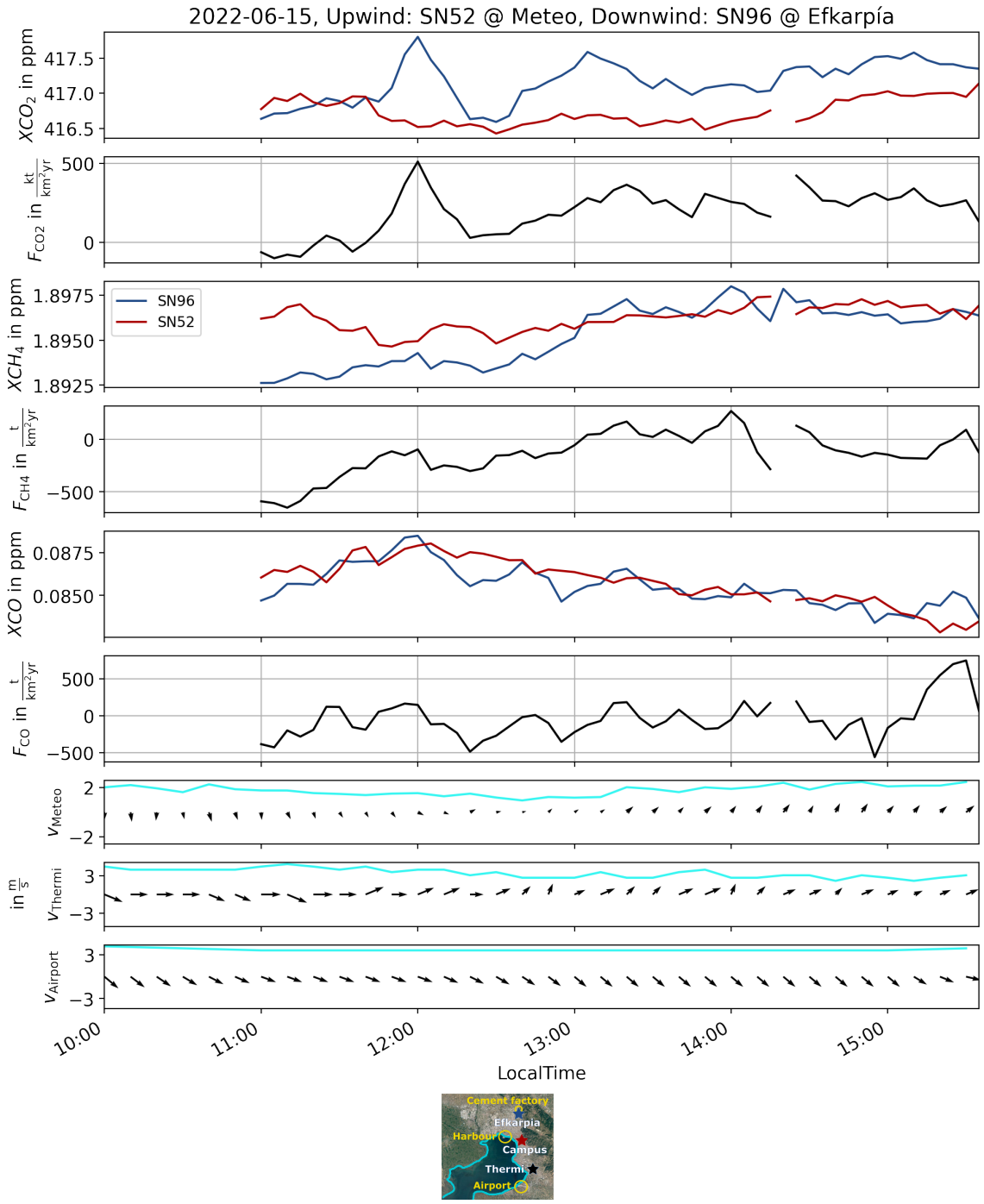

Figure A.9.: DMFs, area flux and wind data for 2022-06-15. The emission flux is calculated with a scaling factor of 3.428 as discussed in section 3.5. The wind data is displayed one hour earlier because the effects of the wind are measured late. The small map serves for orientation concerning wind direction.

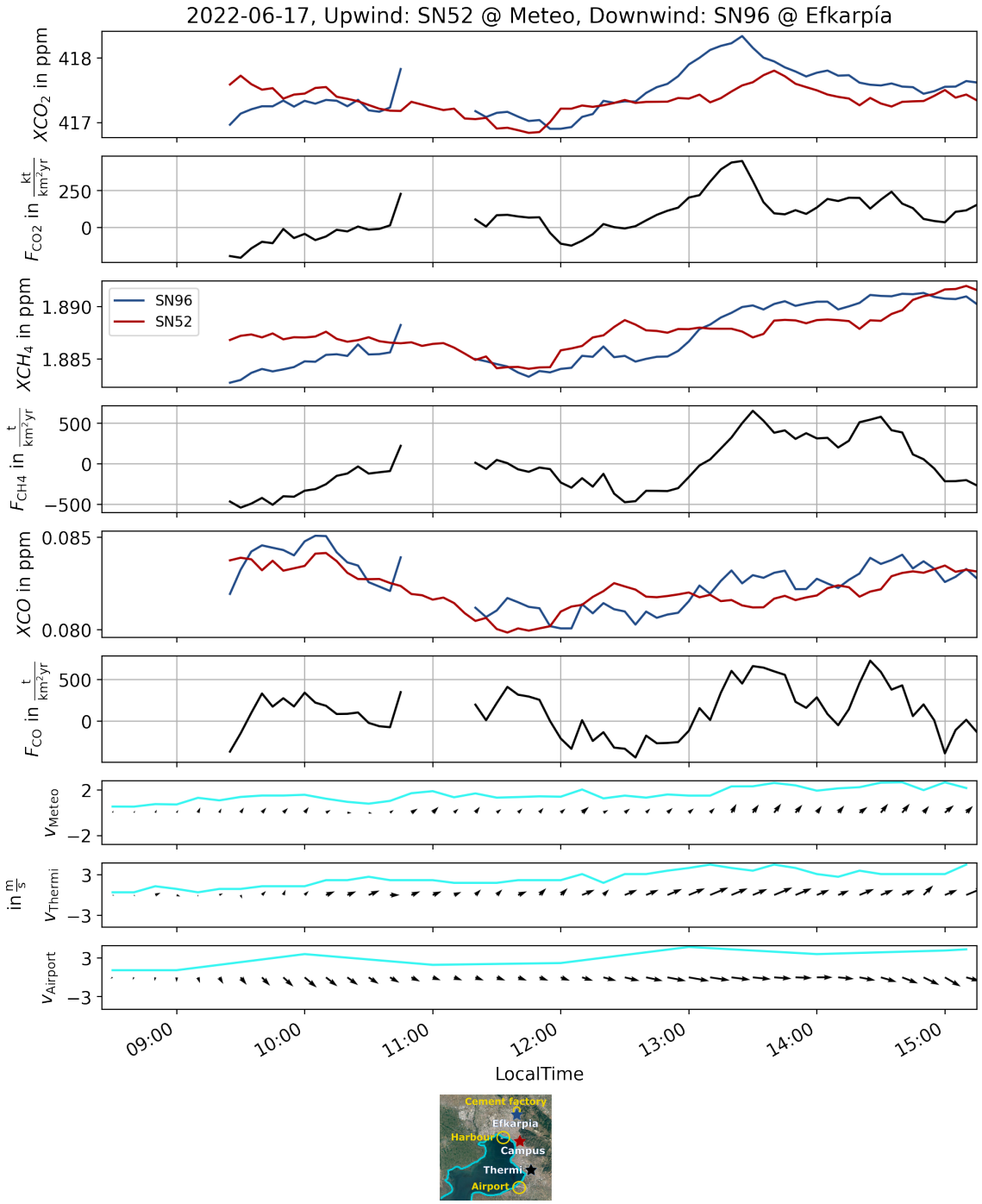

Figure A.10.: DMFs, area flux and wind data for 2022-06-17. The emission flux is calculated with a scaling factor of 3.428 as discussed in section 3.5. The wind data is displayed one hour earlier because the effects of the wind are measured late. The small map serves for orientation concerning wind direction.

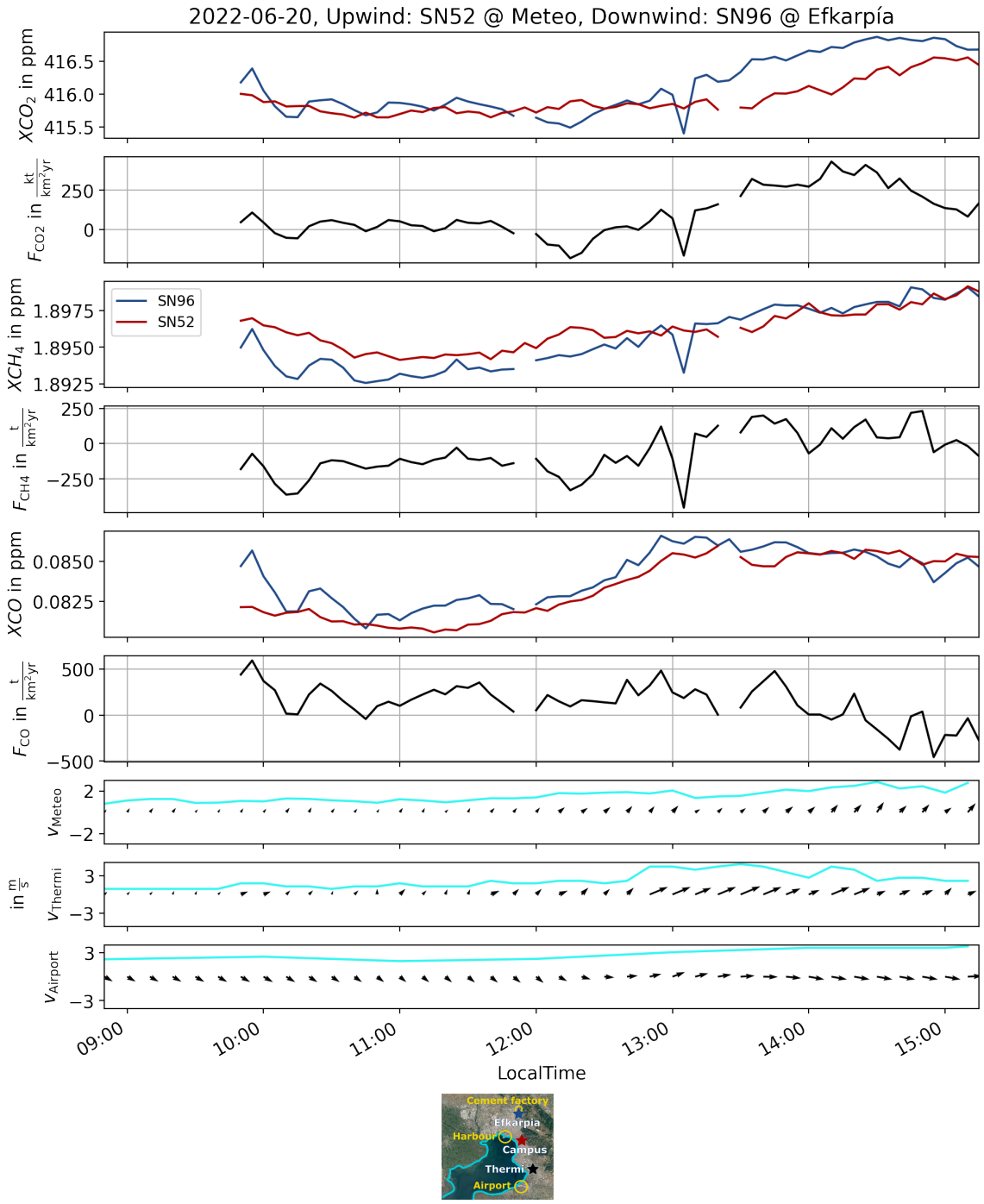

Figure A.11.: DMFs, area flux and wind data for 2022-06-20. The emission flux is calculated with a scaling factor of 3.428 as discussed in section 3.5. The wind data is displayed one hour earlier because the effects of the wind are measured late. The small map serves for orientation concerning wind direction.

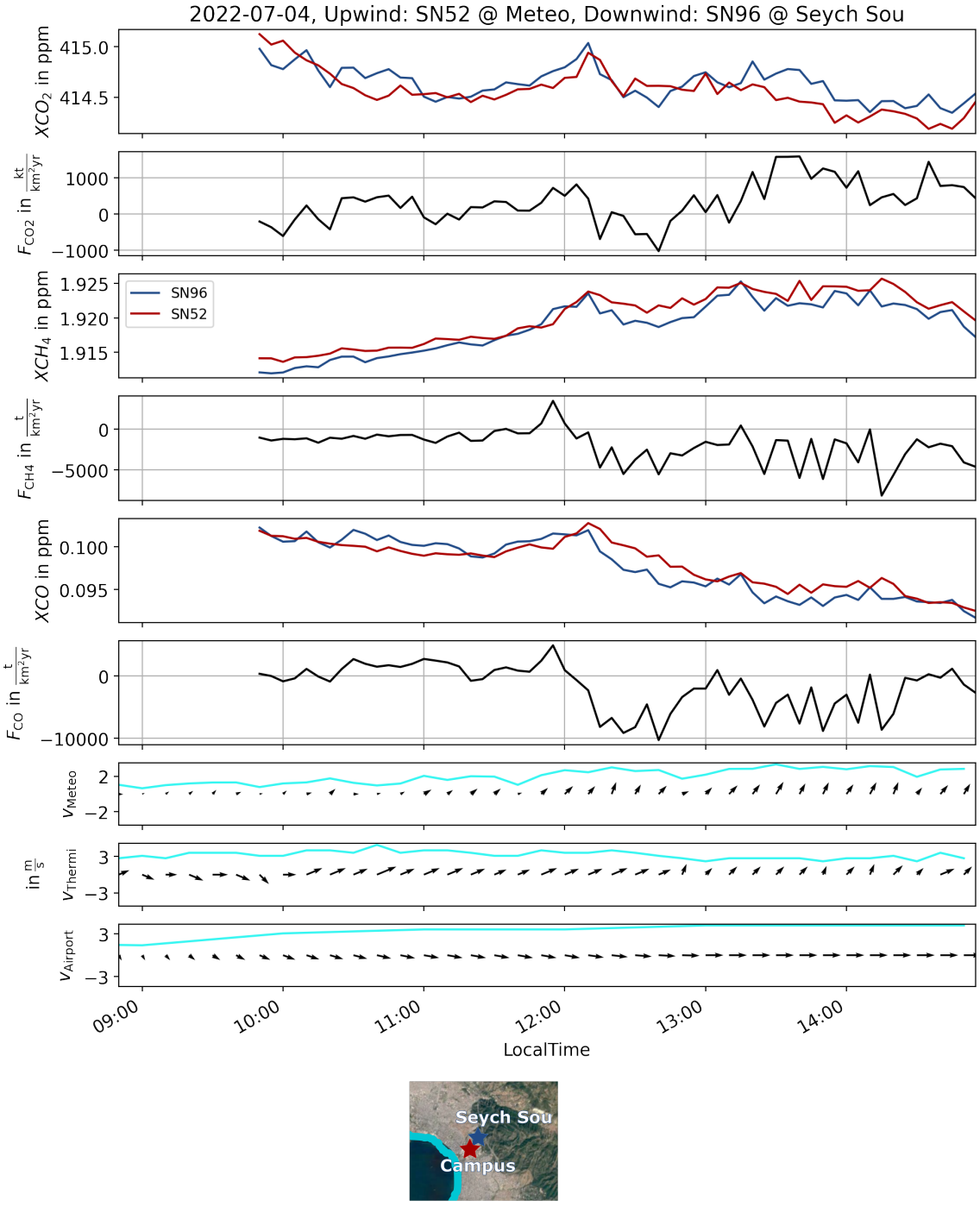

Figure A.12.: DMFs, area flux and wind data for 2022-07-04. The emission flux is calculated with a scaling factor of 3.428 as discussed in section 3.5. The wind data is displayed one hour earlier because the effects of the wind are measured late. The small map serves for orientation concerning wind direction.

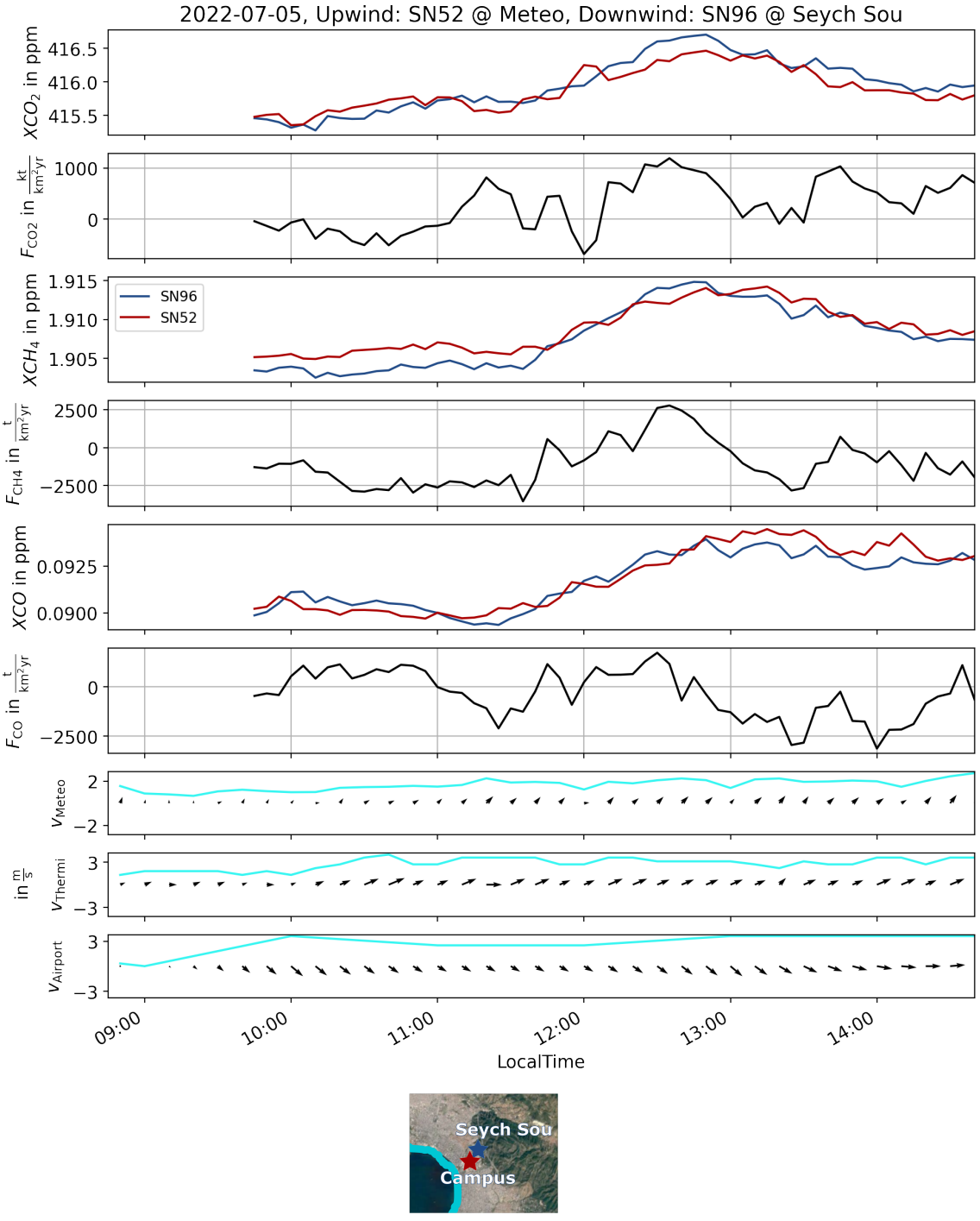

Figure A.13.: DMFs, area flux and wind data for 2022-07-05. The emission flux is calculated with a scaling factor of 3.428 as discussed in section 3.5. The wind data is displayed one hour earlier because the effects of the wind are measured late. The small map serves for orientation concerning wind direction.

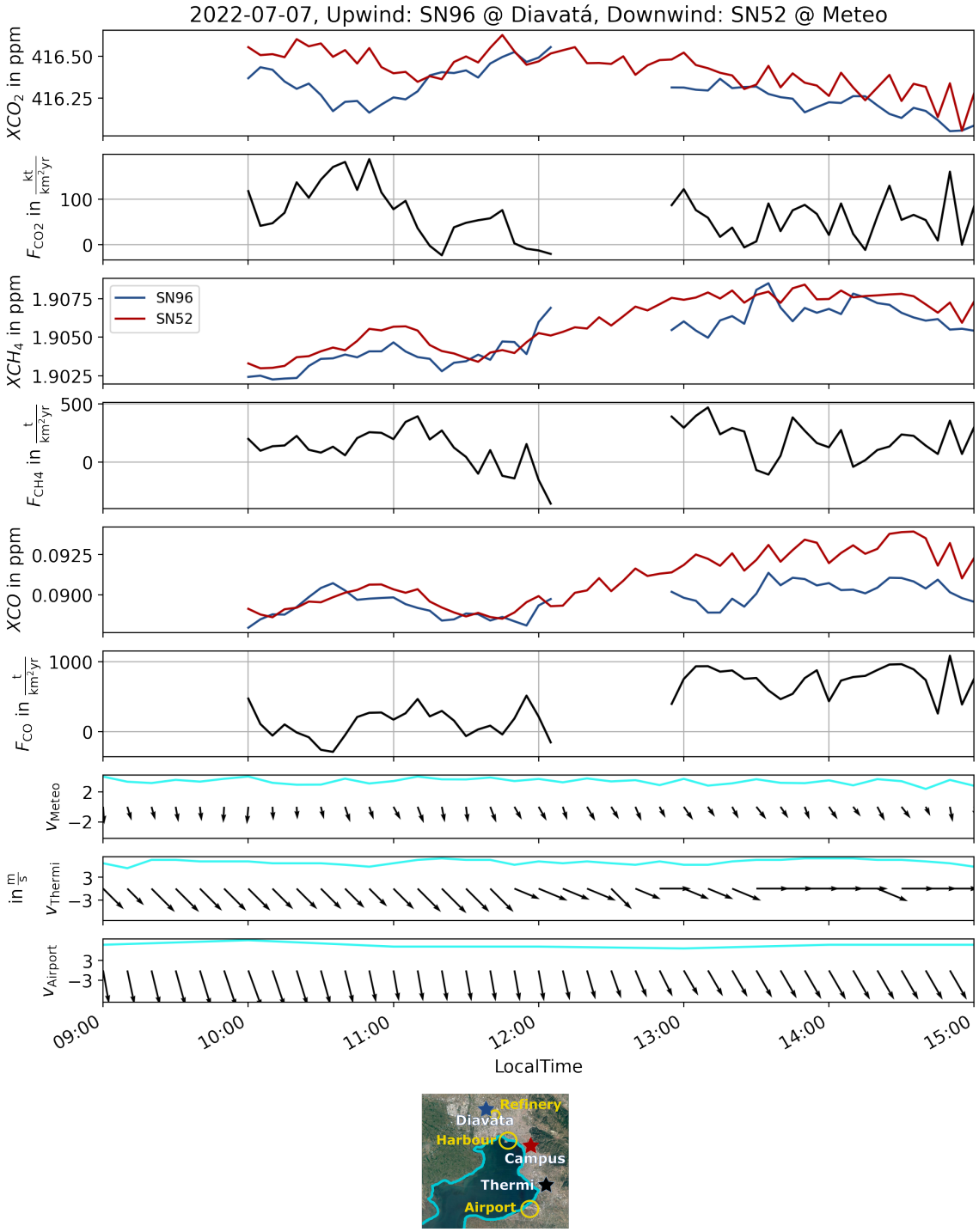

Figure A.14.: DMFs, area flux and wind data for 2022-07-07. The emission flux is calculated with a scaling factor of 3.428 as discussed in section 3.5. The wind data is displayed one hour earlier because the effects of the wind are measured late. The small map serves for orientation concerning wind direction.

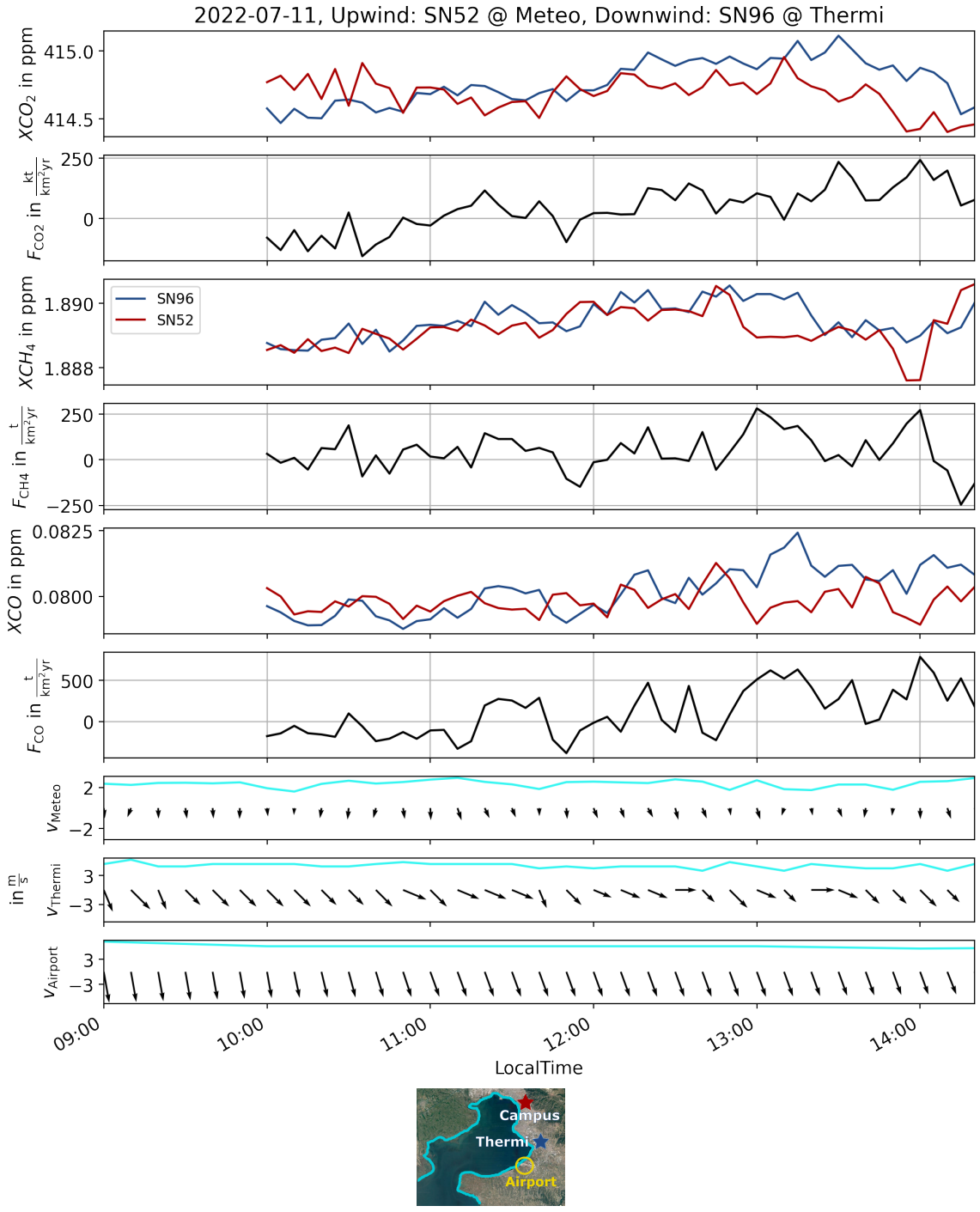

Figure A.15.: DMFs, area flux and wind data for 2022-07-11. The emission flux is calculated with a scaling factor of 3.428 as discussed in section 3.5. The wind data is displayed one hour earlier because the effects of the wind are measured late. The small map serves for orientation concerning wind direction.

A.2.5. Emission Flux: Calm Wind Conditions

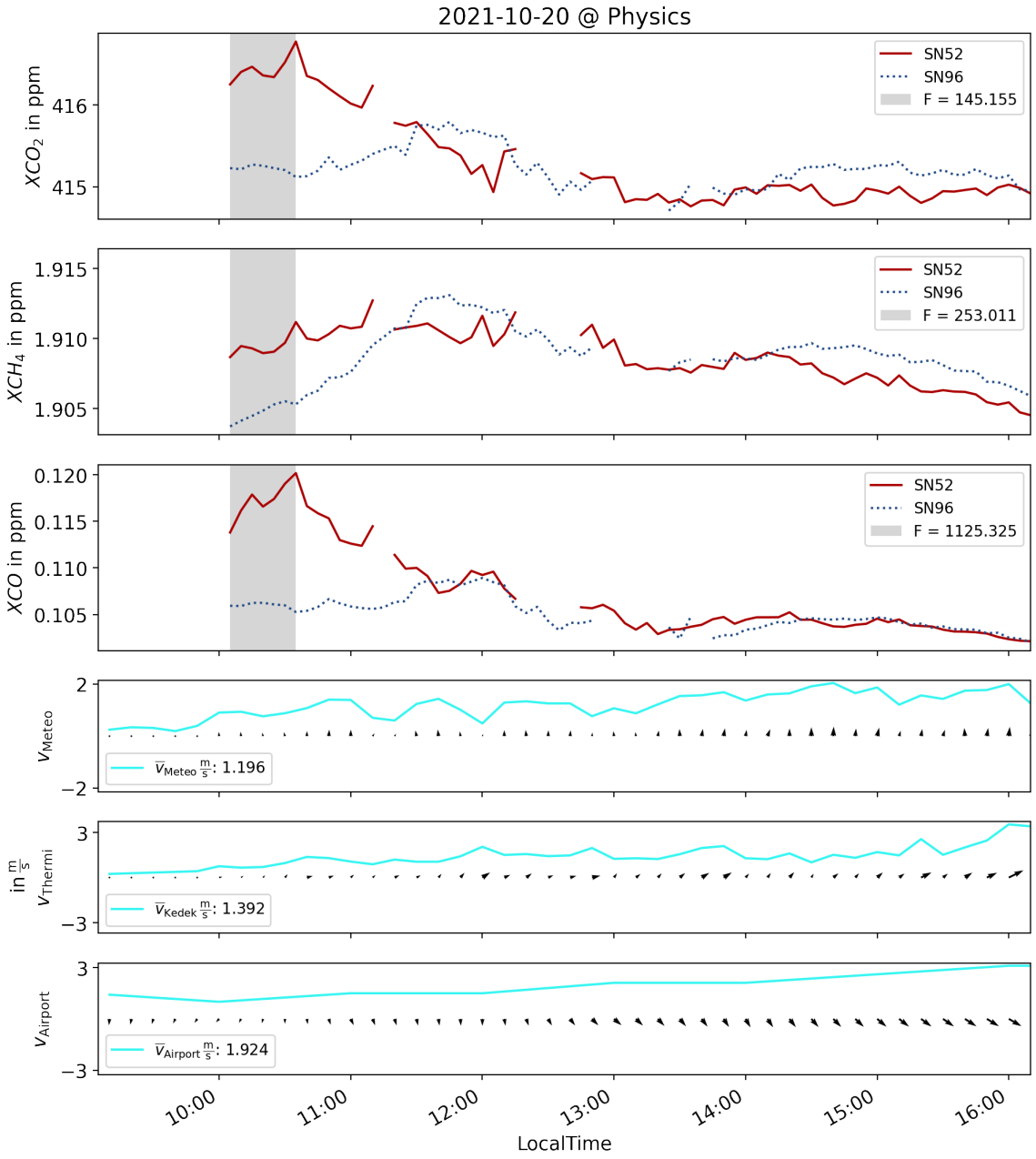

Figure A.16.: DMFs, area flux and wind data for measurements with light wind conditions on the Campus on 2021-10-20. The emission fluxes are calculated for the SN52 instrument located on Campus (SN96 in Thermi) in the chosen time interval as given in Table 4.7. The wind data is displayed one hour earlier because the effects of the wind are measured late.

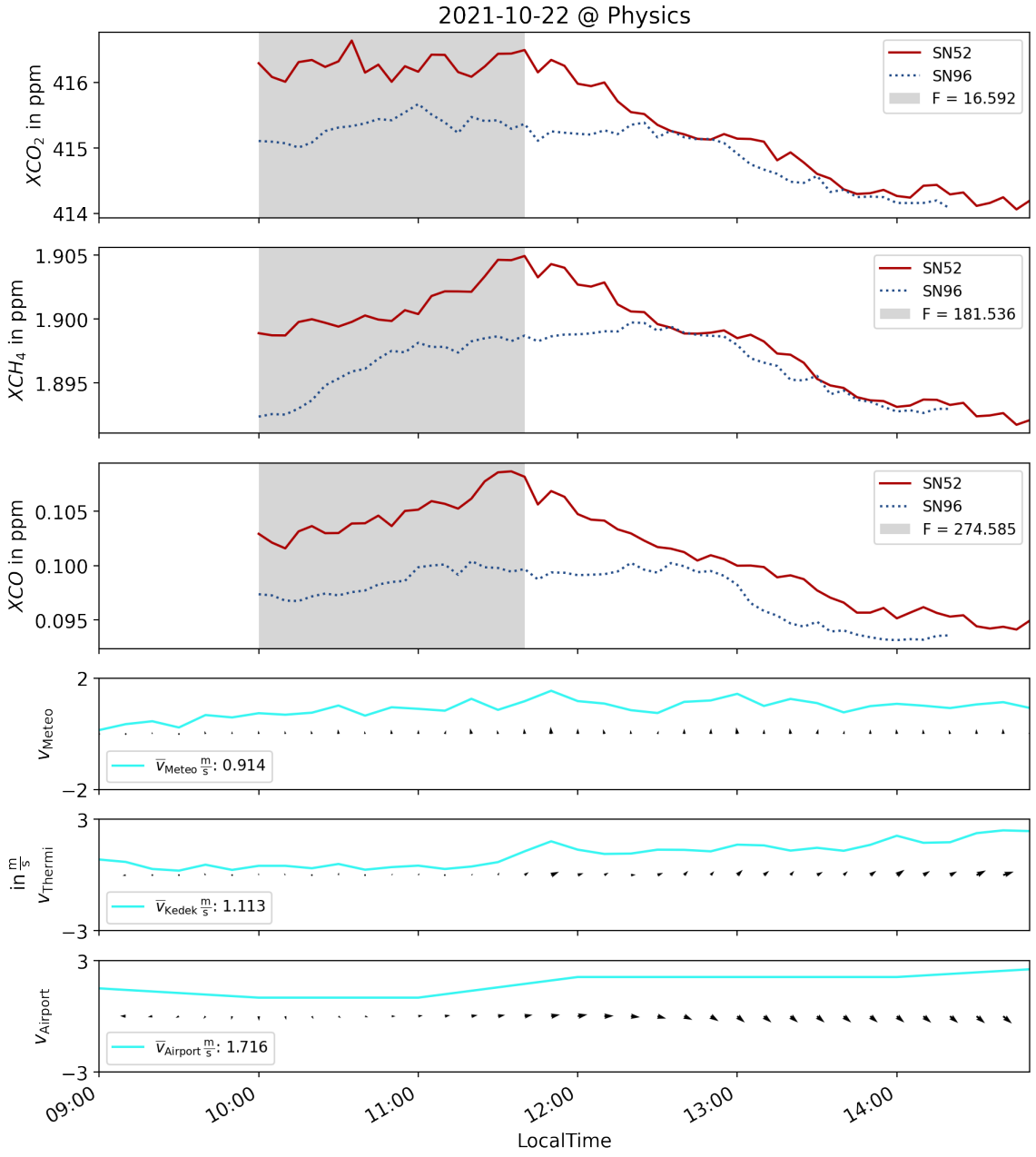

Figure A.17.: DMFs, area flux and wind data for measurements with light wind conditions on the Campus on 2021-10-22. The emission fluxes are calculated for the SN52 instrument located on Campus (SN96 in Thermi). The wind data is displayed one hour earlier because the effects of the wind are measured late.

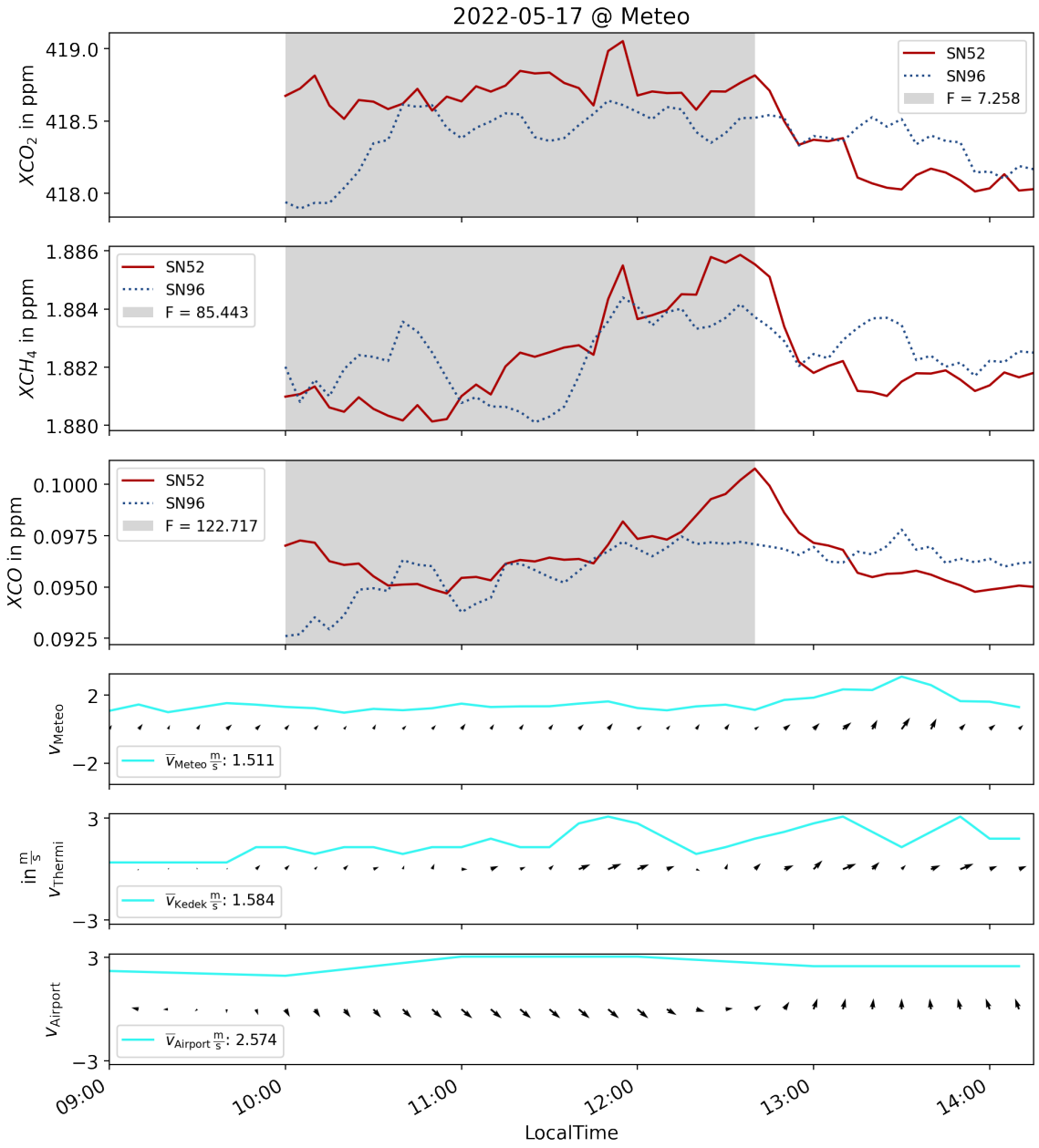

Figure A.18.: DMFs, area flux and wind data for measurements with light wind conditions on the Campus on 2022-05-17. The emission fluxes are calculated for the SN52 instrument located on Campus (SN96 in Galini). The wind data is displayed one hour earlier because the effects of the wind are measured late.

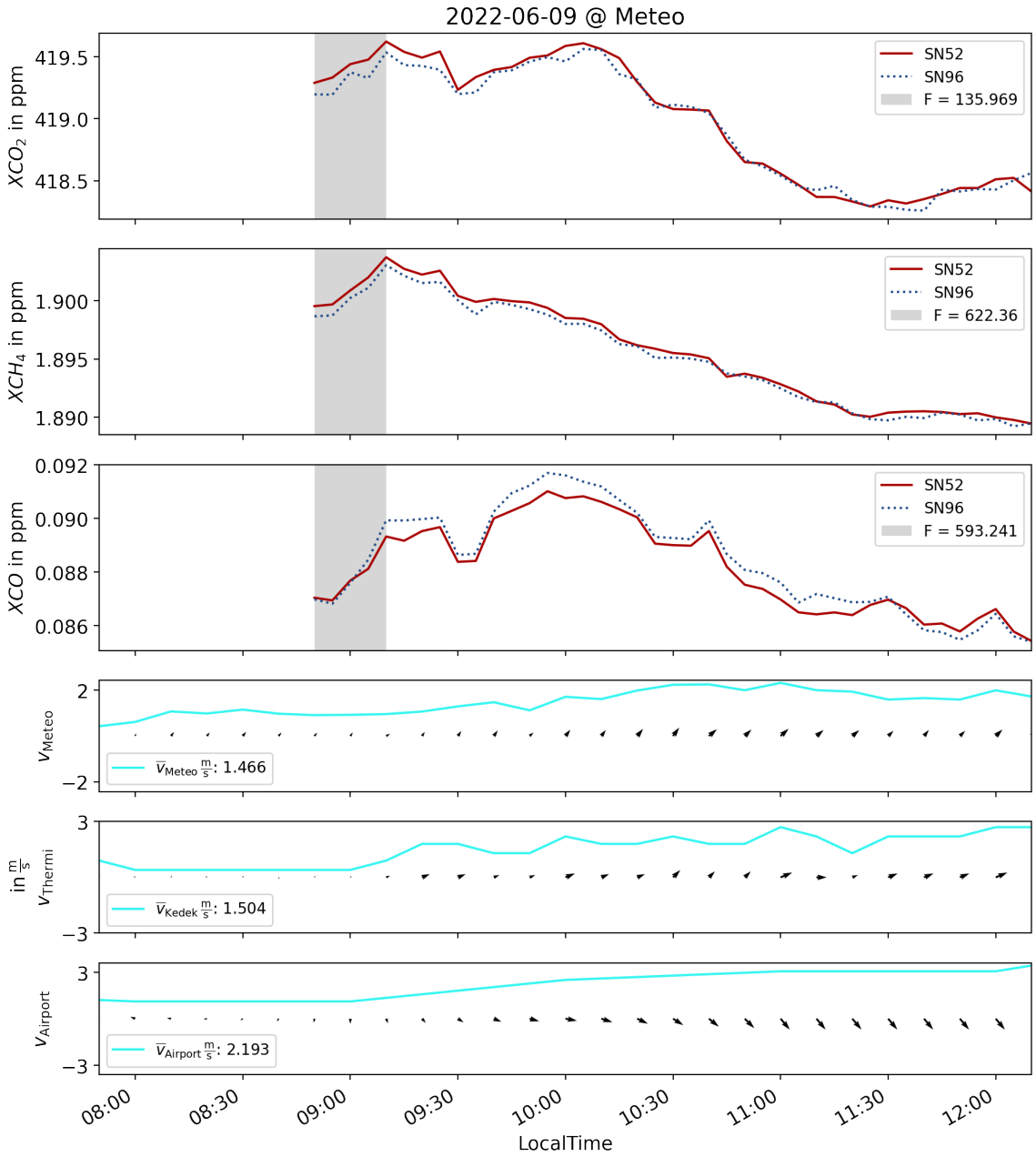

Figure A.19.: DMFs, area flux and wind data for measurements with light wind conditions on the Campus on 2022-06-09. The emission fluxes are calculated for the SN52 instrument located on Campus (SN96 also on Campus) in the chosen time interval as given in Table 4.7. The wind data is displayed one hour earlier because the effects of the wind are measured late.

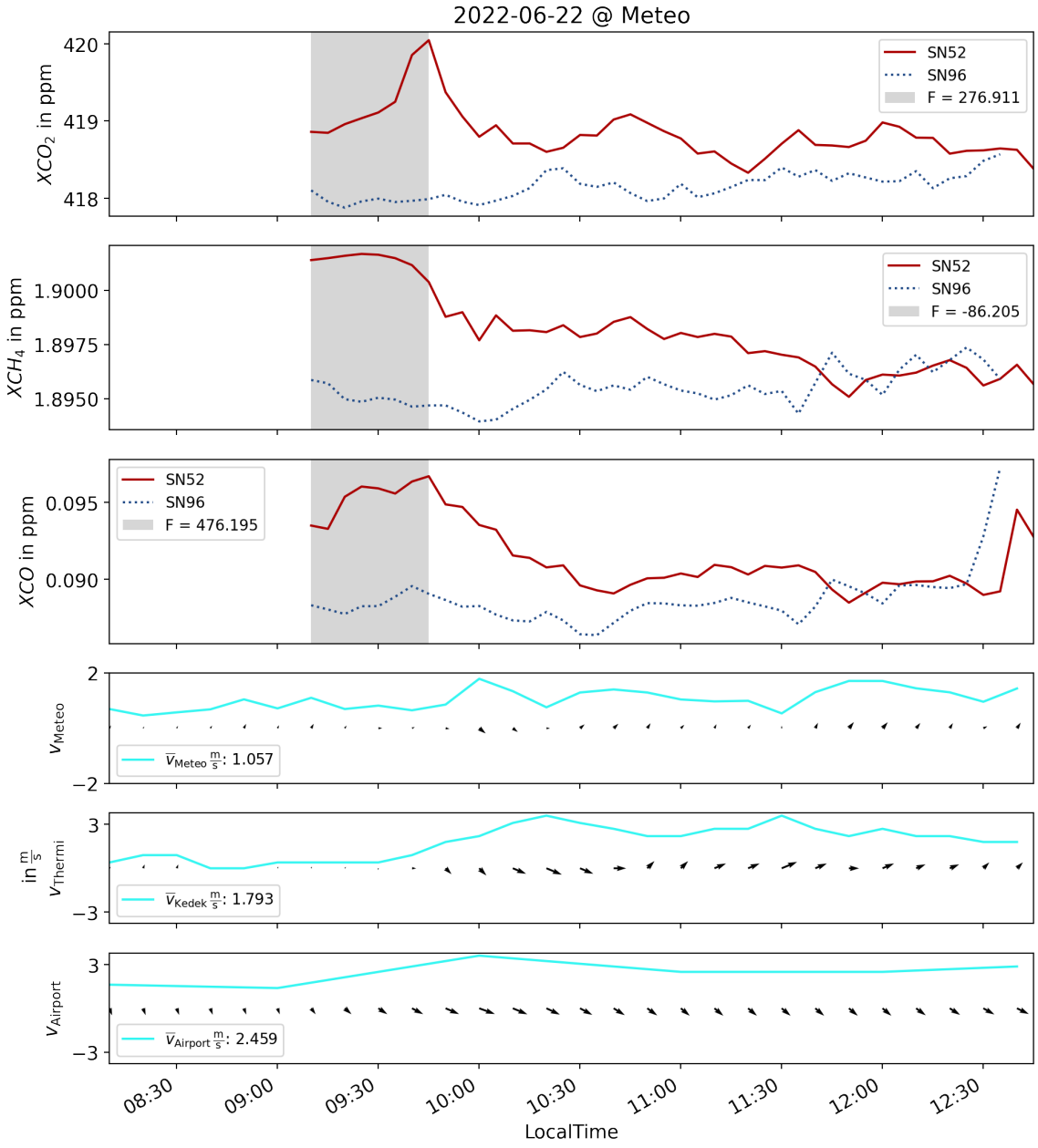

Figure A.20.: DMFs, area flux and wind data for measurements with light wind conditions on the Campus on 2022-06-22. The emission fluxes are calculated for the SN52 instrument located on Campus (SN96 in Diavatá) in the chosen time interval as given in Table 4.7. The wind data is displayed one hour earlier because the effects of the wind are measured late.

Acronyms

ASR absorbed solar radiation. 15

AUTh Aristotle University of Thessaloniki. 2, 37, 39, 41, 45, 46, 48–50, 60, 68, 70, 78, 119

COCCON COllaborative Carbon Column Observing Network. i, iii, 1, 2, 23, 24, 26, 30, 31, 51, 52, 55, 77

DMF dry-air mole fraction. 30, 43, 68

DMFs dry-air mole fractions. i, iii, vii, viii, 2, 29, 30, 32, 42, 44, 51–57, 61–66, 72, 77, 95–115

FTIR Fourier-transform infrared spectroscopy. i, iii, vii, 1, 5, 18–20, 23, 24, 26, 30, 32

GHG greenhouse gas. i–iv, 1, 2, 5, 16, 17, 24, 31, 37, 40, 41, 51, 55, 59, 68, 77

HITRAN high-resolution transmission molecular absorption database. 20

ILS instrumental line shape. 20, 26, 28

KIT Karlsruhe Institute of Technology. 1, 23, 26, 29

MOPD maximal optical path difference. 19, 20, 26

NIR near infrared. 9, 18, 20, 26, 30

OLR outgoing long wave radiation. 16

OPD optical path difference. 19, 20, 26

PBL planetary boundary layer. 8, 31, 33, 34, 50, 51, 60, 77

RF radiative forcing. 1, 17

SZA solar zenith angle. 52–55, 58, 95, 97

TCCON Total Carbon Column Observation Network. 1, 23, 26, 29, 52, 55

TOA top of atmosphere. 15

TSI total solar irradiance. 15

VMR volume mixing ratio. 21, 29

Danke / Thank you

Danke an meine Betreuerin Lena, die mir gezeigt hat, wie cool Forschung sein kann und mich ermutigt hat, eigene Gedanken zu entwickeln. Bei der engen Zusammenarbeit, insbesondere während der Kampagne in Thessaloniki, haben mich viele Dinge inspiriert: Zum einen, dass es manchmal sinnvoll ist, mehr Arbeit an einer Stelle zu investieren, um dann später davon zu profitieren. Das habe ich auch in meiner Arbeit gegen Ende gemerkt. Des Weiteren der Wille, etwas von Grund auf zu verstehen und auch nicht nachzugeben, bis das erfolgt ist. Ich bin begeistert, wie reibungsarm der Ablauf dieser Arbeit war und das hat sicher viel mit Lenas strukturierter Arbeitsweise zu tun. Darüber hinaus hatten wir in Griechenland die Möglichkeit, uns persönlich kennen zu lernen, Schach zu spielen und die dortige Zeit zu einer guten zu machen.

Danke meinen Gutachtern Frank und Peter, die mich klasse untersützt haben. In den Wochen vor der Abgabe dieser Arbeit haben sie mir schnell und motivierend geantwortet und so dazu beigetragen, dass ich nie wirklich gestresst war. Ich konnte viel Lernen durch so viel Intput von derart erfahrenen Wissenschaftlern. Auch Frank hat mich immer wieder dazu motiviert, ein Problem von Grund auf anzugehen und nicht im Lehrbuch danach zu suchen.

A big thank you to our collegues at AUTh in Thessaloniki. Thanks to Marios Mermigkas and Thomas Panou not only for operating one instrument, but also for supporting the campaign in many ways and bringing us to nice places. Dimitrios Balis never hesitated to share his knowledge with us. He showed us possible measurement sites, including adventurous trips in his car. He mainly took care of the organisation of the campaign on site. This included the receipt of the shipped instruments, their storage in Thessaloniki and the procurement of additionally required material. Thanks to Prodromos Zanis and the others in the meteorology building who were there when we were in need of data or advice. Stavros Keppas helped us concerning meteorological data at the ΚΕΔΕΚ station. And finally to all the others who helped with everything and treated us so welcoming. Without them, this campaign would not have happened and the experience for us in Greece would not have been so positive!

Und danke der Arbeitsgruppe IMK-ASF-BOD. Obwohl ich selten am Campus Nord vor Ort war, habe ich mich jedes Mal gut aufgehoben gefühlt. Ich hatte nie das Gefühl, dass eine Frage blöd ist oder ich als Masterstudent in der Hierarchie unten stehe. Mit Darko als Büronachbar war immer ein trockener Witz bereit, das war schön. Bene war sich nie zu schade, mir eine Frage zu beantworten oder sich einen fehlerhaften Code anzuschauen. Des Weiteren gilt ein Dank allen, die (aus meiner Perspektive) im Hintergrund arbeiten: dem Sektretariat, den Gruppenleiter Frank und Thomas, Frau Jacob von der Reisekostenstelle und Jochen, der die Stromversorgung für unser Spektrometer konstruiert hat.

Danke an meine Familie, auf deren Unterstützung in mannigfaltiger Art ich immer vertrauen kann. Das Vertauen in mich, das mich durch das lange Studium getragen hat

und mir nebenbei erlaubt hat, viele andere Dinge zu machen. Danke, dass ihr bei allem, was ich mache, auf eine Art dabei sein wollt.

Danke an alle Menschen, die über das lange Studium hinweg dabei waren und es zu einer so schönen Zeit gemacht haben. Ich bin froh, dass wir bis heute in Kontakt sind und immer wieder neue Pläne und Ideen entwickelt haben, weit über das Physik-Studium hinaus. Obwohl es viele anstrengende und frustierende Tage in der Bibliothek gab, hat unsere tolle Gemeinschaft uns immer weitermachen lassen.

Danke an Lena für das Ohr, das mir so geduldig zuhört und verständnisvoll ist. Und dafür, dass du so lustig bist und mich im Lernzentrum immer ablenkst!!

Danke an Mikele und Cinzia, die mir mit ihrem kleinen Geschäft immer auf ein Neues ein Lächeln ins Gesicht bringen.